Answer to reviews for ms amt-2018-25 - Formenti et al., Aerosol optical properties derived from POLDER-3/PARASOL (2005-2013) over the western Mediterranean Sea: I. Quality assessment with AERONET and in situ airborne observations

We thank both referees for evaluating the manuscript and providing us with feedback on its scientific content. Detailed responses to their remarks are presented in the body of text here below in blue

Anonymous Referee #1

The authors present a 2-part analysis of POLDER-3/PARASOL oceanic aerosol retrievals against ground-based AERONET validation (in the Mediterranean), as well as a comparison of different sub-orbital (in-situ) data taken in the region. For the former, the authors present compelling evidence of POLDER-3 sensitivity to aerosol size, fine/coarse mode discrimination, AOD, and non-sphericity (to some extent). For the latter, the authors compare results from different optical-particle counters, providing a nice summary of retrieved complex refractive index for different aerosol types. The authors have clearly performed a thorough literature review, and this work should be published after minor revisions.

General Comments:

I would strongly encourage the authors to convert AOD, fine-mode AOD, and coarse mode AOD to 550 nm rather than 865 nm. Many other retrieval algorithms provide AOD information (such as MODIS DT) at this wavelength (or at least near it), and solar irradiance is much higher (meaning absolute attenuation will be larger) at 550 nm. Fine-mode AOD is typically very small at 865 nm, which will result in a lower RMSE and correlation as compared to the coarse mode (which you see in Figures 4 and 5). I expect that your fine-mode AOD range will more than double by extrapolating to 550 nm, and I expect your RMSE to increase substantially too. Although the lack of absorption is probably not an issue because your retrieved fine-mode AODs are so low (and desert dust is non-absorbing in the red and NIR), you may see a low bias in AODf at 550 nm because the effects of absorption can lead to non-linear errors in retrieved AOD. As POLDER's sensitivity to sphericity is probably dependent on total aerosol loading, might it make sense to report non-spherical AOD rather than non-spherical AOD fraction?

We understand and appreciate the comments by Referee #1. It is true that the choice of wavelength is of importance: 865 nm results in small values of fine-mode AOD (compared to 550 nm), but it is a question of accuracy. The objective of the paper is the validation of the POLDER-3 retrievals at the wavelengths where the instrument made the measurements and the oceanic algorithm is applied. These are 865 and 670 nm, but not 550 nm. Converting all data to 550 nm would result in inducing an additional bias due to the limitations in the retrieval of the Angstrom exponent (AE). This is why, as a first step, it is of first importance to evaluate the retrieval at the instrument/algorithm wavelength. However, we will certainly consider the conversion for the second part of this paper, which will address the analysis of the AOD products for the investigation of the aerosol spatial distribution and temporal variability in the western Mediterranean. A sentence on this issue has been added in section 5.2.

I might be a bit biased towards the POLDER-3/AERONET analysis, but I think the paper might flow better if all of the in-situ analysis were moved to the supplemental (or into its own paper). It really seems like an add-on to the POLDER-3/AERONET work.

We considered in deep detail this suggestion by Referee #1. Our feeling, and the motivation behind the analysis, is that the comparison with the in situ data provides with additional information which augments the results obtained by the comparison with AERONET. In particular, they allow investigating the sensitivity to size of POLDER-3 retrievals. In this respect, we would prefer keeping them with the main text. This would imply keeping Figure 3, bottom panels of Figure 4, and Figure 7. The

alternative suggestion by Referee #1 is that the in situ-POLDER comparison could make the object of a paper *per se*. Again, we felt that the complementary of AERONET and in situ is the added value of the paper. We prefer to gather the available information in a single paper, the approach is rather original and we believe it gives more value to our study. On the contrary, it seems to us that there is not enough supplementary material for writing a solid additional paper.

Specific Comments:

Line 255: Should read “can be calculated as”.

Done

Line 365: Is this increased temporal window only for AODF and AODC, or for all measurements?

This was done only for AOD_F and AOD_C. To clarify the sentence has been changed from “Instead, the averaging temporal window was extended to the whole afternoon (that is, all data points later than 12:00 UTC) in order to allow for a significant dataset for comparison” to “For these two variables, the averaging temporal window was extended to the whole afternoon (that is, all data points later than 12:00 UTC) in order to allow for a significant dataset for comparison”.

Line 452: I think this should read “retrieved” not “measured”, as POLDER does not measure AOD.

Correct - Done

Line 580-582: At the risk of sounding like a broken record, I believe that this can be explained by your use of 865nm AOD rather than 550 nm AOD.

A sentence has been added.

Table 4: The uncertainties here do not make sense to me [maybe I am just missing something?]: 1. Your RMSE is substantially larger than the absolute term in your AOD uncertainty (which you have as an extremely low 0.003 [should this be 0.03?]) The 0.003 corresponds to Bias value reported in Figure 4.

2. AE uncertainty should be a function of AOD or just a flat envelope. The higher the AOD, the greater confidence you should have in particle properties.

The AE uncertainty is expressed as a function of AE from RMS and Bias values obtained in Figure 8, as done for AOD from Figure 4. The error is larger for larger AE which corresponds to lower AOD values.

3. Non-spherical AOD uncertainty makes a lot more sense than f_{NCS} uncertainty, as you can account for inherent bias at low AOD.

The POLDER-3 oceanic algorithm retrieves f_{NCS}, which can only assume fixed values (0, 25, 50, 75 and 100%), without interpolation, and not the AOD_{CNS}. In this methodological paper it is therefore logic to evaluate this quantity and not the AOD products. We agree with the reviewer that f_{NCS} poses problems when the AOD is low, that is why the product is provided only for AOD > 0.1.

Figure 2-3: I would move this to supplemental, but up to you.

We agree in moving Figure 2 but would prefer keeping Figure 3 in the main text as it is the parallel to Figure 1.

Figure 4: I would remove the bottom to panels, as you have too few data to provide anything of value from airborne. Maybe then merge Figure 4 with 5?

Again, we believe in the added values of the comparison to the in situ data, albeit based on a limited number of data points. The current representation is simple and easy to read. We would like to keep it as it is.

Figure 6: There appear to be a couple of issues with this figure: 1. Should the caption read ”volume distribution at Dcut-off < 1.0 μm (left) and days with AERONET Dcut-off ≥ 1.0 μm (right)” or ”volume distribution at Dcut-off < 1.0 μm (Top) and days with AERONET Dcut-off ≥ 1.0 μm (Bottom)” 2. Figure 6 reads as though retrieved fine-

mode AOD is the top plot, and coarse-mode AOD is the bottom plot. a. I assume that this is a mistake, and that the fine-mode retrievals are on the left, and the coarse-mode retrievals are on the right side. b. This should also be clarified in the caption.

The reviewer is correct: the fine-mode AOD is the top plot and the coarse-mode AOD is the bottom plot. This is now corrected. The caption should read “the caption read ”volume distribution at Dcut-off < 1.0 μm (left) and days with AERONET Dcut- off ≥ 1.0 μm (right)”

Figure 7: I would move this to the supplemental as well.

See previous comments. We would like to leave this in the main text.

Figure 8: I would change this to being contingent on AERONET AOD > 0.1, but this is just my preference. I would also remove the airborne data, as there are too few data. Maybe instead you could have 3 plots of AE, with different AOD requirements for each (>0.05, >0.1, >0.2)? This would help demonstrate the dependence of AE errors on AOD.

The scope of this figure is not to show how the error on AE changes with increasing AOD bur rather how it compares to the AERONET retrieval when the right screening of AOD by POLDER-3 is done. Again the airborne data are few but illustrative.

Figure 10: Would it make sense to change this to AODNS vs AODCNS?

As we explained previously, the POLDER-3 oceanic algorithm retrieves f_{NCS}, which can only assume fixed values (0, 25, 50, 75 and 100%), without interpolation, and not the AOD_{CNS}. To clarify this, the text in lines 153-161 has been reworded. Because of that, we would like to keep the figure as it is. We have therefore added Figure 10 to show the scatterplot comparison between the POLDER-3 AODCNS and the AERONET AODNS. The 2 quantities are strongly correlated (R=0.87) but the POLDER-3 AOD_{CNS} is lower than the AERONET AOD_{NS}, as expected. Explaining text has been added in Section 4.4. Former Figure 10 is now included as Figure 9.b.

Anonymous Referee #2

General comments:

The topic of the study is very important: an analysis of the quality of POLDER satellite measurements of aerosol properties over the Mediterranean. This analysis and error information can then be used by other researchers in the CHARMEX project.

The paper constitutes a very comprehensive study, and gives a clear overview of the Aeronet and aircraft measurements, together with their error sources. The thorough discussion of measurement methods and their errors and characteristics, including the supplementary material, is welcomed and is an excellent example for other similar studies.

The paper is well written. The methods are well described, with extensive referencing. However, some figures could be clarified (see comments below).

In the introduction the title should be explained. The reader may wonder what the topic of part 2 will be. This should be clarified, e.g. at the end of the discussion. The fact that the interesting Figure 12 is only given at the end of the paper is probably a cliff-hanger to paper 2 ? There is no information on trends in aerosols over the West-Mediterranean from POLDER and Aeronet data. That is a pity – is 8 years too short? Or will the trends be described elsewhere?

We have now added a sentence in the introduction and modified the sentence at the end of the discussion to clarify that the topic of part 2 would be the analysis of spatial distribution and temporal variability, including trends, provided by the analysis of POLDER-3 retrievals over the western Mediterranean.

Specific comments:

1. Please say in the introduction why there is no attention given to the spatial distribution of aerosols in the West-Mediterranean area. The text given on lines 608-611 should be given in the introduction as well.

This is now done

2. l. 131 ff: All symbols, like m, D, etc., should be in italics (slant font). This does not hold for acronyms, like AOD.

This is now done

3. Header Table 1: Nbpol is an unclear quantity; please define.

To increase readability, the caption was changed as “Table 1. List of AERONET stations available in the western Mediterranean region retained for this study. The number of ocean POLDER pixel within 0.5° from the position of the station is indicated (N_{PIXEL}). The number of observations by POLDER-3 and AERONET between March 2005 to October 2013, and the number of coincident days (within brackets) are also reported.” Nbpol was changed into N_{PIXEL}.

4. Table 4: AOD, AE, etc. are acronyms and not symbols, so they should be in upright font.

This is now done.

5. Figure 2: What do the green boxes mean?

As indicated in the caption, green boxes indicate the input values from airborne measurements (size distribution, scattering and extinction coefficients) and the initial values of the complex refractive indexes estimated from published literature.

6. Caption Figure 4: What does daily AOD mean in the case of a polar orbiting satellite at 13:30? The individual data points of POLDER averaged over the 1x1 deg2 box?

Yes, daily indicates the average of individual data points of PODLER averaged over the 1x1 degree box every day.

7. Figure 4: Why is Nb used instead of N for the number of points?

This is now corrected.

9. Caption Figure 5: Note that the definition of fine and coarse modes is probably not the same for POLDER and Aeronet.

A sentence has been added to the Figure caption.

10. Figure 6: I find this figure difficult to understand. D_cut-off is the threshold value itself, so it should be D > D_cutoff and D < D_cutoff. Is here D_cutoff itself a variable quantity ? I also do not understand the difference between the left and right figures.

There was a problem with the order of panels in Figure 6 (see answer to Reviewer #1) which is now corrected. In Lines 180-182 we clarify this point but modifying the sentence as "The fine and coarse modes of the retrieved volume size distribution are defined as the modes below and above a threshold diameter ($D_{cut\text{-}off}$) corresponding to the minimum of the size distribution. The $D_{cut\text{-}off}$ value is not fixed but can vary between 0.44 and 0.99 µm". This sentence is also added to the Figure caption.

11. Please always give the physical quantity in the axis label, so e.g. in Fig. 5, 6, and 7 AOD should be given in the label.

This is now done.

12. Figure 9: Please indicate the three AE ranges with horizontal boundary lines.

This is now done.

13. Caption Fig. 10: ns > NS. Please say that f_NS also is a fraction in terms of total optical depth.

Done

14. Caption Fig. 12: Please use capitals for CNS, NS, ...

Done

15. Caption Fig. 12: the AOD > AOD, classes > class, curves > curve

Done

16. Concluding remarks: Could a recommendation be added on how to determine the cut-off diameter between fine and coarse aerosols?

A sentence has been added

17. Suppl. Table S1: what is the imaginary part of the refractive index?

The imaginary part of the refractive index is zero in the ocean retrieval algorithm. This is now added in the caption of Table S1

18. Suppl. l. 24: at which wavelength does this refractive index value hold?

The wavelength value has been added

19. Suppl. l. 74: change > changes

Done

20. Suppl. Table S3: please use a better alignment of words and numbers to avoid ugly breaks.

Done

21. Suppl. L. 168: particle > particles

Done

All the textual corrections / suggestions have been accepted

Aerosol optical properties derived from POLDER-3/PARASOL (2005-2013) over the western Mediterranean Sea: I. Quality assessment with AERONET and in situ airborne observations

Paola Formenti[1,*], Lydie Mbemba Kabuiku[1,2~~4~~], Isabelle Chiapello[2~~3~~], Fabrice Ducos[2~~3~~], François Dulac[4~~3~~] and Didier Tanré[3~~2~~]

[1] Laboratoire Interuniversitaire des Systèmes Atmosphériques, UMR CNRS 7583, Université Paris-Est Créteil et Université Paris Diderot, Institut Pierre-Simon Laplace, Créteil, France

[2] Agence De l'Environnement et de la Maîtrise de l'Energie (ADEME), 20 avenue du Grésillé, Angers, France

[3] Laboratoire d'Optique Atmosphérique, UMR CNRS 8518, Université Lille, Villeneuve d'Ascq, France

[3~~,4~~] Laboratoire des Sciences du Climat et de l'Environnement, UMR 8212 CEA-CNRS-UVSQ 8212, Institut Pierre-Simon Laplace, Université Paris-Saclay, Gif-sur-Yvette, France

~~[4] Agence De l'Environnement et de la Maîtrise de l'Energie (ADEME) 20 avenue du Grésillé, Angers, France~~

* corresponding author (paola.formenti@lisa.u-pec.fr)

~~For~~ Revised version submitted~~ssion~~ to Atmos. Meas. Tech., ChArMEx special issue

Abstract

The western Mediterranean atmosphere is impacted by a variety of aerosol sources, producing a complex and variable mixture of natural and anthropogenic particles, with different chemical and physical properties. Satellite sensors provide a useful global coverage of aerosol parameters but through indirect measurements that request careful validation. Here we present the results of a long-term regional scale analysis of the full dataset (March 2005 and October 2013) of POLDER-3/PARASOL ocean operational retrievals of the total, fine and coarse aerosol optical depth (AOD, AOD_F and AOD_C), Angstrom exponent (AE), and the spherical/non-spherical partition of coarse-mode AOD (AOD_{CS} and AOD_{CNS}), respectively. The evaluation is performed using data from seventeen coastal and insular ground-based AERONET sites on one side, and airborne vertical profiles of aerosol extinction and number size distribution obtained by the SAFIRE ATR-42 aircraft operated in the area during summer 2012 and 2013 on the other side. This study provides the first regional evaluation of uncertainties of the POLDER-3 products, and highlights their quality. The POLDER-3 Ångström exponent, representing AOD spectral dependence in link with the aerosol particle size distribution, is biased towards small values. This bias, however, does not prevent using AE for classifying the regional aerosol laden air masses. AOD_F corresponds to particles smaller than 0.6-0.8 µm in diameter and appears suitable to monitor the aerosol submicron fraction from space. We also provide an original validation of POLDER-3 AOD_C and its spherical/non-spherical partition, which shows agreement within 25% with AERONET shape retrievals when the aerosol coarse fraction dominates.

1. Introduction

Aerosols include a large variety of particles (mineral dust, sea salt, soot carbon and organic species, sulphates, nitrates…) emitted by natural and anthropic sources and different mechanisms (combustion, wind erosion, gas-to-particle conversion, etc.). Aerosols have a short lifetime in the troposphere (Boucher, 2015) but they are key to many atmospheric processes, as the redistribution of solar and thermal radiation by scattering and absorption, cloud formation and precipitation, and air

quality degradation, which, in turn are relevant in shaping the Earth climate and liveability (Pope III et al., 2002; Akimoto, 2003; Pope III and Dockery, 2006; Monks et al., 2009; Boucher et al., 2013).

Despite its importance, the global aerosol radiative effect is far from being certain, as both aerosol spatial distribution and optical properties are affected by large unknowns (Boucher et al., 2013; Myhre et al., 2013). Furthermore, the apportionment of aerosols to anthropogenic~~ic~~ and natural sources is critical to evaluate the perturbative forcing of human activities on the Earth radiative budget and ultimately climate (Myhre et al., 2013; Shindell et al., 2013; Kim et al., 2014; Pan et al., 2015). In this general context, the Mediterranean basin is a region of great interest. Submitted to demographic pressure and experiencing bad air quality (Monks et al., 2009; Kovats et al., 2014), the Mediterranean is a high emission and transport region of all kinds of anthropogenic and natural aerosols (e.g. Moulin et al., 1998; Lelieveld et al., 2002; Pace et al., 2005 and 2006; Querol et al., 2009; Pey et al., 2013; Becagli et al., 2017), as well as one of the most vulnerable areas to climate change (Giorgi, 2006), with severe future warming leading to a reduction in precipitation~~s~~ and soil moisture, and henceforth a significant water stress towards the end of the century (Giorgi and Lionello, 2008; García-Ruiz et al., 2011; Christensen et al., 2013) and likely positive feedbacks on the aerosol load.

Through the years, the Mediterranean aerosols have been investigated through a number of dedicated local and regional scale experiments (e.g. Söderman and Dulac, 1998; Formenti et al., 2002; Lelieveld et al., 2002; Zerefos et al., 2002; Dulac and Chazette, 2003; Cros et al., 2004; Putaud et al., 2004, Mallet et al., 2016), surface monitoring stations and networks (e.g. Bergametti et al., 1989; Migon et al., 1993; Mihalopoulos et al., 1997; Meloni et al., 2007; di Sarra et al., 2008; Pérez et al., 2008; Querol et al., 2009; Kalivitis et al., 2011; Mallet et al., 2013; Pappalardo et al., 2014; Lyamani et al., 2015) and satellite observations (e.g. Dulac et al., 1992; Moulin et al., 1998; Barnaba and Gobbi, 2004; Antoine and Nobileau, 2006; Papadimas et al., 2008; Gkikas et al., 2009 and 2016). More recently, the regional-scale Chemistry-Aerosol Mediterranean Experiment (ChArMEx, http://charmex.lsce.ipsl.fr/) within the international Mediterranean Integrated STudies at Regional And Local Scales (MISTRALS, http://www.mistrals-home.org) program has significantly added to the

existing body of knowledge by providing new ground-based, airborne and balloon-borne observations over the western part of the basin (Mallet et al., 2016; see also this special issue).

ChArMEx has also provided a new momentum in the analysis of regional ground-based and satellite aerosol observations on long and short periods (e.g. Mallet et al., 2013; Nabat et al., 2013; Lyamani et al., 2015; Gkikas et al., 2016; Granados-Muñoz et al., 2016; Sicard et al., 2016). Satellite data are highly valuable to provide information on the regional and global aerosol spatial and temporal distribution and optical properties which are input to climate models. Most ~~satellite~~ multi-spectral imagery instruments (e.g., MODIS, SEAWIFS, AVHRR, SEVIRI…) retrieve the ~~A~~aerosol ~~O~~optical d~~D~~epth (*AOD*), representing the column-integrated optically-active content of atmospheric aerosols, and also proportional to the net change in the clear sky outgoing radiative flux at the top of the atmosphere (Boucher, 2015). ~~The~~ *AOD* is an essential parameter to establish the climatology of the distribution and effects of atmospheric aerosols and it is often used for model evaluation (e.g., Chin et al., 2002; Huneeus et al., 2011; Nabat et al., 2013). With this respect, advanced spaceborne retrievals deriving the AOD as a function of particle size and shape, and possibly of wavelength, are most useful in evaluating the origin and the radiative effect of aerosols of different nature.

In this paper, we present a first comprehensive quality-assessment study of the advanced dataset provided by the operational ~~retrieval~~ ocean retrieval algorithm of the third multi-spectral, multi-directional and polarized POLDER-3 (POLarization and Directionality of the Earth's Reflectances) radiometer on PARASOL (Polarization & Anisotropy of Reflectances for Atmospheric Sciences coupled with Observations from a Lidar) satellite (Herman et al., 2005; Tanré et al., 2011) over the western Mediterranean basin. POLDER-3 operated from March 2005 to October 2013 and provided the total, fine and coarse mode aerosol optical depth (*AOD*, AOD_F and AOD_C) at the wavelength of 865 nm, the spectral dependence of the AOD between 670 and 865 nm (Angström e~~E~~xponent, *AE*), and the partition of spherical and non-spherical AOD_C (AOD_{CS} and AOD_{CNS}, respectively). This paper extends previous evaluations of AOD and AOD_F (Goloub et al., 1999; Fan et al., 2008; Bréon et al., 2011) with a focus on the western Mediterranean basin, and provides the first estimate of the

Mis en forme : Police :Italique
Mis en forme : Police :Italique
Mis en forme : Police :Italique
Mis en forme : Police :Italique
Mis en forme : Police :Italique
Mis en forme : Police :Italique
Mis en forme : Police :Italique
Mis en forme : Police :Italique

significance of the coarse mode spherical and non-spherical components (AOD_C, AOD_{CS} and AOD_{CNS}).

This study is based on comparisons with co-localised observations from the sun/sky photometers of coastal and insular stations of the Aerosol Robotic Network (AERONET; Holben et al., 1998), and with the in situ measurements of vertical profiles of aerosol extinction and size distribution which were performed by the French ATR-42 environmental research aircraft of the Service des Avions Français Instrumentés pour la Recherche en Environnement (SAFIREafire, www.safire.fr) during twohe ChArMEx intensive campaigns (Di Biagio et al., 2016, Denjean et al., 2016, Mallet et al., 2016). In particular, the use of the size distribution vertical profiles measured in situ allows us to calculate the aerosol optical depth over different size ranges, and the evaluation of AOD_F and AOD_C.

The analysis presented in this paper is essential to geophysical analyses of observations by POLDER-3 of the spatial and temporal variability of the aerosol load over the western Mediterranean basin. This analysis, including the investigation of temporal trends over the 8-year operating period, will be presented in a follow-up dedicated paper (part II of the present manuscript).

2. Measurements

2.1. POLDER-3/PARASOL

The third radiometer POLDER-3 on PARASOL, operational from March 2005 to October 2013, was part of the A-Train constellation operated on a sun-synchronous orbit at 705 km crossing the Equator at 13:30 (Equator local time) (Tanré et al., 2011). In December 2009, it left the A-Train, and continued the observations at 3.9 km below, and at 9.5 km below in 2011. This changed its hour of passage, which was 16:00 Equator local time at the end of the operational period.

POLDER-3/PARASOL used a 274 x 242-pixels CCD detector array, each pixel covering 5.3 x 6.2 km² at nadir. The size of the POLDER-3 images was 2100 x 1600 km², allowing to achieve a global coverage within two days. The western Mediterranean area could be covered in less than 5 minutes along its north-to-south axis. The spatial resolution of POLDER-derived (Level 2) aerosol

Mis en forme : Police :Italique
Mis en forme : Police :Italique
Mis en forme : Police :Italique

parameters is about 18.5 x 18.5 km² (corresponding to 3 x 3 pixels of the Level-1 grid; http://www.icare.univ-lille1.fr/parasol/products).

The instrument measured ~~solar~~ Earth radiance at 9 wavelengths from 443 to 1020 nm, three of which with polarisation (490, 670, 865 nm), and at up to 16 different angles (±51° along, ±43° across track). Cloud screening according to Bréon and Colzy (1999) was applied to minimize possible cloud contamination of aerosol products.

In this paper, we used the latest algorithm update (collection 3) performed in 2014 of the operational clear-sky ocean retrieval algorithm (Deuzé et al., 1999, 2000; Herman et al., 2005). This latest version includes calibration improvements and uses the total and polarized radiances at 670 and 865 nm. For each clear sky pixel, the algorithm recalculates the observed polarized radiances at several observational angles from a Look-Up Table (LUT) built on aerosol micro-physical models. These are constructed as follows: (i) aerosol are not-absorbing, that is, the imaginary part m_i of their complex refractive index ($m = m_r - i\,m_i$) is ~~nul~~zero. Only the real part m_r is attributed, and considered as invariant with wavelength between 670 and 865 nm; (ii) the aerosol number size distribution is bimodal and lognormal with a fine mode with effective diameter (D_{eff}) smaller than 1.0 µm and a coarse mode with D_{eff} larger than 1.0 µm. The coarse mode includes a non-spherical fraction based on the spheroidal model from Dubovik et al. (2006). Collection 3 increases the number of modes with respect to the previous versions reported by Herman et al. (2005) and Tanré et al. (2011), and allows spheroidal D_{eff} to take two values (2.96 or 4.92 µm). The summary of LUT parameters are presented in the supplementary material (**Table S1**).

The calculations of the multi-spectral, multi-angle polarized radiances are done using a Mie model for homogeneous spherical particles or the spheroidal optical model developed by Dubovik et al. (2006). A quality flag index (0 indicating the lowest and 1 the highest quality) is attributed to each pixel depending on the quality of radiance simulation.

In this paper, we target the following POLDER-3 oceanic (i.e. over ocean surfaces) aerosol products, in which AODs are at 865 nm:

Mis en forme : Police :Italique
Mis en forme : Police :Italique
Mis en forme : Police :Italique
Mis en forme : Police :Italique
Mis en forme : Police :Italique
Mis en forme : Police :Italique

- The total aerosol optical depth (*AOD*),and the Ångström Exponent (*AE*) representing the spectral dependence of AOD, and calculated as

$$AE = -\frac{\ln(\mathrm{AOD}_{865}/\mathrm{AOD}_{670})}{\ln(865/670)} \quad (1)$$

- The aerosol optical depth due to the fine particle mode (AOD_F)

all obtained for clear-sky pixels.

In addition, for favourable viewing geometries (scattering angles between 90° and 160°), we have enough information to consider that the coarse mode is a mixing of spherical and non-spherical particles. We assume that the fraction of non-spherical particles (f_{CNS}) of the coarse mode (AOD_c) can be equal to 5 discrete values (0, 0.25, 0.50, 0.75, 1.0). Then, the AOD_{CNS} (respectively AOD_{CS}) is derived from

$$AOD_{CNS} = f_{CNS} \times AOD_C \quad (2\text{-a})$$

$$AOD_{CS} = (1-f_{CNS}) \times AOD_C \quad (2\text{-b})$$

-

- ~~And the aerosol optical depth due to the spherical (AOD_{CS}) and non-spherical (AOD_{CNS}) coarse mode fractions, obtained for clear-sky pixels with favourable viewing geometries (scattering angles between 90° and 160°). These products allow estimating the fraction of non-spherical particles in the coarse mode AOD (f_{CNS}) from~~

~~$$f_{CNS} = AOD_{CNS} / (AOD_{CNS} + AOD_{CS}) \quad (2)$$~~

~~Whereas AOD_F was available for all clear-sky pixels regardless of the geometry of observations, the AOD_C was estimated in two ways depending on the availability of observations.~~

~~For days with observations in favourable viewing geometrical conditions, AOD_C was calculated as the sum of measured AOD_{CS} and AOD_{CNS}. For the remaining days,~~ AOD_C can also be calculated ~~was~~

Mis en forme : Police :Italique
Mis en forme : Police :Italique
Mis en forme : Police :Italique
Mis en forme : Normal, Sans numérotation ni puces
Mis en forme : Justifié, Interligne : Double
Mis en forme : Anglais (États-Unis)
Mis en forme : Police :Italique
Mis en forme : Police :Italique
Mis en forme : Police :Italique
Mis en forme : Police :Italique
Mis en forme : Anglais (États-Unis)
Mis en forme : Police :Italique
Mis en forme : Droite
Mis en forme : Police :Italique, Indice
Mis en forme : Police :Italique
Mis en forme : Police :Italique, Indice
Mis en forme : Police :Italique
Mis en forme : Police :Italique, Indice
Mis en forme : Police :Italique
Mis en forme : Police :Italique, Indice
Mis en forme : Police :Italique
Mis en forme : Police :Italique, Indice
Mis en forme : Police :Italique
Mis en forme : Police :Italique, Indice
Mis en forme : Normal, Sans numérotation ni puces
Mis en forme : Police :Italique

~~calculated~~ as $AOD–AOD_F$. A maximum difference of ±0.002 due to rounding errors was found for days when both methods are applicable.

Only the POLDER-3 aerosol products from pixels with a quality flag index ≥0.5 have been considered in the following discussion.

2.2. AERONET

AERONET is a global network of ground-based multi-spectral sun/sky photometers (Holben et al., 1998; 2001) dedicated to real time monitoring of aerosol properties and widely used as ground-based reference for validation of aerosol satellite retrievals (e.g., Goloub et al., 1999; Bréon et al., 2011). It uses standardized sun/sky photometers (CIMEL CE-318, Cimel Electronique, Paris) measuring solar extinction and sky radiances (at times with polarization) in the almucantar plane at wavelengths between 340 and 1020 nm (most commonly 440, 675, 870, and 1020 nm), that allow deriving a number of aerosol optical and microphysical parameters (Dubovik and King, 2000; Dubovik et al., 2006).

AOD and *AE* are obtained about every 15 minutes from the measurement of the direct sun extinction and are reported as the average of a triplet of acquisitions lasting approximately 30 s. We consider here AERONET *AOD* at 870 nm and the *AE* value obtained between 870 and 675 nm. For freshly calibrated and well maintained instruments, the accuracy in AOD is of the order of 0.01-0.02 regardless of the AOD value (Holben et al., 1998). The aerosol optical depth in the fine and coarse mode (AOD_F and AOD_C, respectively) are recalculated from the column-integrated particle volume size distribution retrieved between 0.1 and 30 µm in diameter by the inversion algorithm described in Dubovik and King (2000) and Dubovik et al. (2006). The fine and coarse modes of the retrieved volume size distribution are defined as the modes below and above a threshold diameter ($D_{cut\text{-}off}$) corresponding to the minimum ~~of~~ in the particle size distribution. The $D_{cut\text{-}off}$ value is not fixed but can vary between 0.44 and 0.99 µm. AOD_F and AOD_C values are estimated by recalculating the extinction due to the fine and coarse modes of the aerosols. The latest AERONET retrieval scheme considers an aerosol mixture of polydisperse, randomly-oriented homogeneous spheroids with a fixed distribution of aspect ratios (Mishchenko et al., 1997) and provides fraction (in percentage) of non-

Mis en forme : Police :Italique
Mis en forme : Police :Italique
Mis en forme : Police :Italique
Mis en forme : Police :Italique
Mis en forme : Police :Italique
Mis en forme : Police :Italique
Mis en forme : Police :Italique
Mis en forme : Police :Italique

spherical/spherical particles, i.e. f_{NS}/f_S (Dubovik et al., 2006). ~~By~~ For clear sky, there are about 10 measurements per day of this fraction in the early day or late afternoon (solar zenith angle ≥50°).

We used AERONET V2 level-2 quality assured aerosol products. Seventeen coastal AERONET stations, shown in **Figure 1,** were selected in this study, (see also **Table 1** for their respective geographical coordinates and covered periods). Their regional distribution covers the entire western Mediterranean basin, including south Europe (e.g., near coastal stations of Barcelona, Toulon, Villefranche-sur-Mer…), North Africa (Blida), and island locations in the northern (Ersa), central (Palma de Mallorca) and southern (Lampedusa and Alboran) basin, therefore capturing the diversity of the aerosol population, resulting from the different sources contributing to the Mediterranean aerosol (desert dust, marine, urban and industrial pollution, and biomass burning). The dataset also includes the ground-based super-sites of Ersa and Lampedusa of the ChArMEx project (Mallet et al., 2016). Considering the 17 stations altogether, more than 18000 daily observations of AOD are available in total in both POLDER-3 and AERONET datasets, among which 6421 are concurrent (see section 3.2 below) and thus available for comparison. We did not consider for tentative matching with POLDER in this study a rather limited number (<100) of daily observations obtained from manual sun-photometers on-board ships in our area (Figure 1) and period of interest, which are also available from the Maritime Aerosol Network component of AERONET (Smirnov et al., 2011).

2.3. ChArMEx airborne measurements

The airborne measurements relevant to this paper were performed on-board the French ATR-42 environmental research aircraft of SAFIRE~~afire~~ during two of the intensive observational periods of the ChArMEx project:

- The Transport and Air Quality (TRAQA) campaign, dedicated to the study of air pollutants transport from Europe to the Mediterranean, their evolution and their impact on regional air quality (Di Biagio et al., 2015; 2016; Nabat et al., 2015a; Rea et al., 2015);
- The Aerosol Direct Radiative Forcing on the Mediterranean (ADRIMED) campaign was dedicated to the characterization of aerosol optical properties in the Mediterranean and their direct radiative effect in clear sky conditions (Denjean et al., 2016; Mallet et al., 2016).

During TRAQA, the ATR-42, based at the Francazal airport near Toulouse, France (43°36'N, 1°26'E), conducted 17 flights from 20 June to 13 July 2012 encountering weather conditions favouring the transport of pollution aerosols from continental Europe, and particularly from the Rhone valley, the Gulf of Genoa and Barcelona, giving raise to AOD values in the range of 0.2-0.6 at 550 nm over the northwestern Mediterranean. From 17 to 23 June, and then on 29 June, two episodes of desert dust transport were observed in the free troposphere, increasing the AOD up to 1.4 on June 29. (Di Biagio et al., 2015; 2016). During ADRIMED, the ATR-42, based in Cagliari, Italy (39°15'N, 9°03'E), flew 16 scientific flights between 14 June and 4 July 2013 (Denjean et al., 2016; Mallet et al., 2016). Several episodes of desert dust transport from southern Algeria and Morocco and northern Algeria and Tunisia were observed over the western and central Mediterranean, particularly off the Balearic Islands and above the Lampedusa island offshore Tunisia (Denjean et al., 2016).The total optical depth at 550 nm remained moderate, in the order of 0.2-0.4 even during dust events (Mallet et al., 2016).

2.3.1. Airborne instrumentation measuring aerosol optical properties

2.3.1.1. PLASMA photometer

PLASMA (Photomètre Léger Aéroporté pour la Surveillance des Masses d'Air), developed by LOA (Laboratoire d'Optique Atmospherique, Lille), is a multi-spectral sun-photometer which measures the direct sun radiance and retrieves the AOD at 15 wavelengths between 343 and 2250 nm, including 869 nm (Karol et al., 2013). The estimated uncertainty ranges between 0.005 and 0.01 (Karol et al., 2013). PLASMA was operated during the ADRIMED campaign only, when it was mounted on the roof of the ATR-42, allowing the retrieval of a vertical profile of both the spectral AOD and the aerosol particle size distribution (Torres et al., 2017).

2.3.1.2. CAPS-PMex

The Cavity Attenuated Phase Shift in situ instrument (CAPS-PMex, Aerodyne Research Inc.) measures the extinction coefficient σ_{ext} at 532 nm with an estimated relative uncertainty of ±3.2% (Kebabian et al., 2007; Massoli et al., 2010; Petzold et al., 2013). The operating principle is based on the modulation of the frequency and the phase changes of the light emitted by a LED source due to

Mis en forme : Police :Italique

aerosols, after correction of the Rayleigh scattering by the molecules present in the air mass. As described in Denjean et al. (2016), the instrument was available during the ADRIMED campaign only, when it was located inside the cabin behind the Communautary Aerosol Inlet (CAI), and operated at 0.85 L min^{-1} and with a temporal resolution of 1 second. In this paper, the extinction coefficient σ_{ext} is expressed in Mm^{-1} (1 Mm^{-1} = 10^{-6} m^{-1}).

2.3.1.3. Nephelometer

The scattering coefficient σ_{scatt} at 450, 550 and 700 nm was measured by a spectral integrating nephelometer (model 3563, TSI Inc.) described extensively by Anderson et al. (1996) and Anderson and Ogren (1998). During both TRAQA and ADRIMED, the instrument was operated at 30 L min^{-1} with a temporal resolution of 1-2 seconds downstream the AVIRAD inlet also onboard the ATR-42 (Di Biagio et al., 2015; 2016; Denjean et al., 2016). The AVIRAD inlet estimated size cut-off, corresponding to the diameter at which particles are collected with a 50% efficiency, is 12 µm in optical diameter.

The instrument uses a halogen lamp as light source and three photomultipliers preceded by spectral filters. Due to the geometry of its sensing volume, the nephelometer measures the scattering coefficient (σ_{scatt}) between 7° and 170° and the backscattering coefficient (σ_{bscatt}) between 90° and 170°. The scattering Angström exponent (AE_{scatt}) ~~and~~ representing the scattering spectral dependence ~~car~~ can be calculated as

$$\mathbf{AE_{scatt}} = -\frac{\mathbf{ln(\sigma_{scatt,450}/\sigma_{scatt,700})}}{\mathbf{ln(450/700)}} \quad (3)$$

The relative uncertainty in σ_{scatt} due to calibration, counting statistics and non-idealities of detector surfaces, is estimated to be ±1-2% for submicron aerosols and ±8-15% for supermicron aerosols (Müller et al., 2009). To these values usually adds the error related to the geometric truncation of the measured angular range of the scattering phase function due to the sensing volume (Anderson and

Mis en forme : Police :Italique

Mis en forme : Police :Italique

Mis en forme : Police :Italique

Mis en forme : Police :Italique

Ogren, 1998). This truncation induces an underestimation of σ_{scatt} and σ_{bscatt}, which depends on the angular distribution of the scattered light, and thus on particle size. Anderson and Ogren (1998) have shown that the uncertainty induced by the underestimation of σ_{scatt} can be parameterized by the scattering spectral dependence for submicron aerosols. This parameterization is not possible for aerosols of larger particle size (diameter greater than 1 µm), because the Angström exponent~~coefficient~~ tends to zero whereas the underestimation is important (50-60%) because of the increase of the forward scattering. In this case, the correction is performed by optical calculation if the particle size distribution and refractive index are known (Müller et al., 2009; Formenti et al., 2011). As for σ_{ext}, in this paper σ_{scatt} is expressed in Mm^{-1}.

Mis en forme : Police :Italique
Mis en forme : Police :Italique
Mis en forme : Police :Italique
Mis en forme : Police :Italique
Mis en forme : Police :Italique

2.3.2. Aerosol particle size distribution

Because of its extent, the aerosol particle size distribution is measured in situ by the combination of several instruments, often based on different physical principles (Wendisch and Brenguier, 2013). In our work, we used a combination of different optical counters operating on the fine and coarse modes of the aerosols, that is:

- a Passive Cavity Aerosol Spectrometer Probe (PCASP, Droplet Measurement Technologies, Boulder, Colorado), operated at 632.8 nm with a temporal resolution of 1 second. The PCASP measures light scattering between 35 and 135° to derive the particle number size distribution over 31 channels between 0.1 and 3.0 µm in diameter (Liu et al., 1992; Reid et al., 1999). The PCASP was operated on a wing pod of the ATR-42 during the TRAQA campaign only.
- an Ultra High Sensitivity Aerosol Spectrometer (UHSAS, Droplet Measurement Technologies, Boulder, Colorado), operated at 1054 nm with a temporal resolution of 1 second. The UHSAS measures light scattering between 22 and 158° to derive the particle number size distribution over 99 size channels between 0.04 and 1.0 µm in diameter (Cai et al., 2008). The UHSAS replaced the PCASP under the aircraft wing during the ADRIMED campaign.
- a Sky-Grimm counter (1.129 model, Grimm Aerosol Technik; Grimm and Eatough, 2009), operated at 632.8 nm with a temporal resolution of 6 seconds. The instrument integrates light scattering between 30° and 150° to derive the particle number size distribution over 32

channels between 0.25 and 30 µm in diameter (Grimm and Eatough, 2009). The instrument was available during both TRAQA and ADRIMED, operated inside the aircraft cabin and behind the AVIRAD inlet. Due to a flow problem, measurements during TRAQA are restricted to the portions of the flights when the ATR-42 remained below 350 m above sea level.

3. Validation strategy

3.1. Matching POLDER-3 and in situ aircraft measurements

In situ aircraft measurements provided direct and indirect observations for validation. Direct observations of the total *AOD* were obtained by the reading of the PLASMA sun-photometer for those portions of the flights when the ATR-42 flew at its lowest altitude and by integrating the vertical profile of the extinction coefficient σ_{ext} measured by the CAPS-PMex instrument between the minimum and the maximum heights (z_{min} and z_{max}) of the ATR-42 during profile ascents or descents.

Indirect validation of the size-dependent optical depth (*AOD*, AOD_F and AOD_C) was performed by optical calculation from the number size distribution $dN(D,z)/d\log D$ measured by the combination of the PCASP, UHSAS and Grimm optical counters as

$$\mathrm{AOD_x}\ (865\ \mathrm{nm}) = \int_{z_{min}}^{z_{max}} dz\ \sigma_{ext}(z) = \int_{z_{min}}^{z_{max}} dz \int_{D_{x'}}^{D_x} \pi D^2 Q_{ext}(z, D, m) \frac{dN(D,z)}{d\log D} d\log D \quad (4)$$

The suffix x in Equation 4 indicates the size domain of the aerosol optical depth (total, fine or coarse) considered in the calculations.

Equation 4 allows one to estimate the aerosol optical depth over a variable size domain, whose boundaries (D_{min} and D_{max}) can be adjusted to represent the fine and the coarse modes, as well as the total particle size distribution.

The iterative procedure used for the calculation is presented in **Figure S12**. All calculations used the optical Mie theory for homogeneous spherical particles (Mie, 1908). The initial step of the procedure consisted in estimating the aerosol number size distribution, input of Equation 4, from the

Mis en forme : Police :Italique
Mis en forme : Police :Italique
Mis en forme : Police :Italique
Mis en forme : Police :Italique
Mis en forme : Police :Italique
Mis en forme : Police :Italique
Mis en forme : Police :Italique
Mis en forme : Police :Italique
Mis en forme : Police :Italique
Mis en forme : Police :Italique
Mis en forme : Police :Italique
Mis en forme : Police :Italique

measurements of the PCASP, UHSAS and Grimm optical counters operated on board the ATR-42 during TRAQA and ADRIMED. This required two actions, described in details in the Supplementary material.

1. The conversion of the nominal “optical equivalent spherical diameter" (D_{EO}) characteristic of each particle counter to a "geometric equivalent spherical diameter" (D_{EG}). The operating principle of the particle optical counters is based on the angular dependence of the light scattering intensity to the particle size (Wendisch and Brenguier, 2013). The proportionality factor between angular light scattering and particle size depends on the particle complex refractive index. At calibration, the optical particle counters provide ~~with "~~an “optical equivalent spherical diameter" (D_{EO}), corresponding to the diameter of standard material, generally spherical latex beeds, which refractive index (m_{latex} = 1.59-0i) is usually different from the real aerosol refractive index measured in the atmosphere. It is therefore necessary to convert the measured D_{EO} value into a so-called "geometric equivalent spherical diameter" (D_{EG}) value taking into account the actual refractive index of ambient particles.
2. The combination of measurements over different size ranges. Since no optical counter completely covers the full size range of atmospheric aerosol particles, measurements of the PCASP, UHSAS and Grimm were combined by examining their agreement on their size overlap domains. When successful, the particle number size distribution obtained by the combination was normalised to the total particle number and fitted using a multi-mode lognormal distribution to eliminate discontinuities and extend the representation beyond the lower and upper operating size ranges of the optical counters.

The capability of the derived number size distributions to represent the aerosol extinction coefficient, henceforth to estimate aerosol optical depth, was assessed by comparing the calculated extinction and scattering coefficients σ_{ext} and σ_{scatt} to the measurements of the CAPS-PMex and the nephelometer at 450, 532, 550 and 700 nm. The scattering coefficient σ_{scatt} was calculated by integrating the scattering phase function between 7° and 170°, corresponding to the aperture of the sensing volume of the nephelometer.

Mis en forme : Police :Italique
Mis en forme : Police :Italique
Mis en forme : Police :Italique
Mis en forme : Police :Italique
Mis en forme : Police :Italique
Mis en forme : Police :Italique
Mis en forme : Police :Italique
Mis en forme : Police :Italique
Mis en forme : Police :Italique

All optical calculations performed in this paper assumed the spectral complex refractive index m, representing the aerosol composition, as independent of size. An initial dataset per aerosol type was chosen (Table S2 in the Supplementary material). The calculations were iterated by varying the initial values of the complex refractive indices until both 1/ the adjusted value for the calculation of the extended size distributions and 2/ the comparison between calculations and measurements of the extinction and scattering coefficients agreed within errors. Results of these comparisons are presented in the Supplementary material.

3.2. Constitution of the data set

This section describes the choices of temporal and spatial coincidences adopted for the comparisons between POLDER-3, AERONET and in situ data.

3.2.1. Coincidence with AERONET

As described in previous evaluation studies of aerosol products derived from satellites (e.g., Bréon et al., 2011), two approaches can be considered in order to compare coincident ground-based photometer and satellite aerosol data. One option is to select only the closest (in time) photometer measurement and the closest (in distance) satellite pixel from the photometer site. Another method consist in performing averaging within a certain time window for photometer data, and a spatial average of the satellite data within a given distance from the photometer site. Bréon et al. (2011) have shown that these two approaches give very comparable results for POLDER-3 aerosol products over oceans. In this study we adopted the second approach, considering the POLDER-3 aerosol products from pixels within ±0.5° around the AERONET sites. For AERONET *AOD* and *AE*, the averaging temporal window was set to ±1 h around the time of the POLDER-3 passage. For AERONET AOD_F, AOD_C, and shape retrieval, this temporal window produces an insufficient number of data, in particular for springs and summers in the period 2005-2011 due to the temporal time shift of the POLDER-3 passage towards the afternoon. ~~Instead~~For these two variables, the averaging temporal window was extended to the whole afternoon (that is, all data points later than 12:00 UTC) in order to allow for a significant dataset for comparison.

Mis en forme : Police :Italique
Mis en forme : Police :Italique
Mis en forme : Police :Italique
Mis en forme : Police :Italique

Table 1 reports the number of available observational days for POLDER-3 and AERONET aerosol parameters at each station in the period March 2005-October 2013, as well as the number of coincident days obtained between POLDER-3 and AERONET. The stations are ranged regarding the number of coincident days obtained for *AOD* and *AE*, this number representing the upper limit of the number of common POLDER-3/AERONET observations days available. Including all 17 stations, 18634 occurrences of comparable POLDER-3 and AERONET observations are available for *AOD*, *AE*, AOD_F and AOD_C, and 7923 occurrences for AOD_{CS} and AOD_{CNS}, due to specific constraints on geometric conditions in the POLDER-3 algorithm necessary to derive shape-related parameters (non sphericity). Per site, the number of clear sky observational days for POLDER-3-derived *AOD*, *AE*, AOD_F and AOD_C varies from 668 to 1392. Part of this variability also depends on the percent of sea pixels in the 1° x 1° area around the sites, which is lower for coastal (e.g., Burjassot or Roma) than insular stations (e.g., Alboran, Lampedusa or Gozo). Between 1 pixel in the case of inland stations of Roma and Burjassot, and up to 29 pixels in the case of the small remote island of Alboran were considered. Overall, the number of available AERONET observation days is important both for *AOD* and *AE* (18223), and AOD_F and AOD_C (11228). The number of days with AERONET-derived f_{NS} was less significant (4976 data points), due to additional constrains in the inversion necessary to derive this parameter.

The number of available AERONET observations per site varied from 158 to 2059 for *AOD* and *AE*, and from 43 to 1333 for AOD_F and AOD_C, mainly due to partial functioning of the instruments or maintenance of the sites. At some stations, measurements started years after the beginning of POLDER-3 mission (e.g., 2011 for Alboran, 2013 for Gozo). Finally, the number of POLDER-3/AERONET coincident days available for analysis is 6421 for *AOD* and *AE*, 3855 for AOD_F and AOD_C, and 730 for the percentage of spherical coarse particles (f_{NS}).

3.2.2. Coincidence with airborne observations

The comparison between POLDER-3 and airborne measurements was conducted for profile ascents or descents of the ATR-42 close in time with POLDER-3 overpasses. Flight tracks and profiles locations are shown in **Figure 3**2, whereas additional details (dates, geographical coordinates,

Mis en forme : Police :Italique
Mis en forme : Police :Italique
Mis en forme : Police :Italique
Mis en forme : Police :Italique
Mis en forme : Police :Italique
Mis en forme : Police :Italique
Mis en forme : Police :Italique
Mis en forme : Police :Italique
Mis en forme : Police :Italique
Mis en forme : Police :Italique
Mis en forme : Police :Italique
Mis en forme : Police :Italique
Mis en forme : Police :Italique
Mis en forme : Police :Italique
Mis en forme : Police :Italique
Mis en forme : Police :Italique
Mis en forme : Police :Italique
Mis en forme : Police :Italique
Mis en forme : Police :Italique
Mis en forme : Police :Italique

altitude span and duration) are given in **Table 2**. Data from the PLASMA sun-photometer, operated only during ADRIMED, were available only on 8 profiles (also indicated in Table 2) for which the minimum flight altitude was as close as possible to the surface. The data set was limited to ATR-42 profiles extending as much as possible over the column. To evaluate whether the aircraft profile sampled entirely or only partially the aerosol layers, we compared the *AOD* measured by PLASMA to that obtained by integrating the extinction profile of the CAPS-PMex instrument (not shown). By examining the AERONET time series, we also excluded episodes when the *AOD* had significantly varied in time between the POLDER-3 overpass and the aircraft profile. This mostly happened for cases when the aerosol optical depth exceeded 0.2 due to the transport of mineral dust (flights T-V22 and T-V23 during TRAQA and V31-S3 and V42-S2 during ADRIMED). The profiles discarded for comparison with POLDER-3 were used for the validation of the optical calculations presented in section 4 (not shown in Table 2 nor Figure ~~3~~2).

Prior to analysis, all in situ airborne data were synchronised and then averaged to 30 seconds to reduce the noise due to the native resolution of the measurements (1 to 6 seconds). POLDER-3 data were averaged over pixels within ±0.5° around the lowest altitude of each profile. In order to analyse the aerosol vertical stratification, we examined the magnitude of the scattering coefficient σ_{scatt} at 550 nm as a function of altitude and its spectral behaviour, represented by the scattering Angström Exponent (AE_{scatt}) measured by the airborne nephelometer. As in previous similar studies (Pace et al., 2006; Formenti et al., 2011; Di Biagio et al., 2015; 2016; Denjean et al., 2016), the aerosol layers were classified in four categories (clear/background maritime, desert dust, pollution, and mixture), following the criteria reported in **Table 3**. The mixture category, indicating mixing between desert dust and pollution, as observed by Denjean et al. (2016), was further detailed to distinguish dust-dominated layers (AE_{scatt} between 0.5 and 0.75) and pollution-dominated layers (AE_{scatt} between 0.75 and 1).

3.3. Statistical indicators

The agreement between the POLDER-3, AERONET and airborne datasets was quantified by several evaluation metrics, including the number of matchups (*N*), the linear correlation coefficient (*R*), the

Mis en forme : Police :Italique
Mis en forme : Police :Italique
Mis en forme : Police :Italique
Mis en forme : Police :Italique
Mis en forme : Police :Italique
Mis en forme : Police :Italique
Mis en forme : Police :Italique
Mis en forme : Police :Italique

slope (*S*) and intercept (*I*) of the linear regression, the root mean square error (*RMS*), and the bias (*B*), representing their mean difference.

$$RMS = \sqrt{\frac{1}{n}\sum_{i=1}^{n}(y_i - x_i)^2} \quad (5)$$

$$B = \frac{1}{n}\sum_{i=1}^{n}(y_i - x_i) \quad (6)$$

where x and y are generic datasets, and n the number of pairs of compared values.

Additional metrics is provided by the "fraction of accurate retrievals" (G_{frac}) defined by Bréon et al. (2011). This quantity is defined as

$$G_{frac} = \frac{\#obs(\Delta < EE)}{\#obs} \quad (7)$$

and quantifies the fraction of POLDER-3 data points for which the absolute difference (Δ) between reference and evaluated data is lower than the estimated error (*EE*).

In accordance to Bréon et al. (2011), EE was calculated as

$$EE = \pm (0.03 + 0.05 \times AOD) \quad (8)$$

and applied to all the *AOD* advanced products. Because G_{frac} is only appropriate for large datasets whose number of data points exceeds 100 (Bréon et al., 2011), it was calculated only for comparisons with AERONET data.

4. Results

4.1. Evaluation of the total aerosol optical depth

Figure ~~4~~ 3 shows the results of comparison of the *AOD* retrieved by POLDER-3 between 2005 and 2013 with respect to the 6421 observations at the seventeen AERONET stations and those on the

Mis en forme : Police :Italique
Mis en forme : Police :Italique
Mis en forme : Police :Italique
Mis en forme : Police :Italique
Mis en forme : Police :Italique
Mis en forme : Police :Italique
Mis en forme : Police :Italique
Mis en forme : Police :Italique
Mis en forme : Police :Italique
Mis en forme : Police :Italique
Mis en forme : Police :Italique
Mis en forme : Police :Italique
Mis en forme : Police :Italique

vertical profiles of the ChArMEx campaigns (PLASMA sun-photometer and calculations from the in situ size distributions).

The comparison with AERONET shows a good correlation (regression coefficient R = 0.88, G_{frac} = 73%), with a statistically low dispersion and bias (RMS = 0.04, B = 0.003). Twenty-seven percent of the observations do not meet the criteria of the G_{frac} parameter. Cases outside the G_{frac} boundary were characterized by large standard deviations, either because the spatial distribution of AOD was heterogeneous in the 1° x 1° area of the pixels surrounding the AERONET sites, or because it varied significantly on the time window of ±1 hour around the POLDER-3 overpass. In our dataset, the highest value of AOD ~~measured~~ retrieved by POLDER-3 was 1.4 (±0.1) during a desert dust transport event over Lampedusa observed on April 25, 2011. This is the only event coincident with an AERONET measurement (1.50 ±0.06) with POLDER-3 AOD >1.

Figure 3~~4~~ also shows the comparison with the PLASMA observations and with the calculations initiated by the measured airborne number size distributions.

On those, the AOD did not exceed 0.2, whereas AE ranged from 0.31 ±0.07 to 1.09 ±0.08, indicating that these cases are representative of aerosols of different origins. The comparison was also very satisfactory and confirmed the more extensive results from the comparison with AERONET-derived $AODs$. POLDER-3 provides higher values of AOD for mineral dust (lowest AE values) compared to those calculated from in situ aerosol measurements, which could reflect an underestimate of the coarse mode distribution from the in situ aircraft measurements. On the other hand, POLDER-3 tends to underestimate AOD with respect to PLASMA at low AE values, resulting in a negative bias of the correlation (~~bias~~ B = 0.02). In both cases, ~~the~~ RMS remained low and below 0.05.

4.2. Evaluation of fine and coarse aerosol optical depth

4.2.1. Comparison with AERONET observations

Figure 4~~5~~ shows the comparison between POLDER-3 and AERONET for AOD_F and AOD_C. AOD_F remained below 0.25, smaller than AOD_C, which reached 0.8. The correlation coefficient for AOD_C (R = 0.81) is closer to the correlation coefficient for AOD (0.88) than that for AOD_F (0.63). The

Mis en forme : Police :Italique
Mis en forme : Police :Italique
Mis en forme : Police :Italique
Mis en forme : Police :Italique
Mis en forme : Police :Italique
Mis en forme : Police :Italique
Mis en forme : Police :Italique
Mis en forme : Police :Italique
Mis en forme : Police :Italique
Mis en forme : Police :Italique
Mis en forme : Police :Italique
Mis en forme : Police :Italique
Mis en forme : Police :Italique
Commenté [d1]: A confirmer par Didier:
This might be due to the small absorption of dust particles, which is not taken into account in the aerosol models of the POLDER inversion look-up table.
Mis en forme : Police :Italique
Mis en forme : Police :Italique
Mis en forme : Police :Italique
Mis en forme : Police :Italique
Mis en forme : Police :Italique
Mis en forme : Police :Italique
Mis en forme : Police :Italique
Mis en forme : Police :Italique
Mis en forme : Police :Italique
Mis en forme : Police :Italique
Mis en forme : Police :Italique

agreement between POLDER-3 and AERONET is confirmed by the G_{frac} values of 74% for AOD_C and 88% for AOD_F, the low statistical bias (-0.007 for AOD_F and 0.01 for AOD_C), and the moderate dispersion (RMS values between 0.02 for AOD_F and 0.04 for AOD_C). The weaker correlation and the dispersion observed for AOD_F can be attributed to the difficulty in retrieving low values of optical depth. Additionally, Tanré et al. (2011) pointed out that differences could arise by the definitions of the cut-off diameter ($D_{cut\text{-}off}$) used in the POLDER-3 and AERONET retrievals to estimate AOD_F. In the AERONET retrievals, AOD_F is calculated from the fine mode of the particle size distribution defined for a value of $D_{cut\text{-}off}$ forced between 0.44 and 0.99 µm. In the POLDER-3 algorithm, AOD_F is calculated from the full particle size distribution of the retrieved fine mode, without cuf-off. However, because of its use of polarisation, POLDER-3 is the most sensitive to particles smaller than 0.6-0.8 µm in diameter (Tanré et al., 2011 and references therein).

In **Figure ~~6~~5**, we explore the relevance of this difference in the comparison of AOD_F and AOD_C by further separating days when AERONET $D_{cut\text{-}off}$ <1.0 µm and days when $D_{cut\text{-}off}$ ≥1.0 µm. The threshold value of 1.0 µm corresponds to the D_{eff} of all the fine modes in the POLDER-3 LUT. Cases with $D_{cut\text{-}off}$ <1.0 µm were more numerous (2413 days), and showed a better agreement (~~bias~~ *B* = -0.003, G_{frac} = 91%, *RMS* = 0.02, *R* = 0.60). Data corresponding to $D_{cut\text{-}off}$ ≥1.0 µm were less numerous (1442 days). Whereas the correlation improved slightly (*R* = 0.69 versus *R* = 0.60), the dispersion increased (~~bias~~ *B* = -0.01, *RMS* = 0.03) due to the appearance of points for which AERONET AOD_F almost doubled that of POLDER-3. Colouring the data points by *AE* showed that the data points with $D_{cut\text{-}off}$ below 1.0 µm mostly corresponded to aerosols with a weak-to-moderate spectral dependence (low *AE*), whereas cases with $D_{cut\text{-}off}$ above 1.0 µm mostly (but not exclusively) corresponded to aerosols with a moderate-to-strong spectral dependence (high *AE*).

The size cut-off definition also affects the comparison for AOD_C. For $D_{cut\text{-}off}$ <1.0 µm, AOD_C values were high and the correlation was significant. Conversely, AOD_C remained low (≲0.2) when $D_{cut\text{-}off}$ ≥1.0 µm. This is consistent with the fact that the contribution of AOD_C to *AOD* decreases as the $D_{cut\text{-}off}$ increases (**Figure ~~S1~~ S2** in the supplementary material). **Figure ~~6~~ 5** shows that discriminating data on the basis of $D_{cut\text{-}off}$ results in attributing AOD_F and AOD_C to different aerosol types.

Mis en forme … [1]
Mis en forme … [2]
Mis en forme … [3]
Mis en forme … [4]
Mis en forme … [5]
Mis en forme … [6]
Mis en forme … [7]
Mis en forme … [8]
Mis en forme … [9]
Mis en forme … [10]
Mis en forme … [11]
Mis en forme … [12]
Mis en forme … [13]
Mis en forme … [14]
Mis en forme … [15]
Mis en forme … [16]
Mis en forme … [17]
Mis en forme … [18]
Mis en forme … [19]
Mis en forme … [20]
Mis en forme … [21]
Mis en forme … [22]
Mis en forme … [23]
Mis en forme … [24]
Mis en forme … [25]
Mis en forme … [26]
Mis en forme … [27]
Mis en forme … [28]
Mis en forme … [29]
Mis en forme … [30]
Mis en forme … [31]
Mis en forme … [32]
Mis en forme … [33]
Mis en forme … [34]
Mis en forme … [35]
Mis en forme … [36]
Mis en forme … [37]
Mis en forme … [38]
Mis en forme … [39]
Mis en forme … [40]
Mis en forme … [41]
Mis en forme … [42]
Mis en forme … [43]
Mis en forme … [44]
Mis en forme … [45]
Mis en forme … [46]
Mis en forme … [47]

4.2.2. Comparison with airborne measurements

To understand further the previous comparisons, POLDER-3 AOD_F and AOD_C were recalculated from the measured number size distributions (Equation 4) by varying the lower limit of the size integration between 0.4 and 1.0 µm in diameter with a step of 0.2. Results are shown in **Figure ~~7~~6**. As expected, the comparison for AOD_F is very sensitive to the size range. The best agreement between the retrieved and the calculated AOD_F is obtained for $D_{cut\text{-}off}$ between 0.6 and 0.8 µm, both showing high correlation coefficient R and low RMS. Conversely, the AOD_C comparison is almost independent of the value of $D_{cut\text{-}off}$ but more affected by the upper limit of the size range in Equation 4.

4.3. Evaluation of the Ångström Exponent

Figure ~~7~~8 shows the comparison of AE retrieved by POLDER-3 with values obtained by AERONET, PLASMA and the optical calculations. The comparison with AERONET was restricted to days when the POLDER-3 AOD exceed 0.1 (2031 out of the 6421 data points) to take into account only those values with relative uncertainties within 50%. The comparison showed a significant spread and a moderate correlation coefficient (R = 0.70). However, POLDER-3 tends to underestimate values of AE larger than 1 with respect to AERONET, and overestimate values smaller than 0.5, yielding a significant bias (–0.11). The values obtained by POLDER-3 compare well with the airborne observations of PLASMA (R = 0.84), but less well to the optical calculations (R = 0.42). In both cases, the bias is positive (0.1 with PLASMA and 0.2 with in situ AE). This fact, observed previously by Goloub et al. (1999) and Tanré et al. (2011), can be explained by considering that the values of AE are calculated from the retrieved AOD at 865 and 670 nm (Equation 1), which, in the ocean retrieval algorithm of POLDER, is obtained by the fit of measured radiances. The current aerosol models in the LUT (modal diameters and real part of the refractive index) provide AE values in the range –0.18 to 3.3. However, the extreme values are obtained only if the size distribution allowing to match the observed radiances consists of a single mode of non-spherical coarse particle (modal diameter of 0.9 µm for AE = –0.18) or a single mode of fine spherical particles (modal diameter of 0.08 µm for AE = 3.3). **Figure ~~9~~8** compares the scatterplots of AE and AOD obtained for the coincident POLDER-3 and AERONET datasets. The tendency of POLDER-3 to underestimate AE shows up clearly by the

Mis en forme : Police :Italique
Mis en forme : Police :Italique
Mis en forme : Police :Italique
Mis en forme : Police :Italique
Mis en forme : Police :Italique
Mis en forme : Police :Italique
Mis en forme : Police :Italique
Mis en forme : Police :Italique
Mis en forme : Police :Italique
Mis en forme : Police :Italique
Mis en forme : Police :Italique
Mis en forme : Police :Italique
Mis en forme : Police :Italique
Mis en forme : Police :Italique
Mis en forme : Police :Italique
Mis en forme : Police :Italique
Mis en forme : Police :Italique

absence of values of *AE* larger than 2.5, which, conversely, are retrieved by AERONET. On the other end of the spectrum, values down to –0.5 are found in the AERONET data set when POLDER-3 hardly retrieves negative values. Both POLDER-3 and AERONET show a trend with the largest AOD values at lower *AE* values. However, high *AOD* values (>0.9) are found with POLDER but not AERONET, and are all except one associated to relatively low *AE* (<1). Because the cloud screening of AERONET is relatively robust thanks to triplet measurements (Smirnov et al., 2000), these outliers may result from undetected cloud contamination in the POLDER algorithm.

4.4. Evaluation of aerosol sphericity

When the geometrical conditions of observations are favourable, the coarse mode optical depth (AOD_C) retrieved by POLDER-3 is quantified and apportioned into a spherical and a non-spherical fraction (AOD_{CS} and AOD_{CNS}, respectively). These products are potentially very useful in discriminating the mineral dust contribution, dominated by non-spherical coarse particles (e.g., Dubovik et al., 2002; Chou et al., 2008), when marine aerosols can be considered as spherical at relative humidities characteristics of coastal and open-sea sites (Sayer et al., 2012a; 2012b).

As a prerequisite, we investigated the comparison between POLDER-derived f_{CNS} (percent fraction of non-sphericity in the coarse mode AOD_C, that is, $f_{CNS} = AOD_{CNS}/(AOD_{CNS}+AOD_{CS})$ retrieved by POLDER-3 and f_{NS} (percent of non-sphericity of the total *AOD*) estimated by AERONET. In the operational ocean algorithm, f_{CNS} can only take ~~is a~~ discrete values equal to 0, 0.25, 0.50, 0.75, and 1. ~~, but the~~ The averaging process produces intermediate values when there is local variability between the pixels around a given AERONET station

In general, the POLDER-3 f_{CNS} and the AERONET f_{NS} are poorly correlated. The correlation coefficient *R* is 0.29 for the coincident data points of all the 17 stations ($N = 730$, **Table 1**). At individual coastal and insular stations (Lampedusa and Malaga), notably impacted by mineral dust ~~the coastal and insular ones such as Lampedusa and Malaga~~, the correlation between POLDER-3 f_{CNS} and AERONET f_{NS} is more significant ($R = 0.73$ for $N = 54$ and $R = 0.59$ for $N = 53$, respectively). This is also seen when restricting the data set of Ersa and Lampedusa to the summers of 2012 and 2013 ($R = 0.55$ at Ersa, $N = 11$; $R = 0.70$ at Lampedusa, $N = 10$).

Mis en forme : Police :Italique

Mis en forme : Police :Italique

Mis en forme : Police :Italique

Mis en forme : Police :Italique

Mis en forme : Police :Italique

Mis en forme : Police :Italique

Mis en forme : Police :Italique

Mis en forme : Police :Italique

Mis en forme : Police :Italique

Mis en forme : Police :Italique

Mis en forme : Police :Italique

Mis en forme : Police :Italique

Mis en forme : Police :Italique

Mis en forme : Police :Italique

Mis en forme : Police :Italique

Mis en forme : Police :Italique

Mis en forme : Police :Italique

Mis en forme : Police :Italique

Mis en forme : Police :Italique

Mis en forme : Police :Italique

Mis en forme : Police :Italique

Mis en forme : Police :Italique

Mis en forme : Police :Italique

Mis en forme : Police :Italique

Mis en forme : Police :Italique

Mis en forme : Police :Italique

Mis en forme : Police :Italique

Mis en forme : Police :Italique

Mis en forme : Police :Italique

Mis en forme : Police :Italique

The robustness of the comparison can be increased by further constraining the dataset to POLDER-3 and AERONET *AOD* values larger than 0.10 and limiting the comparison to AERONET data for which AOD_C is at least 30% of the total *AOD*. By applying these thresholds (**Figure 9a**), the correlation between f_{CNS} and f_{NS} is R = 0.56 (N = 274 for the 17 stations). Overall, 80% of the POLDER-3 f_{CNS} agrees within 25% with the AERONET values. The largest differences occur when AERONET retrieves f_{NS} values lower than 50%. In this case, only 40% of the POLDER-3 f_{CNS} are in the ±25% agreement interval with AERONET. Conversely, for AERONET f_{NS} >50%, 88% of the POLDER-3 f_{CNS} agree within ±25% with the AERONET estimate of f_{NS}. Finally, **Figure 10** shows that a relatively good agreement is obtained by comparing broad classes 25% wide, providing consistency confidence to the classification of non-sphericity by POLDER-3.

Finally, Figure 10 shows the implication on those results on the evaluation of the POLDER-3 AOD_{CNS} and AERONET AOD_{NS}. With the previous thresholds (POLDER 3 and AERONET AOD values larger than 0.10 and AERONET AOD_C/AOD larger than 30%), the correlation obtained between coincident POLDER-3 AOD_{CNS} and AERONET AOD_{NS} at 865 nm is significant (R = 0.87).

The two datasets are very consistent. However, the POLDER-3 AOD_{CNS} is almost systematically lower than the AERONET AOD_{NS}, regardless of the percent that it represents with respect to the AOD (not shown). The physical reasons behind this evident discrepancy are beyond the scope of this paper and we recommend addressing them in future research.

5. Discussion

5.1. Evaluation of uncertainties on the advanced POLDER-3 oceanic aerosol products

In this paper we provide a first comprehensive evaluation of the advanced POLDER-3 aerosol products over ocean by the latest operational algorithm, based on ground-based remote sensing (AERONET) but also airborne remote sensing and in situ observations (TRAQA and ADRIMED campaigns) over the western Mediterranean sea. **Table 4** summarizes it by presenting the absolute errors (Δ) derived from the RMS (representing the precision) and the bias (B) as a measure of accuracy. For consistency with previous similar analyses and as an acknowledgment of the large size

Mis en forme : Police :Italique
Mis en forme : Police :Italique
Mis en forme : Police :Italique
Mis en forme : Police :Italique
Mis en forme : Police :Italique
Mis en forme : Police :Italique
Mis en forme : Police :Italique
Mis en forme : Police :Italique
Mis en forme : Police :Italique
Mis en forme : Police :Italique

of the dataset, only the *RMS* and ~~the~~ bias of the linear regressions with the AERONET data have been reported. The uncertainties in AOD_{CS} and AOD_{CNS} were calculated as the square-root of the quadratic sum of the errors in AOD_C and f_{CNS}.

Our estimate of ΔAOD indicates that, for the western Mediterranean basin, the accuracy and the precision of the POLDER-3 are better than those derived by the error analysis of Tanré et al. (2011), also reported in Table 4, based on a global comparison with AERONET of the POLDER-1 instrument. It is noteworthy that the POLDER-1 retrieval algorithm was using a single mode spherical particle size distribution (Goloub et al., 1999) instead of the current two modes allowing, in addition, an aspherical component. Furthermore, from our regional evaluation of the whole latest collection 3 of the POLDER-3 data set, G_{frac} value for *AOD* (73%) is much better than that reported by Bréon et al. (2011) (G_{frac}= 45%), based on previous collection of POLDER-3 retrievals at a global scale.

5.2. Evaluation of the fine and coarse aerosol optical depth~~AOD~~

Table 4 reports the uncertainties in AOD_F and AOD_C based on estimates *RMS* and bias. It is interesting to notice that the precision in AOD_C is apparently lower than in AOD_F (higher *RMS*), despite the correlation being far better for the former than for the latter. We have shown that the direct comparison between POLDER-3 and AERONET should take into account the differences in the definition of the fine size fraction in the respective retrieval algorithms. The AERONET AOD_F is recalculated from the fine mode of the volume size distribution retrieved from the measured total radiance, and defined as the mode below an upper limit diameter ($D_{cut\text{-}off}$) varying between 0.88 and 1.98 µm. Conversely, our comparison with airborne measurements indicates that ~~the~~ AOD_F retrieved by POLDER-3 corresponds to a fine mode extending to values of $D_{cut\text{-}off}$ between 0.6 and 0.8 µm. This is expected as POLDER-3 uses polarised radiances, highly sensitive to fine particles, in agreement with previous regional validations of POLDER AOD_F over land (Kacenelenbogen et al., 2006; Fan et al., 2008; Wang et al., 2015). ~~The~~ Our comparison with in situ data shows that the POLDER-3 AOD_C is less sensitive to the $D_{cut\text{-}off}$ value (**Figure ~~7~~6**), but mostly to the extent of the coarse mode towards the largest particles.

Mis en forme : Police :Italique
Mis en forme : Police :Italique
Mis en forme : Police :Italique
Mis en forme : Police :Italique
Mis en forme : Police :Italique
Mis en forme : Police :Italique
Mis en forme : Police :Italique
Mis en forme : Police :Italique
Mis en forme : Police :Italique
Mis en forme : Police :Italique
Mis en forme : Police :Italique
Mis en forme : Police :Italique
Mis en forme : Police :Italique
Mis en forme : Police :Italique
Mis en forme : Police :Italique
Mis en forme : Police :Italique
Mis en forme : Police :Italique
Mis en forme : Police :Italique

It should also be noted that the values of AOD_F might be biased low at 865 nm, which will result in a lower ~~*RMS* and correlation as compared to the coarse mode (see Figures 4 and 5). This might~~could ~~also act in~~ minimis~~e~~ing the effects of the lack of aerosol absorption in the POLDER algorithm, which could affect the retrieval of pollution and dust aerosols at lower wavelengths where absorption is more significant.

5.3. Regional aerosol distribution

The ability of POLDER-3 in representing the spatial distribution of aerosols in the Mediterranean region is demonstrated in Figure ~~12~~ 11 showing the retrieved products averaged over the operating period. These regional maps highlights a north-south gradient for AOD and AOD_{CNS}, with, on average, the highest values in the southernmost part of the western Mediterranean region, especially over south Ionian Sea off Libya, as previously reported by former satellites AOD products (e.g., Moulin et al., 1998; Antoine and Nobileau, 2006). The distribution of POLDER-3 AE indicates high values along the European coasts (especially over the Adriatic Sea), and low along the North African coasts indicative of the dominance of desert dust in the South and anthropogenic aerosol in the North of the basin. AOD_F and AOD_{CS} maps show moderate spatial variability over the basin, associated to averaged values (AOD_F of 0.033, AOD_{CS} of 0.021) 2 to 3 times lower than those retrieved by POLDER-3 for AOD_{CNS} (0.065). Despite these low spatial patterns, it is noticeable that AOD_F values tend to increase in the Eastern part of our region of study, suggesting the complexity of various aerosol types influences over the Mediterranean Sea.

The detailed investigation of the aerosol climatology and regional distribution of the ~~POLDER-3 derived~~ aerosol optical depth ~~load~~ of the fine and coarse mode aerosol, including spherical and non-spherical components, retrieved by POLDER-3 over the western Mediterranean Sea, ~~as a support to the ongoing research in the area,~~ will be presented in ~~a companion~~ the second part of this paper. This analysis, including the investigation of temporal trends over the 8-year operating period, will provide an important support to the ongoing aerosol research in the ~~area~~region.

6. Conclusing~~ve~~ remarks

Mis en forme : Police :Italique
Mis en forme : Police :Italique, Indice
Mis en forme : Police :Italique
Mis en forme : Police :Italique
Mis en forme : Police :Italique
Mis en forme : Police :Italique
Mis en forme : Police :Italique
Mis en forme : Police :Italique
Mis en forme : Police :Italique
Mis en forme : Police :Italique
Mis en forme : Police :Italique
Mis en forme : Police :Italique

The western Mediterranean aerosol is a complex mixture with a significant temporal and spatial variability at small scales (Pace et al., 2005; 2006; Di Iorio et al., 2009; Mallet et al., 2016 and references therein), and significant impact on present and future regional climate (Nabat et al., 2014; 2015a; 2015b; 2016). High-resolved long-time series of spaceborne observations of aerosol optical depth on different size classes and for differing particle shapes, such as provided by POLDER-3, are essential in exploring those evolutions, directly, but also indirectly, as a term of comparison for climate and transport models (Nabat et al., 2014). In the past, quantitative remote sensing of the ~~AOD~~ aerosol optical depth has proven most useful in establishing decadal climatology of the transport of mineral dust over the basin, highlighting its seasonal variability, geographic distribution and sources, link to large-scale atmospheric dynamics (Dulac et al., 1992; Moulin et al., 1997a; 1997b; 1998; Antoine and Nobileau, 2006; Papadimas et al., 2008).

The quality of the observations is surely key to those surveys, and has motivated the comparative analysis of the advanced POLDER-3 oceanic aerosol products during the whole period of operation (March 2005 to October 2013) presented in this paper, with regards to co-located and coincident ground-based measurements by AERONET, and airborne vertical profiles of aerosol optical depth and size distribution during the TRAQA and ADRIMED campaigns of the ChArMEx project.

The results presented in this paper indicate that overall the operational oceanic algorithm of POLDER-3 provides with a very good evaluation of the various components of the aerosol optical depth at the regional scale of the Western Mediterranean. Our results ~~The results presented in this paper~~ confirm previous validations (Goloub et al., 1999; Kacenelenbogen et al., 2006; Fan et al., 2008; Bréon et al., 2011; Tanré et al., 2011), and provide a first evaluation of the uncertainties on the fine and coarse fractions of the aerosol optical depth, and the partitioning of the coarse mode *AOD* into its spherical and non-spherical components. We highlighted some differences with respect to AERONET and the in situ data, for example in the evaluation of the Angstrom exponent and the non-spherical coarse fraction of the AOD. The physical reasons behind those differences remain unresolved. They might require re-examining the basic assumptions of the LUT or the observational constraints, which is beyond the scope of this paper, but which we recommend addressing in future research.

Mis en forme : Police :Italique

Our results ~~They~~ allow moving forward in the classification of the Mediterranean aerosols, and in particular in the investigation of the anthropogenic fraction, which is relevant to climate change. As a matter of fact, our results indicate that the fine-fraction *AOD* at 865 nm ~~can be constrained~~is contributed by ~~to~~ the aerosol accumulation mode below 0.6-0.8 µm in diameter. On the basis of this result, we recommend that any further comparison to AERONET would be restricted to values corresponding to $D_{cut\text{-}off} < 0.8$ µm. This suggests that ~~the~~ AOD_F measured by POLDER-3 could be used for predicting the submicron column concentrations for air quality studies, and for evaluating the radiative effect of fine aerosols.

Mis en forme : Police :Italique

Mis en forme : Police :Italique

Mis en forme : Police :Italique, Indice

Mis en forme : Police :Italique

Data availability

Commenté [d2]: Nothing about airborne measurements?

POLDER-3 data extraction was performed with the program PARASOLASCII (http://www-loa.univ-lille1.fr/~ducos/public/parasolascii/). This version is made available from the AERIS Data and Service Center (http://www.icare.univ-lille1.fr/parasol). The AERONET version 2.0 aerosol products at the level 2.0 quality (cloud screened and quality assured with up-to-date calibration) were obtained from the official website at http://aeronet.gsfc.nasa.gov/. Single particle Mie scattering calculations were performed with the Mie_single.pro routine under IDL available at http://eodg.atm.ox.ac.uk/MIE/mie_single.html.

Competing interests

The authors declare that they have no conflict of interest.

Special issue statement

This article is part of the special issue of the "C~~H~~hemistry and Ae~~R~~osols Mediterranean Experiment~~s~~ (ChArMEx) (ACP/AMT inter-journal SI)". It is not associated with a conference.

Acknowledgements

This work is part of the ChArMEx project supported by CNRS-INSU, ADEME, Météo-France and CEA in the framework of the multidisciplinary program MISTRALS (Mediterranean Integrated Studies aT Regional And Local Scales; http://mistrals-home.org/). It has also been supported by the French National Research Agency (ANR) through the ADRIMED program (contract ANR-11-BS56-0006) and

by the French National Program of Spatial Teledetection (PNTS, http://www.insu.cnrs.fr/pnts, project n°PNTS-2015-03). L. Mbemba Kabuiku was granted by the French Environment and Energy Management Agency (ADEME) and National Center of Space Studies (CNES). Airborne data was obtained using the ATR-42 atmospheric research aircraft managed by ~~Safire~~SAFIRE, which is a joint facility of the French national center for scientific research (CNRS), Météo-France and CNES. The AERIS national data infrastructure provided access to the POLDER-3 data used in this study. Teams from AERONET and its French component PHOTONS are acknowledged for calibrating the sun-photometer network and producing long-term time series of quality assured aerosol product time series used in this study. We thank the AERONET principal investigators L. A. Arboledas (Alboràn), S. Basart and J. M. Baldasano (Barcelona), B. N. Holben (Blida), J. A. Martinez Lozano (Burjassot), M. Mallet (Ersa and Montesoro Bastia), P. Goloub (Ersa), J. Piazzola (Frioul and Porquerolles), R. Ellul (Gozo), D. Meloni (Lampedusa), F. J. Olmo Reyes (Malaga), S. Pignatti (Messina), J. R. Moreta Gonzalez (Palma de Mallorca), G. P. Gobbi (Rome), Z. Ameur (Tizi Ouzou), S. Despiau (Toulon) and D. Antoine (Villefranche-sur-Mer) and their staff for establishing and maintaining the 17 sites used in this investigation. C. Di Biagio (LISA) and C. Denjean (CNRM) are acknowledged for help with data analysis. G. Siour (LISA) is acknowledged for help with figure production.

References

Ackermann, J.: The extinction-to-backscatter ratio of tropospheric aerosol: A numerical study, J. Atmos. Oceanic Technol., 15, 1043–1050, doi:10.1175/1520-0426, 1998.

Akimoto, H.: Global air quality and pollution, Science, 302, 1716–1719,doi:10.1126/science.1092666, 2003.

Anderson, T. L., Covert, D. S., Marshall, S. F., Laucks, M. L., Charlson, R. J., Waggoner, A. P., Ogren, J. a., Caldow, R., Holm, R. L., Quant, F. R., Sem, G. J., Wiedensohler, A., Ahlquist, N. A., and Bates, T. S.: Performance characteristics of a high-sensitivity, three-wavelength, total scatter/backscatter nephelometer, J. Atmos. Ocean. Technol., 13, 967–986, doi:10.1175/1520-0426(1996)013<0967:PCOAHS>2.0.CO;2, 1996.

Anderson, T. L., and Ogren, J. A.: Determining Aerosol Radiative Properties Using the TSI 3563 Integrating Nephelometer, Aerosol Sci. Technol., 29, 57–69, doi:10.1080/02786829808965551, 1998.

Antoine, D., and Nobileau, D.: Recent increase of Saharan dust transport over the Mediterranean Sea, as revealed from ocean color satellite (SeaWiFS) observations, J. Geophys. Res. Atmos., 111, 1–19, doi:10.1029/2005JD006795, 2006.

Barnaba, F. and Gobbi, G. P.: Aerosol seasonal variability over the Mediterranean region and relative impact of maritime, continental and Saharan dust particles over the basin from MODIS data in the year 2001, Atmos. Chem. Phys., 4, 2367-2391, https://doi.org/10.5194/acp-4-2367-2004, 2004.

Becagli, S., F. Anello, C. Bommarito, F. Cassola, G. Calzolai, T. Di Iorio, A. di Sarra, J.L. Gómez-Amo, F. Lucarelli, M. Marconi, D. Meloni, F. Monteleone, S. Nava, G. Pace, M. Severi, D. M. Sferlazzo, R. Traversi, and Udisti R.: Constraining the ship contribution to the aerosol of the central Mediterranean, Atmos. Chem. Phys., 17, 2067-2084, doi: 10.5194/acp-17-2067-2017, 2017.

Bergametti, G., Dutot, A.-L., Buat-Ménard, P., Losno, R., and Remoudaki, E.: Seasonal variability of the elemental composition of atmospheric aerosol particles over the northwestern Mediterranean, Tellus, 41B, 353-361, doi:10.1111/j.1600-0889.1989.tb00314.x, 1989.

Bohren, C. F., and Huffman, D. R.: Absorption and scattering of light by small particles, Wiley-VCH, 1998.

Boucher, O.: Atmospheric aerosols Properties and Climate Impacts, 311 pp., Springer, 2015.

Boucher, O., Randall, D., Artaxo, P., Bretherton, C., Feingold, G., Forster, P., Kerminen, V.-M., Kondo, Y., Liao, H., Lohmann, U., Rasch, P., Satheesh, S. K., Sherwood, S., Stevens, B., and Zhang, X. Y.: Clouds and Aerosols, in Climate Change 2013 - The Physical Science Basis, edited by Intergovernmental Panel on Climate Change, pp. 571–658, Cambridge University Press, Cambridge., 2013.

Bréon, F.-M., and Colzy, S.: Cloud detection from the spaceborne POLDER instrument and validation against surface synoptic observations, J. Appl. Meteorol., 38, 777–785, doi:10.1175/1520-0450(1999)038<0777:CDFTSP>2.0.CO;2, 1999.

Bréon, F. M., Vermeulen, A., and Descloitres, J.: An evaluation of satellite aerosol products against sunphotometer measurements, Remote Sens. Environ., 115, 3102–3111, doi:10.1016/j.rse.2011.06.017, 2011.

Cai, Y., Montague, D. C., Mooiweer-Bryan, W., and Deshler, T.: Performance characteristics of the ultra high sensitivity aerosol spectrometer for particles between 55 and 800 nm: Laboratory and field studies, J. Aerosol Sci., 39, 759–769, doi:10.1016/j.jaerosci.2008.04.007, 2008.

Chin, M., Ginoux, P., Kinne, S., Torres, O., Holben, B. N., Duncan, D. N., Martin, R. V., Logan, J. A., Higurashi, H., and Nakajima, T.: Tropospheric aerosol optical thickness from the GOCART model and comparisons with satellite and Sun photometer measurements, J. Atmos. Sci., 59, 451-483, doi:10.1175/1520-0469(2002)059<0461:TAOTFT>2.0.CO;2, 2002.

Chou, C., Formenti, P., Maille, M., Ausset, P., Helas, G., Harrison, M, and Osborne, S.: Size distribution, shape, and composition of mineral dust aerosols collected during the African Monsoon Multidisciplinary Analysis Special Observation Period 0: Dust and Biomass-Burning Experiment field campaign in Niger, January 2006, J. Geophys. Res. Atmos., 113, 1–17, doi:10.1029/2008JD009897, 2008.

768 Christensen, J. H., Kumar, K. K., Aldria, E., An, S.-I., Cavalcanti, I. F. a., Castro, M. De, Dong, W.,
769 Goswami, P., Hall, A., Kanyanga, J. K., Kitoh, A., Kossin, J., Lau, N.-C., Renwick, J., Stephenson,
770 D. B., Xie, S.-P. and Zhou, T.: Climate Phenomena and their Relevance for Future Regional
771 Climate Change, in Climate Change 2013 - The Physical Science Basis, edited by
772 Intergovernmental Panel on Climate Change, pp. 1217–1308, Cambridge University Press,
773 Cambridge., 2013.
774 Cros, B., Durand, P., Cachier, H., Drobinski, P., Fréjafon, E., Kottmeier, C., Perros, P. E., Peuch, V.
775 H., Ponche, J. L., Robin, D., Saïd, F., Toupance, G., and Wortham, H.: The ESCOMPTE program:
776 An overview, Atmos. Res., 69, 241–279, doi:10.1016/j.atmosres.2003.05.001, 2004.
777 Denjean C., Cassola F., Mazzino A., Triquet S., Chevaillier S., Grand N., Bourrianne T., Momboisse
778 G., Sellegri K., Schwarzenbock A., Freney E., Mallet M., and Formenti P., Size distribution and
779 optical properties of mineral dust aerosols transported in the western Mediterranean, Atmos.
780 Chem. Phys., 16, 1081–1104, doi:10.5194/acp-16-1081-2016, 2016.
781 Deuzé, J. L., Herman, M., Goloub, P., Tanré, D., and Marchand, A.: Characterization of aerosols over
782 ocean from POLDER/ADEOS-1, Geophys. Res. Lett., 26, 1421, doi:10.1029/1999GL900168,
783 1999.
784 Deuzé, J. L., Goloub, P., Herman, M., Marchand, A., Perry, G., Susana, S., and Tanré, D.: Estimate
785 of the aerosol properties over the ocean with POLDER, J. Geophys. Res. Atmos., 105, 15329–
786 15346, doi:10.1029/2000JD900148, 2000.
787 Di Biagio, C., Doppler, L., Gaimoz, C., Grand, N., Ancellet, G., Raut, J.-C., Beekmann, M., Borbon,
788 A., Sartelet, K., Attié, J.-L., Ravetta, F., and Formenti, P.: Continental pollution in the western
789 Mediterranean basin: vertical profiles of aerosol and trace gases measured over the sea during
790 TRAQA 2012 and SAFMED 2013, Atmos. Chem. Phys., 15, 9611–9630, doi:10.5194/acp-15-
791 9611-2015, 2015.
792 Di Biagio C., Formenti P., Doppler L., Gaimoz C., Grand N., Ancellet G., Attié J.L., Bucci S., Dubuisson
793 P., Fierli F., Mallet M., and Ravetta F., Continental pollution in the Western Mediterranean basin:
794 large variability of the aerosol single scattering albedo and influence onthe direct shortwave
795 radiative effect, Atmos. Chem. Phys., 16, 10591–10607, doi:10.5194/acp-16-10591-2016, 2016.
796 Di Iorio, T., di Sarra, A., Sferlazzo, D. M., Cacciani, M., Meloni, D., Monteleone, F., Fuà, D., and
797 Fiocco, G.: Seasonal evolution of the tropospheric aerosol vertical profile in the central
798 Mediterranean and role of desert dust, J. Geophys. Res., 114, D02201,
799 doi:10.1029/2008jd010593, 2009.
800 Di Sarra, A., Pace, G., Meloni, D., De Silvestri, L., Piacentino, S., and Monteleone, F.: Surface
801 shortwave radiative forcing of different aerosol types in the central Mediterranean, Geophys. Res.
802 Lett., 35, L02714, doi:10.1029/2007GL032395, 2008.
803 Dubovik, O., and King, M. D.: A flexible inversion algorithm for retrieval of aerosol optical properties
804 from Sun and sky radiance measurements, J. Geophys. Res. Atmos., 105, 20673–20696,
805 doi:10.1029/2000JD900282, 2000.
806 Dubovik, O., Holben, B., Eck, T. F., Smirnov, A., Kaufman, Y. J., King, M. D., Tanré, D., and Slutsker,
807 I.: Variability of Absorption and Optical Properties of Key Aerosol Types Observed in Worldwide
808 Locations, J. Atmos. Sci., 59, 590–608, doi:10.1175/1520-0469(2002);2, 2002.
809 Dubovik, O., Sinyuk, A., Lapyonok, T., Holben, B. N., Mishchenko, M., Yang, P., Eck, T. F., Volten,
810 H., Muñoz, O., Veihelmann, B., van der Zande, W. J., Leon, J.-F., Sorokin, M., and Slutsker, I.:
811 Application of spheroid models to account for aerosol particle nonsphericity in remote sensing of
812 desert dust, J. Geophys. Res., 111, D11208, doi:10.1029/2005JD006619, 2006.
813 Dulac, F., and Chazette, P.: Airborne study of a multi-layer aerosol structure in the eastern
814 Mediterranean observed with the airborne polarized lidar ALEX during a STAAARTE campaign
815 (7 June 1997), Atmos. Chem. Phys., 3, 1817–1831, doi:10.5194/acp-3-1817-2003, 2003.
816 Dulac, F., Tanré, D., Bergametti, G., Buat-Ménard, P., Desbois, M., and Sutton, D.: Assessment of
817 the African airborne dust mass over the western Mediterranean Sea using Meteosat data, J.
818 Geophys. Res., 97, 2489, doi:10.1029/91JD02427, 1992.
819 Fan, X., Goloub, P., Deuzé, J. L., Chen, H., Zhang, W., Tanré, D., and Li, Z.: Evaluation of PARASOL
820 aerosol retrieval over North East Asia, Remote Sens. Environ., 112, 697–707,
821 doi:10.1016/j.rse.2007.06.010, 2008.

Formenti, P., Boucher, O., Reiner, T., Sprung, D., Andreae, M. O., Wendisch, M., Wex, H., Kindred, D., Tzortziou, M., Vasaras, A., and Zerefos, C.: STAAARTE-MED 1998 summer airborne measurements over the Aegean Sea 2. Aerosol scattering and absorption, and radiative calculations, J. Geophys. Res. Atmos., 107, doi:10.1029/2001JD001536, 2002.

Formenti, P., Rajot, J. L., Desboeufs, K., Saïd, F., Grand, N., Chevaillier, S., and Schmechtig, C.: Airborne observations of mineral dust over western Africa in the summer Monsoon season: spatial and vertical variability of physico-chemical and optical properties, Atmos. Chem. Phys., 11, 6387-6410, doi:10.5194/acp-11-6387-2011, 2011.

García-Ruiz, J. M., López-Moreno, J. I., Vicente-Serrano, S. M., Lasanta–Martínez, T., and Beguería, S.: Mediterranean water resources in a global change scenario, Earth-Science Rev., 105, 121–139, doi:10.1016/j.earscirev.2011.01.006, 2011.

Giorgi, F.: Climate change hot-spots, Geophys. Res. Lett., 33, L08707, doi:10.1029/2006GL025734, 2006.

Giorgi, F., and Lionello, P.: Climate change projections for the Mediterranean region, Glob. Planet. Change, 63, 90–104, doi:10.1016/j.gloplacha.2007.09.005, 2008.

Gkikas, A., Hatzianastassiou, N., and Mihalopoulos, N.: Aerosol events in the broader Mediterranean basin based on 7-year (2000-2007) MODIS C005 data, Ann. Geophys., 27, 3509-3522, doi:10.5194/angeo-27-3509-2009, 2009.

Gkikas, A., Basart, S., Hatzianastassiou, N., Marinou, E., Amiridis, V., Kazadzis, S., Pey, J., Querol, X., Jorba, O., Gassó, S., and Baldasano, J. M.: Mediterranean intense desert dust outbreaks and their vertical structure based on remote sensing data, Atmos. Chem. Phys., 16, 8609-8642, doi:10.5194/acp-16-8609-2016, 2016.

Goloub, P., Tanré, D., Deuzé, J. L., Herman, M., Marchand, A., and Bréon, F.-M.: Validation of the first algorithm applied for deriving the aerosol properties over the ocean using the POLDER/ADEOS measurements, IEEE Trans. Geosci. Remote Sens., 37, 1586–1596, doi:10.1109/36.763270, 1999.

Granados-Muñoz, M. J., Navas-Guzmán, F., Luis Guerrero-Rascado, J., Antonio Bravo-Aranda, J., Binietoglou, I., Nepomuceno Pereira, S., Basart, S., Baldasano, J. M., Belegante, L., Chaikovsky, A., Comerón, A., D'Amico, G., Dubovik, O., Ilic, L., Kokkalis, P., Muñoz-Porcar, C., Nickovic, S., Nicolae, D., José Olmo, F., Papayannis, A., Pappalardo, G., Rodríguez, A., Schepanski, K., Sicard, M., Vukovic, A., Wandinger, U., Dulac, F., and Alados-Arboledas, L.: Profiling of aerosol microphysical properties at several EARLINET/AERONET sites during the July 2012 ChArMEx/EMEP campaign, Atmos. Chem. Phys., 16, 7043–7066, doi:10.5194/acp-16-7043-2016, 2016.

Grimm, H., and Eatough, D. J.: Aerosol measurement: the use of optical light scattering for the determination of particulate size distribution, and particulate mass, including the semi-volatile fraction., J. Air Waste Manag. Assoc., 59, 101–107, doi:10.3155/1047-3289.59.1.101, 2009.

Herman, M., Deuzé, J. L., Marchand, A., Roger, B., and Lallart, P.: Aerosol remote sensing from POLDER/ADEOS over the ocean: Improved retrieval using a nonspherical particle model, J. Geophys. Res., 110, D10S02, doi:10.1029/2004JD004798, 2005.

Holben, B. N., Eck, T. F., Slutsker, I., Tanré, D., Buis, J. P., Setzer, A., Vermote, E., Reagan, J. A., Kaufman, Y. J., Nakajima, T., Lavenu, F., Jankowiak, I., and Smirnov, A.: AERONET - A federated instrument network and data archive for aerosol characterization, Remote Sens. Environ., 66, 1–16, doi:10.1016/S0034-4257(98)00031-5, 1998.

Holben, B. N., Tanré, D., Smirnov, A., Eck, T. F., Slutsker, I., Abuhassan, N., Newcomb, W. W., Schafer, J. S., Chatenet, B., Lavenu, F., Kaufman, Y. J., Castle, J. Vande, Setzer, A., Markham, B., Clark, D., Frouin, R., Halthore, R., Karneli, A., O'Neill, N. T., Pietras, C., Pinker, R. T., Voss, K., and Zibordi, G.: An emerging ground-based aerosol climatology: Aerosol optical depth from AERONET, J. Geophys. Res. Atmos., 106, 12067–12097, doi:10.1029/2001JD900014, 2001.

Huneeus, N., Schulz, M., Balkanski, Y., Griesfeller, J., Prospero, J., Kinne, S., Bauer, S., Boucher, O., Chin, M., Dentener, F., Diehl, T., Easter, R., Fillmore, D., Ghan, S., Ginoux, P., Grini, A., Horowitz, L., Koch, D., Krol, M. C., Landing, W., Liu, X., Mahowald, N., Miller, R., Morcrette, J.-J., Myhre, G., Penner, J., Perlwitz, J., Stier, P., Takemura, T., and Zender, C. S.:: Global dust model intercomparison in AeroCom phase I, Atmos. Chem. Phys., 11, 7781-7816. doi:10.5194/acp-11-7781-2011., 2011.

877 Kacenelenbogen, M., Léon, J.-F., Chiapello, I., and Tanré, D.: Characterization of aerosol pollution
878 events in France using ground-based and POLDER-2 satellite data, Atmos. Chem. Phys., 6,
879 4851-4866 , 2006.
880 Kalivitis, N., Bougiatioti, A., Kouvarakis, G., and Mihalopoulos, N.: Long term measurements of
881 atmospheric aerosol optical properties in the Eastern Mediterranean, Atmos. Res., 102, 351–
882 357, doi:10.1016/j.atmosres.2011.08.013, 2011.
883 Karol, Y., Tanré, D., Goloub, P., Vervaerde, C., Balois, J. Y., Blarel, L., Podvin, T., Mortier, A., and
884 Chaikovsky, A.: Airborne sun photometer PLASMA: concept, measurements, comparison of
885 aerosol extinction vertical profile with lidar, Atmos. Meas. Tech., 6, 2383–2389, doi:10.5194/amt-
886 6-2383-2013, 2013.
887 Kebabian, P. L., Robinson, W. A., and Freedman, A.: Optical extinction monitor using cw cavity
888 enhanced detection, Rev. Sci. Instrum., 78, doi:10.1063/1.2744223, 2007.
889 Kim, D., Chin, M., Yu, H., Diehl, T., Tan, Q., Kahn, R. A., Tsigaridis, K., Bauer, S. E., Takemura, T.,
890 Pozzoli, L., Bellouin, N., Schulz, M., Peyridieu, S., Chédin, A., and Koffi, B.: Sources, sinks, and
891 transatlantic transport of North African dust aerosol: A multimodel analysis and comparison with
892 remote sensing data, J. Geophys. Res. Atmos., 119, 6259–6277, doi:10.1002/2013JD021099,
893 2014.
894 Kovats, R. S., Valentini, R., Bouwer, L. M., Georgopoulou, E., Jacob, D., Martin, E., Rounsevell, M.,
895 and Soussana, J.-F.: Europe, in Climate Change 2014: Impacts, Adaptation, and Vulnerability.
896 Part B: Regional Aspects, Contribution of Working Group II to Fifth Assessment Report of the
897 Intergovernmental Panel on Climate Change, Eds. Barros, V.R., Field, C.B., Dokken, D.J.,
898 Mastrandrea, M.D., Mach, K.J., Bilir, T.E., Chatterjee, M., Ebi, K.L., Estrada, Y.O., Genova, R.C.,
899 Girma, B., Kissel, E.S., Levy, A.N., MacCracken, S., Mastrandrea, P.R., and White, L.L.,
900 Cambridge University Press, 1267–1326, 2014.
901 Kubilay, N., Cokacar, T., and Oguz, T.: Optical properties of mineral dust outbreaks over the
902 northeastern Mediterranean, J. Geophys. Res. Atmos., 108, 1–10, doi:10.1029/2003JD003798,
903 2003.
904 Lelieveld, J., Berresheim, H., Borrmann, S., Crutzen, P. J., Dentener, F. J., Fischer, H., Feichter, J.,
905 Flatau, P. J., Heland, J., Holzinger, R., Korrmann, R., Lawrence, M. G., Levin, Z., Markowicz, K.
906 M., Mihalopoulos, N., Minikin, a, Ramanathan, V., De Reus, M., Roelofs, G. J., Scheeren, H. a,
907 Sciare, J., Schlager, H., Schultz, M., Siegmund, P., Steil, B., Stephanou, E. G., Stier, P., Traub,
908 M., Warneke, C., Williams, J., and Ziereis, H.: Global air pollution crossroads over the
909 Mediterranean, Science, 298, 794–9, doi:10.1126/science.1075457, 2002.
910 Liu, P. S. K., Leaitch, W. R., Strapp, J. W., and Wasey, M. A.: Response of Particle Measuring
911 Systems Airborne ASASP and PCASP to NaCl and Latex Particles, Aerosol Sci. Technol., 16,
912 83–95, doi:10.1080/02786829208959539, 1992.
913 Lyamani, H., Valenzuela, A., Perez-Ramirez, D., Toledano, C., Granados-Muñoz, M. J., Olmo, F. J.,
914 and Alados-Arboledas, L.: Aerosol properties over the western Mediterranean basin: temporal
915 and spatial variability, Atmos. Chem. Phys., 15, 2473–2486, doi:10.5194/acp-15-2473-2015,
916 2015.
917 Mallet, M., Dubovik, O., Nabat, P., Dulac, F., Kahn, R., Sciare, J., Paronis, D. and Léon, J. F.:
918 Absorption properties of Mediterranean aerosols obtained from multi-year ground-based remote
919 sensing observations, Atmos. Chem. Phys., 13, 9195–9210, doi:10.5194/acp-13-9195-2013,
920 2013.
921 Mallet, M., Dulac, F., Formenti, P., Nabat, P., Sciare, J., Roberts, G., Pelon, J., Ancellet, G., Tanré,
922 D., Parol, F., Denjean, C., Brogniez, G., di Sarra, A., Alados-Arboledas, L., Arndt, J., Auriol, F.,
923 Blarel, L., Bourrianne, T., Chazette, P., Chevaillier, S., Claeys, M., D'Anna, B., Derimian,
924 Y., Desboeufs, K., Di Iorio, T., Doussin, J.-F., Durand, P., Féron, A., Freney, E., Gaimoz, C.,
925 Goloub, P., Gómez-Amo, J. L., Granados-Muñoz, M. J., Grand, N., Hamonou, E., Jankowiak, I.,
926 Jeannot, M., Léon, J.-F., Maillé, M., Mailler, S., Meloni, D., Menut, L., Momboisse, G., Nicolas,
927 J., Podvin, T., Pont, V., Rea, G., Renard, J.-B., Roblou, L., Schepanski, K., Schwarzenboeck, A.,
928 Sellegri, K., Sicard, M., Solmon, F., Somot, S., Torres, B., Totems, J., Triquet, S., Verdier, N.,
929 Verwaerde, C., Waquet, F., Wenger, J., and Zapf, P.: Overview of the Chemistry-Aerosol
930 Mediterranean Experiment/Aerosol Direct Radiative Forcing on the Mediterranean Climate

(ChArMEx/ADRIMED) summer 2013 campaign, Atmos. Chem. Phys., 16, 455–504, doi:10.5194/acp-16-455-2016, 2016.
Markwardt, C. B.: Non-linear least squares fitting in IDL with MPFIT, in Proc. Astronomical Data Analysis Software and Systems XVIII, eds. D. Bohlender, P. Dowler & D. Durand, Astron. Soc. Pac. Conf. Ser., 411, 251, 2009.
Massoli, P., Kebabian, P. L., Onasch, T. B., Hills, F. B. and Freedman, A.: Aerosol light extinction measurements by Cavity Attenuated Phase Shift (CAPS) spectroscopy: Laboratory validation and field deployment of a compact aerosol particle extinction monitor, Aerosol Sci. Technol., 44(6), 428–435, doi:10.1080/02786821003716599, 2010.
Meloni, D., di Sarra, A., Biavati, G., Deuisi, J.J., Montelelone, F., Pace, G., Piacentino, S., and Sferlazzo, D. M. : Seasonal behavior of Saharan dust events at the Mediterranean island of Lampedusa in the period 1999–2005, Atmos. Environ., 41, 3041-3056, doi:10.1016/j.atmosenv.2006.12.001, 2007.
Mie, G.: Beiträge zur Optik trüber Medien, speziell kolloidaler Metallösungen, Ann. Phys., 330, 377–445, doi:10.1002/andp.19083300302, 1908.
Migon, C., Alleman, L., Leblond, N., and Nicolas, E.: Evolution of atmospheric lead over the northwestern Mediterranean between 1986 and 1992, Atmos Environ.A., 27, 2161-2167, doi:10.1016/0960-1686(93)90045-Z, 1993.
Mihalopoulos, N., Stephanou, E., Kanakidou, M., Pilitsidis, S., and Bousquet, P.: Tropospheric aerosol ionic composition in the Eastern Mediterranean region. Tellus B, 49, 314-326. doi:10.1034/j.1600-0889.49.issue3.7.x, 1997.
Mishchenko, M. I., Travis, L. D., Kahn, R. A., and West, R. A.: Modeling phase function for dustlike tropospheric aerosols using a shape mixture of randomly oriented polydisperse spheroids, J. Geophys. Res., 102, 16831–16847, doi:10.1029/96JD02110, 1997.
Monks, P. S., Granier, C., Fuzzi, S., Stohl, A., Williams, M. L., Akimoto, H., Amann, M., Baklanov, A., Baltensperger, U., Bey, I., Blake, N., Blake, R. S., Carslaw, K., Cooper, O. R., Dentener, F., Fowler, D., Fragkou, E., Frost, G. J., Generoso, S., Ginoux, P., Grewe, V., Guenther, A., Hansson, H. C., Henne, S., Hjorth, J., Hofzumahaus, A., Huntrieser, H., Isaksen, I. S. A., Jenkin, M. E., Kaiser, J., Kanakidou, M., Klimont, Z., Kulmala, M., Laj, P., Lawrence, M. G., Lee, J. D., Liousse, C., Maione, M., McFiggans, G., Metzger, A., Mieville, A., Moussiopoulos, N., Orlando, J. J., O'Dowd, C. D., Palmer, P. I., Parrish, D. D., Petzold, A., Platt, U., Pöschl, U., Prévôt, A. S. H., Reeves, C. E., Reimann, S., Rudich, Y., Sellegri, K., Steinbrecher, R., Simpson, D., ten Brink, H., Theloke, J., van der Werf, G. R., Vautard, R., Vestreng, V., Vlachokostas, C., and von Glasow, R.: Atmospheric composition change – global and regional air quality, Atmos. Environ., 43, 5268–5350, doi:10.1016/j.atmosenv.2009.08.021, 2009.
Moulin, C., Guillard, F., Dulac, F., and Lambert, C. E.: Long-term daily monitoring of Saharan dust load over ocean using Meteosat ISCCP-B2 data: 1. Methodology and preliminary results for 1983–1994 in the Mediterranean, J. Geophys. Res., 102, 16947, doi:10.1029/96JD02620, 1997a.
Moulin, C., Lambert, C. E., Dulac, F., and Dayan, U.: Control of atmospheric export of dust from North Africa by the North Atlantic Oscillation, Nature, 387 (6634), 691-694, 1997b.
Moulin, C., Lambert, C. E., Dayan, U., Masson, V., Ramonet, M., Bousquet, P., Legrand, M., Balkanski, Y. J., Guelle, W., Marticorena, B., Bergametti, G., and Dulac, F.: Satellite climatology of African dust transport in the Mediterranean atmosphere, J. Geophys. Res., 103, 13137, doi:10.1029/98JD00171, 1998.
Müller, T., Nowak, A., Wiedensohler, A., Sheridan, P., Laborde, M., Covert, D. S., Marinoni, A., Imre, K., Henzing, B., Roger, J.-C., Martins dos Santos, S., Wilhelm, R., Wang, Y.-Q. and de Leeuw, G.: Angular illumination and truncation of three different integrating nephelometers: Implications for empirical, size-based orrections, Aerosol Sci. Technol., 43, 581–586, doi:10.1080/02786820902798484, 2009.
Myhre, G., Shindell, D., Bréon, F.-M., Collins, W., Fuglestvedt, J., Huang, J., Koch, D., Lamarque, J.-F., Lee, D., Mendoza, B., Nakajima, T., Robock, A., Stephens, G., Takemura, T., and Zhan, H.: Anthropogenic and Natural Radiative Forcing, in Climate Change 2013: The Physical Science Basis, pp. 659–740, 2013.
Nabat, P., Somot, S., Mallet, M., Chiapello, I., Morcrette, J. J., Solmon, F., Szopa, S., Dulac, F., Collins, W., Ghan, S., Horowitz, L. W., Lamarque, J. F., Lee, Y. H., Naik, V., Nagashima, T.,

Shindell, D., and Skeie, R.: A 4-D climatology (1979-2009) of the monthly tropospheric aerosol optical depth distribution over the Mediterranean region from a comparative evaluation and blending of remote sensing and model products, Atmos. Meas. Tech., 6, 1287–1314, doi:10.5194/amt-6-1287-2013, 2013.

Nabat, P., Somot, S. Mallet, M., Sanchez-Lorenzo, A., and Wild, M.: Contribution of anthropogenic sulfate aerosols to the changing Euro-Mediterranean climate since 1980, Geophys. Res. Lett., 41, doi:10.1002/2014GL060798, 2014.

Nabat, P., Somot, S., Mallet, M., Michou, M., Sevault, F., Driouech, F., Meloni, D., di Sarra, A., Di Biagio, C., Formenti, P., Sicard, M., Léon, J.-F., and Bouin, M.-N.: Dust aerosol radiative effects during summer 2012 simulated with a coupled regional aerosol–atmosphere–ocean model over the Mediterranean, Atmos. Chem. Phys., 15, 3303-3326, doi:10.5194/acp-15-3303-2015, 2015a.

Nabat P., S. Somot, M. Mallet, F. Sevault, M. Chiacchio, and M. Wild: Direct and semi-direct aerosol radiative effect on the Mediterranean climate variability using a coupled regional climate system model, Clim. Dyn., 44, 1127-1155, doi:10.1007/s00382-014-2205-6, 2015b.

Nabat, P., Kiki, Somot, S., Mallet, M. and Michou, M.: Impact of aerosols in regional climate projections over the Mediterranean area, in Air Pollution Modeling and its Application XXIV, , Springer, Ed. by Steyn, D. G., and Chaumerliac, N., pp. 73-78, doi:10.1007/978-3-319-24478-5_12, 2016.

Pace, G., Meloni, D., and di Sarra, A.: Forest fire aerosol over the Mediterranean basin during summer 2003, J. Geophys. Res., 110, D21202, doi:10.1029/2005jd005986, 2005.

Pace, G., di Sarra, A., Meloni, D., Piacentino, S., and Chamard, P.: Aerosol optical properties at Lampedusa (Central Mediterranean). 1. Influence of transport and identification of different aerosol types, Atmos. Chem. Phys., 6, 697–713, doi:10.5194/acp-6-697-2006, 2006.

Pan, X., Chin, M., Gautam, R., Bian, H., Kim, D., Colarco, P. R., Diehl, T. L., Takemura, T., Pozzoli, L., Tsigaridis, K., Bauer, S. and Bellouin, N.: A multi-model evaluation of aerosols over South Asia: Common problems and possible causes, Atmos. Chem. Phys., 15(10), 5903–5928, doi:10.5194/acp-15-5903-2015, 2015.

Papadimas, C. D., Hatzianastassiou, N., Mihalopoulos, N., Querol, X., and Vardavas, I.: Spatial and temporal variability in aerosol properties over the Mediterranean basin based on 6-year (2000–2006) MODIS data, J. Geophys. Res., 113, D11205, doi:10.1029/2007JD009189, 2008.

Pappalardo, G., Amodeo, A., Apituley, A., Comeron, A., Freudenthaler, V., Linné, H., Ansmann, A., Bösenberg, J., D'Amico, G., Mattis, I., Mona, L., Wandinger, U., Amiridis, V., Alados-Arboledas, L., Nicolae, D., and Wiegner, M.: EARLINET: Towards an advanced sustainable European aerosol lidar network, Atmos. Meas. Tech., 7, 2389–2409, doi:10.5194/amt-7-2389-2014, 2014.

Pérez, N., Pey, J., Castillo, S., Viana, M., Alastuey, A., and Querol, X.: Interpretation of the variability of levels of regional background aerosols in the Western Mediterranean, Sci. Total Environ., 407, 527-540, doi:10.1016/j.scitotenv.2008.09.006, 2008.

Petzold, A., Rasp, K., Weinzierl, B., Esselborn, M., Hamburger, T., Dörnbrack, A., Kandler, K., Schütz, L., Knippertz, P., Fiebig, M., and Virkkula, A.: Saharan dust absorption and refractive index from aircraft-based observations during SAMUM 2006, Tellus B, 61, 118-130, 10.1111/j.1600-0889.2008.00383.x, 2009.

Petzold, A., Onasch, T., Kebabian, P., and Freedman, A.: Intercomparison of a Cavity Attenuated Phase Shift-based extinction monitor (CAPS PMex) with an integrating nephelometer and a filter-based absorption monitor, Atmos. Meas. Tech., 6, 1141–1151, doi:10.5194/amt-6-1141-2013, 2013.

Pey, J., Querol, X., Alastuey, A., Forastiere, F. and Stafoggia, M.: African dust outbreaks over the Mediterranean Basin during 2001-2011: PM10 concentrations, phenomenology and trends, and its relation with synoptic and mesoscale meteorology, Atmos. Chem. Phys., 13, 1395–1410, doi:10.5194/acp-13-1395-2013, 2013.

Pope III, C. A., Burnett, R. T., Thun, M. J., Calle, E. E., Krewski, D., Ito, K., and Thurston, G. D.: Lung Cancer, Cardiopulmonary Mortality, and Long-term Exposure to Fine Particulate Air Pollution, J. AMA, 287, 1132, doi:10.1001/jama.287.9.1132, 2002.

Pope III, C. A., and Dockery, D. W.: Health Effects of Fine Particulate Air Pollution: Lines that Connect, J. Air Waste Manage. Assoc., 56, 709–742, doi:10.1080/10473289.2006.10464485, 2006.

Putaud, J.-P., Van Dingenen, R., Dell'Acqua, A., Raes, F., Matta, E., Decesari, S., Facchini, M. C.,and Fuzzi, S.: Size-segregated aerosol mass closure and chemical composition in Monte Cimone (I) during MINATROC, Atmos. Chem. Phys., 4, 889–902, doi:10.5194/acp-4-889-2004, 2004.

Querol, X., Alastuey, A, Pey, J., Cusack, M., Pérez, N., Mihalopoulos, N., Theodosi, C., Gerasopoulos, E., Kubilay, N., and Koçak, M.: Variability in regional background aerosols within the Mediterranean, Atmos. Chem. Phys., 9, 4575–4591, doi:10.5194/acp-9-4575-2009, 2009.

Rea G., Turquety S., Menut L., Briant R., Mailler S., and Siour G.: Source contributions to 2012 summertime aerosols in the Euro-Mediterranean region, Atmos. Chem. Phys., 15, 8013–8036, doi:10.5194/acp-15-8013-2015, 2015.

Reid, J. S., Eck, T. F., Christopher, S. a., Hobbs, P. V., and Holben, B.: Use of the Ångstrom exponent to estimate the variability of optical and physical properties of aging smoke particles in Brazil, J. Geophys. Res. Atmos., 104, 27473–27489, doi:10.1029/1999JD900833, 1999.

Reid, J. S., Kinney, J. E., Westphal, D. L., Holben, B. N., Welton, E. J., Tsay, S.-C., Eleuterio, D. P., Campbell, J. R., Christopher, S. A., Colarco, P. R., Jonsson, H. H., Livingston, J. M., Maring, H. B., Meier, M. L., Pilewskie, P., Prospero, J. M., Reid, E. A., Remer, L. A., Russell, P. B., Savoie, D. L., Smirnov, A., and Tanré, D.: Analysis of measurements of Saharan dust by airborne and ground-based remote sensing methods during the Puerto Rico Dust Experiment (PRIDE), J. Geophys. Res., 108, 8586, doi:10.1029/2002JD002493, 2003.

Ryder, C. L., Highwood, E. J., Rosenberg, P. D., Trembath, J., Brooke, J. K., Bart, M., Dean, A., Crosier, J., Dorsey, J., Brindley, H., Banks, J., Marsham, J. H., McQuaid, J. B., Sodemann, H., and Washington, R.: Optical properties of Saharan dust aerosol and contribution from the coarse mode as measured during the Fennec 2011 aircraft campaign, Atmos. Chem. Phys., 13, 303-325, doi:10.5194/acp-13-303-2013, 2013.

Sayer, A. M., Smirnov, A., Hsu, N. C., Munchak, L. A., and Holben, B. N.: Estimating marine aerosol particle volume and number from Maritime Aerosol Network data, Atmos. Chem. Phys., 12, 8889–8909, doi:10.5194/acp-12-8889-2012, 2012a.

Sayer, A. M., Hsu, N. C., Bettenhausen, C., Ahmad, Z., Holben, B. N., Smirnov, A., Thomas, G. E., and Zhang, J.: SeaWiFS Ocean Aerosol Retrieval (SOAR): Algorithm, validation, and comparison with other data sets, J. Geophys. Res. Atmos., 117, 1–17, doi:10.1029/2011JD016599, 2012b.

Shindell, D. T., Lamarque, J. F., Schulz, M., Flanner, M., Jiao, C., Chin, M., Young, P. J., Lee, Y. H., Rotstayn, L., Mahowald, N., Milly, G., Faluvegi, G., Balkanski, Y., Collins, W. J., Conley, A. J., Dalsoren, S., Easter, R., Ghan, S., Horowitz, L., Liu, X., Myhre, G., Nagashima, T., Naik, V., Rumbold, S. T., Skeie, R., Sudo, K., Szopa, S., Takemura, T., Voulgarakis, A., Yoon, J. H., and Lo, F.: Radiative forcing in the ACCMIP historical and future climate simulations, Atmos. Chem. Phys., 13, 2939–2974, doi:10.5194/acp-13-2939-2013, 2013.

Sicard, M., Barragan, R., Muñoz-Porcar, C., Comerón, A., Mallet, M., Dulac, F., Pelon, J., Alados Arboledas, L., Amodeo, A., Boselli, A., Bravo-Aranda, J. A., D'amico, G., Granados Muñoz, M. J., Leto, G., Guerrero Rascado, J. L., Madonna, F., Mona, L., Pappalardo, G., Perrone, M. R., Burlizzi, P., Rocadenbosch, F., Rodríguez-Gómez, A., Scollo, S., Spinelli, N., Titos, G., Wang, X., and Zanmar Sanchez, R.: Contribution of EARLINET/ACTRIS to the summer 2013 Special Observing Period of the ChArMEx project: monitoring of a Saharan dust event over the western and central Mediterranean, Int. J. Remote Sens., 37, 4698–4711, doi:10.1080/01431161.2016.1222102, 2016.

Smirnov, A., Holben, B. N., Eck, T. F., Dubovik, O., and Slutsker, I.: Cloud-screening and quality control algorithms for the AERONET database, Remote Sens. Environ., 73, 337-349, doi:10.1016/S0034-4257(00)00109-7, 2000.

Smirnov, A., Holben, B. N., Giles, D. M., Slutsker, I., O'Neill, N. T., Eck, T. F., Macke, A., Croot, P., Courcoux, Y., Sakerin, S. M., Smyth, T. J., Zielinski, T., Zibordi, G., Goes, J. I., Harvey, M. J., Quinn, P. K., Nelson, N. B., Radionov, V. F., Duarte, C. M., Losno, R., Sciare, J., Voss, K. J., Kinne, S., Nalli, N. R., Joseph, E., Krishna Moorthy, K., Covert, D. S., Gulev, S. K., Milinevsky, G., Larouche, P., Belanger, S., Horne, E., Chin, M., Remer, L. A., Kahn, R. A., Reid, J. S., Schulz, M., Heald, C. L., Zhang, J., Lapina, K., Kleidman, R. G., Griesfeller, J., Gaitley, B. J., Tan, Q., and Diehl, T. L.: Maritime aerosol network as a component of AERONET – first results and comparison with global aerosol models and satellite retrievals, Atmos. Meas. Tech., 4, 583-597, doi:10.5194/amt-4-583-2011, 2011.

Söderman, D., and Dulac, F.: Monitoring and prediction of the atmospheric transport and deposition of desert dust in the Mediterranean region, World Meteorological Organization Publication WMO TD864, Geneva, 177-182, 1998.

Tanré, D., Bréon, F. M., Deuzé, J. L., Dubovik, O., Ducos, F., François, P., Goloub, P., Herman, M., Lifermann, A. and Waquet, F.: Remote sensing of aerosols by using polarized, directional and spectral measurements within the A-Train: the PARASOL mission, Atmos. Meas. Tech., 4, 1383–1395, doi:10.5194/amt-4-1383-2011, 2011.

Torres, B., Dubovik, O., Fuertes, D., Schuster, G., Cachorro, V. E., Lapyonok, T., Goloub, P., Blarel, L., Barreto, A., Mallet, M., Toledano, C., and Tanré, D.: Advanced characterisation of aerosol size properties from measurements of spectral optical depth using the GRASP algorithm, Atmos. Meas. Tech., 10, 3743-3781, https://doi.org/10.5194/amt-10-3743-2017, 2017.

Wang, J., C. Zhu, and Y. Zhu, Estimating the POLDER sensitivity to aerosol size using PARASOL observations, Remote Sens. Lett., 6, 88–96, doi:10.1080/2150704X.2015.1007247, 2015.

Wendisch, M., and J.-L. Brenguier, Airborne Measurements for Environmental Research, Wiley-VCH., 2013.

Zerefos, C. S., Kourtidis, K. A., Melas, D., Balis, D., Zanis, P., Katsaros, L., Mantis, H. T., Repapis, C., Isaksen, I., Sundet, J., Herman, J., Bhartia, P. K., and Calpini, B.: Photochemical Activity and Solar Ultraviolet Radiation (PAUR) modulation factors: An overview of the project, J. Geophys. Res. Atmos., 107, doi:10.1029/2000JD000134, 2002.

Figure captions

Figure 1. Map of the location of the 17 AERONET ground-based stations considered in this work.

Figure 2. Iterative data inversion procedure to retrieve from airborne observations the aerosol optical depth (AOD, AOD_F and AOD_C) and Angstrom exponent (AE) as measured by POLDER-3. Green boxes indicate the input values from airborne measurements (size distribution, scattering and extinction coefficients) and the initial values of the complex refractive indices estimated from published literature. The iterative steps of the procedure are indicated in the blue boxes. The results of optical calculations (corrected size distribution, scattering and extinction coefficients) are in the orange boxes.

Figure 32. Flight tracks of the ATR 42 aircraft (coloured lines) during the TRAQA (left) and ADRIMED (right) campaigns. Only flights relevant to this study are presented. The location of the vertical profiles coincidental, at their lowermost altitude, with a POLDER-3 overpass is shown by a black star.

Figure 4.3. Scatter plots of daily *AOD* retrieved by POLDER-3 at 865 nm with respect to: (top panel) coincident and co-located values from the 17 ground-based AERONET sites at 870 nm; (middle panel) airborne PLASMA sunphotometer operated at 865 nm during ADRIMED; (bottom panel) results of the optical calculations at 865 nm according to Figure S12 from airborne measurements during TRAQA and ADRIMED. The solid line is the bisector. The dashed lines represent the limits indicated by the G_{frac} parameter. The characteristics of the linear correlation (number of points Nb, correlation coefficient, G_{frac}, RMS and bias) are also reported.

Figure 45. Scatter plots of daily AOD_F and AOD_C retrieved by POLDER-3 at 865 nm as a function of coincident AERONET values at 870 nm for the 17 sites in the western Mediterranean. The solid line is the bisector. The dashed lines represent the limits indicated by the G_{frac} parameter. The characteristics of the linear correlation (number of points Nb, correlation coefficient, G_{frac}, *RMS* and bias) are also reported. Note that, as discussed in sections 2.1 and 2.2, the definitions of AOD_F and AOD_C by POLDER-3 and AERONET are not the same.

Mis en forme : Police :Italique

Figure 5. Scatter plots of daily ΔAOD_F (top) and ΔAOD_C (bottom) retrieved by POLDER-3 at 865 nm as function of coincident AERONET values at 870 nm at the 17 sites of Western Mediterranean Sea. The AERONET ΔAOD_F and ΔAOD_C are calculated from the fine and coarse modes of the retrieved volume size distribution defined as below and above a threshold diameter ($D_{cut\text{-}off}$) corresponding to the minimum of the size distribution. The $D_{cut\text{-}off}$ is not fixed but can vary between 0.44 and 0.99 µm. The figure presents cases corresponding to AERONET retrievals yielding a separation of the fine and coarse modes of the volume distribution at $D_{cut\text{-}off}$ < 1.0 µm (left) and days with AERONET $D_{cut\text{-}off}$ ≥ 1.0 µm (right). The solid line is the bisector. The dashed lines represent the limits indicated by the ΔG_{frac} parameter. The characteristics of the linear correlation (number of points, correlation coefficient R, G_{frac}, RMS and bias) are also reported.

Figure 6. Same as figure 5 for cases corresponding to AERONET retrievals yielding a separation of the fine and coarse modes of the volume distribution at $D_{cut\text{-}off}$ < 1.0 µm (left) and days with AERONET $D_{cut\text{-}off}$ ≥ 1.0 µm (right).

Figure 67. Scatter plots of AOD_F (left) and AOD_C (right) retrieved by POLDER-3 at 865 nm and compared to values obtained by optical calculations from airborne measurements of the particle size number distribution. Panels, from top to bottom, represent the results of the calculations when varying the cut-off diameter between 0.4 and 1.0 µm. Characteristics of the linear correlation are also reported (number of points Nb, correlation coefficient R, RMS and bias). Error bars of in situ measurements were calculated from the optical calculation and the instrumental uncertainties. The solid line is the bisector.

Figure 78. Scatter plots of the Angström Exponent (AE) retrieved by POLDER-3 between 865 and 670 nm with respect to coincident and collocated values from: (top) the 17 ground-based AERONET sites between 870 and 675 nm; (middle) airborne PLASMA sun photometer operated at 870 and 675 nm during ADRIMED; (bottom) optical calculations at 865 and 670 nm from particle size number distributions measured in situ during TRAQA and ADRIMED. Only AERONET values corresponding to POLDER-3 AOD >0.1 are considered because of large uncertainties in AE at low AOD. To facilitate the reading, the standard deviations of the AERONET values are not represented. Characteristics of the linear correlations are also reported (number of points Nb, correlation coefficient R, RMS and bias).

Figure 89. Scatter plot of ΔAE versus ΔAOD retrieved by POLDER-3 (left) and AERONET (right) on coincidental days (N=6421) for the 17 stations of Western Mediterranean Sea. Mean and standard deviations (in brackets) of ΔAOD obtained by classifying the air masses into pollution (blue, $\Delta AE \geq 1.5$), mixed (green, $0.5 < \Delta AE < 1.5$) and desert dust (orange, $\Delta AE \leq 0.5$) according to Pace et al. (2006) are shown.

Figure 910. Scatterplot of the fraction of coarse mode optical depth due to non spherical particles (f_{ens}) retrieved by POLDER-3 and that of total optical depth (f_{ns}) estimated by AERONET. Values are expressed in percent. Only AERONET data points for which the measured ΔAOD exceeded 0.10 and the ΔAOD_C represented more than 30% of the total ΔAOD are represented. The solid line is the bisector. Dashed lines represent the interval of ± 25% of agreement between POLDER-3 f_{CNS} and AERONET f_{NS}.

Figure 101. Mean and standard deviations of coarse mode optical depth due to non spherical particles measured by POLDER-3 (f_{ens}, blue) and that of total optical depth estimated by AERONET (f_{ns}, red) classified into four classes: spherical (f_{ens} ≤25%); predominant spherical (25%< f_{ens} ≤50%), predominant non-spherical (50%< f_{ens} ≤75%); non-spherical (75%< f_{ens} ≤100%). Values are expressed in percent. Only AERONET data points for which the AOD >0.10 and AOD_C/AOD >0.30 are represented. The black triangles represent the number of points in each classes (the dashed curves is represented for increased readability).

Figure 112. Regional maps of average ΔAOD (top left), ΔAE, (top right), ΔAOD_F (middle left), ΔAOD_C (middle right), ΔAOD_{CNS} (top left), and ΔAOD_{CS} (bottom right) retrieved by POLDER-3 over the period March 2005-October 2013. Mean and standard deviations are also shown.

Mis en forme : Police :Italique

Table captions

Table 1. List of AERONET stations available in the western Mediterranean region retained for this study. The number of ocean POLDER pixel within 0.5° from the position of the station is indicated (N_{PIXEL}). The number of observations by POLDER-3 and AERONET between March 2005 to October 2013, and the number of coincident days (within brackets) are also reported .List of AERONET stations available in the western Mediterranean region with at least one ocean POLDER pixel (Nb_{POL}) within 0.5° around the station, together with the number of POLDER-3 vs. AERONET observations (and coincident days in brackets) for the different aerosol products from March 2005 to October 2013.

Table 2. List of vertical profiles made by the ATR-42 aircraft during the TRAQA and ADRIMED campaigns in coincidence with the passage of POLDER-3. For each profile is indicated: the flight number, the name of the profile, the date, the time period of the profile, the area covered by the flight, the geographical coordinates, the minimum and maximum altitude of the flight and then, the hour of POLDER-3 overpass in UTC.

Table 3. Criteria of classification of aerosol layers encountered on the vertical profiles of TRAQA and ADRIMED, based on nephelometer measurements of the scattering coefficient (σ_{scatt}) at 550 nm and on its spectral dependence (AE_{scatt}) between 450 and 700 nm.

Table 4. Summary of evaluated uncertainties on POLDER-3 advanced aerosol products *AOD*, *AE*, AOD_F, AOD_C, and f_{CNS}. N/A stands for not attributed.

Mis en forme : Police :Italique

Mis en forme : Police :Italique, Indice

Table 1. List of AERONET stations available in the western Mediterranean region retained for this study. The number of ~~with at least one~~ ocean POLDER pixel ~~(Nb_{POL})~~ within 0.5° from the position of the ~~around the~~ station is indicated (N_{PIXEL}). The ~~, together with the~~ number of observations by POLDER-3 and ~~vs.~~ AERONET between March 2005 to October 2013, and the number of coincident ~~observations (and coincident~~ days (~~in~~within brackets) are also reported ~~for the different aerosol products from March 2005 to October 2013~~.

AERONET station	Latitude, Longitude	Altitude (m)	AERONET period	~~$Nb_{POL}N_{PIXEL}$~~	AOD and AE	AOD_F and AOD_C	f_{CNS} and f_{NS}
					POLDER/AERONET (coincidences)		
Barcelona	41°23'N, 02°07'E	125	04/03/2005 - 10/10/2013	13	1171/2059 (827)	1171/1333 (514)	485/623 (116)
Villefranche-sur-Mer	43°41'N, 07°19'E	130	17/02/2005 - 21/08/2013	9	1097/1589 (641)	1097/999 (359)	470/452 (77)
Toulon	43°08'N, 06°00'E	50	04/03/2005 - 04/12/2010	9	1114/1503 (630)	1114/962 (343)	429/393 (67)
Ersa	43°00'N, 09°21'E	80	09/06/2008 - 11/10/2013	17	1178/1252 (541)	1178/676 (281)	504/240 (37)
Malaga	36°42'N, 04°28'W	40	23/02/2009 - 23/09/2013	10	1193/1359 (539)	1193/1036 (419)	465/377 (53)
Lampedusa	35°31'N, 12°37'E	45	06/03/2005 - 11/10/2013	28	1301/1177 (513)	1301/663 (307)	604/285 (54)
Messina	38°11'N, 15°34'E	15	01/05/2005 - 23/20/2012	9	1119/1340 (507)	1119/739 (281)	538/399 (63)
Roma Tor Vergata	41°50'N, 12°38'E	130	10/03/2005 - 11/10/2013	1	725/1954 (486)	725/1199 (280)	297/683 (66)
Blida	36°30'N, 02°52'E	230	06/03/2005 - 19/02/2012	7	989/1357 (475)	989/813 (280)	427/484 (85)
Burjassot	39°30'N, 00°25'W	30	16/04/2007 - 24/04/2013	1	668/1506 (372)	668/1045 (277)	249/480 (54)
Palma de Mallorca	39°33'N, 02°37'E	10	03/08/2011 - 10/10/2013	11	1136/524 (214)	1136/395 (155)	504/162 (19)
Porquerolles	43°00'N, 06°09'E	22	10/05/2007 - 17/07/2013	11	1106/537 (195)	1106/260 (95)	431/82 (9)
Frioul	43°15'N, 05°17'E	40	07/07/2010 - 11/10/2013	8	1037/481 (162)	1037/324 (118)	373/91 (10)
Gozo	36°02'N, 14°15'E	32	25/02/2013 - 11/10/2013	24	1320/210 (102)	1320/162 (67)	633/90 (9)
Montesoro Bastia	42°40'N, 09°26'E	49	26/07/2012 - 23/07/2013	14	1161/240 (76)	1161/43 (7)	506/12 (1)
Alboran	35°56'N, 03°02'E	15	29/06/2011 - 23/01/2012	29	1392/158 (73)	1392/103 (46)	609/47 (7)
Tizi Ouzou	36°41'N, 04°03'E	133	11/04/2012 - 11/10/2013	5	927/238 (68)	927/98 (26)	399/76 (3)
TOTAL	-	-	-	-	18634/18223 (6421)	18634/11228 (3855)	7923/4976 (730)

Mis en forme : Indice

Mis en forme : Indice

Table 2. List of vertical profiles made by the ATR-42 during the TRAQA and ADRIMED campaigns in coincidence with the passage of POLDER-3. For each profile is indicated: the flight number, the name of the profile, the date, the time period of the profile, the area covered by the flight, the geographical coordinates, the minimum and maximum altitude of the flight and then, the hour of POLDER-3 overpass in UTC.

Campaign	Flight ID	Profile ID	Date	Time (UTC)	Area	Geographical span		Altitude span (m asl)	POLDER-3 overpass (UTC)	PLASMA
						Beginning	end			
TRAQA	T-V21	T-V21-S1	27/06/2012	10h31–10h52	Corse	42°59'N–7°43'E	42°59'N–7°41'E	122–3534	14h19	----
	T-V24	T-V24-S1	03/07/2012	15h39–16h08	N-East Barcelona	42°14'N–3°31'E	42°8'N–3°29'E	77–3832	15h03	----
	T-V25	T-V25-S1	04/07/2012	08h32–09h04	South of France–Lion Gulf	41°28'N–6°0'E	41°31'N–6°0'E	100–4444	14h05	----
	T-V26	T-V26-S1		16h08–16h41		42°45'N–4°13'E	42°46'N–4°13'E	128–4684		----
	T-V27	T-V27-S1	06/07/2012	09h01–09h26	South of France	42°41'N–5°19'E	42°39'N -5°14'E	115–4723	13h47	----
		T-V27-S3		09h26–11h00		42°39'N - 5°15'E	42°42'N–5°19'E	76–3782		----
	T-V28	T-V28-S2		16h20–16h42		42°19'N–7°35'E	42°44'N–6°22'E	60–3784		----
ADRIMED	A-V28	A-V28-S2	14/06/2013	10h19–10h44	East Corse–Sardinia	41°38'N–7°14'E	42°4'N–6°46'E	69–3860	14h56	Yes
	A-V29	A-V29-S1	16/06/2013	08h19–08h32	Baleares–Sardinia	39°15'N–9°3'E	39°40'N–8°59'E	6–3877	14h37	Yes
		A-V29-S4		09h46–10h15		39°34'N - 4°29'E	39°39'N -4°29'E	52–4521		Yes
	A-V30	A-V30-S1	16/06/2013	11h59-12h10	Baleares–Sardinia	39°52'N - 4°13'E	39°32'N -3°48'E	93–3240	14:37	Yes
	A-V31	A-V31-S4	17/06/2013	09h41–09h54	Baleares–Sardinia	40°11'N–3°59'E	39°52'N–4°13'E	95–2899	15h18	Yes
	A-V32	A-V32-S1		11h46–12h05		39°52'N–4°13'E	39°56'N–4°36'E	93–4519		Yes
		A-V32-S4		13h30–13h44		39°32'N–9°10'E	39°16'N–9°2'E	10–3548		Yes
	A-V33	A-V33-S2	19/06/2013	12h47–13h17	Corse–Sardinia	43°01'N–9°23'E	43°1'N–9°20'E	73–4502	15h00	Yes
		A-V33-S4		14h46–14h59		39°15'N–9°24'E	39°15'N–9°4'E	5–3224		----
	A-V38	A-V38-S2	28/06/2013	12h25–13h30	Sardinia–Lampedusa	35°30'N–12°38'E	35°30'N–12°37'E	12–5427	14h26	----
	A-V44	A-V44-S1	04/07/2013	12h22–12h33	Gulf of Genoa–Corse–Sardinia	43°02'N–9°15'E	43°2'N–9°19'E	59–3513	15h11	----
		A-V44-S2		14h35–14h51		43°35'N–9°7'E	39°15'N–9°4'E	4–3499		----

Table 3. Criteria of classification of aerosol layers encountered on the vertical profiles of TRAQA and ADRIMED, based on nephelometer measurements of the scattering coefficient (σ_{scatt}) at 550 nm and on its spectral dependence (AE_{scatt}) between 450 and 700 nm.

Aerosol type	AE_{scatt}(450-700 nm)	σ_{scatt} (550 nm)
Clean background / maritime	–	< 5 or 10 Mm^{-1}
Desert dust	< 0.5	> 10 Mm^{-1}
Pollution	> 1	> 10 Mm^{-1}
Mixed (dust-dominated)	0.5 – 0.75	
Mixed (pollution-dominated)	0.75 – 1	

Mis en forme : Police :Italique

Mis en forme : Police :Italique

Table 4. Summary of evaluated uncertainties on POLDER-3 advanced products AOD, AE, AOD_F, AOD_C, and f_{CNS}, and comparison to previous evaluations. N/A stands for not attributed.

Products	**Uncertainties**	
	This work	**Previous work**
AOD	$\Delta AOD = \pm(0.003 + 0.04 \times AOD)$	$\Delta AOD = \pm(0.05 \times AOD + 0.05)^{\$}$
AE	$\Delta AE = \pm(0.11 + 0.44 \times AE)$	$\Delta AE = 0.3–0.5^{\$}$
AOD_F	$\Delta AOD_F = \pm(0.007 + 0.02 \times AOD_F)$	N/A
AOD_F ($D_{cut\text{-}off} < 1\ \mu m$)	$\Delta AOD_F = \pm(0.003 + 0.02 \times AOD_F)$	N/A
AOD_C	$\Delta AOD_C = \pm(0.01 + 0.04 \times AOD_C)$	N/A
f_{NCS}	$\Delta f_{CNS} = \pm 25\%$	N/A
AOD_{CS}	$\Delta AOD_{CS} = AOD_{CS} \times [(0.04 + 0.01/AOD_{CNS})^2 + ((1-\Delta f_{CNS})/(1-f_{CNS}))^2]^{1/2}$	N/A
AOD_{CNS}	$\Delta AOD_{CNS} = AOD_{CNS} \times [(0.04 + 0.01/AOD_{CNS})^2 + (\Delta f_{CNS}/f_{CNS})^2]^{1/2}$	N/A

[\$] Tanré et al.~~,~~ (2011) and references therein

Mis en forme : Police :Italique

Mis en forme : Police :Italique

Mis en forme : Police :Italique

Mis en forme : Police :Italique

Mis en forme : Police :Italique

Mis en forme : Police :Non Italique

Mis en forme : Police :Non Italique

Mis en forme : Police :Non Italique

Mis en forme : Police :Non Italique

Mis en forme : Police :Non Italique

Mis en forme : Police :Non Italique

Mis en forme : Police :Non Italique

Mis en forme : Police :Non Italique

Mis en forme : Police :Non Italique

Mis en forme : Police :Non Italique

Mis en forme : Police :Non Italique

Mis en forme : Police :Non Italique

Mis en forme : Police :Non Italique

Mis en forme : Police :Non Italique

Mis en forme : Police :Non Italique

Mis en forme : Police :Non Italique

Mis en forme : Police :Non Italique

Mis en forme : Police :Non Italique

Mis en forme : Police :Non Italique

Mis en forme : Police :Non Italique

Mis en forme : Police :Non Italique

Mis en forme : Police :Non Italique

Mis en forme : Police :Non Italique

Mis en forme : Police :Non Italique

Mis en forme : Police :Non Italique

Mis en forme : Police :Non Italique

Mis en forme : Police :Non Italique

Mis en forme : Police :Non Italique

Figure 1. Map of the location of the 17 AERONET ground-based stations considered in this work.

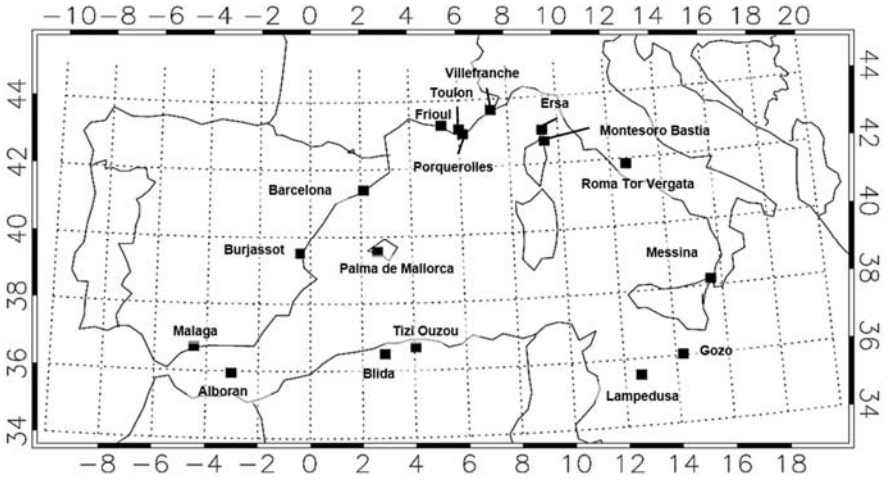

Figure 2. Iterative data inversion procedure to retrieve the aerosol optical depth (AOD, AOD_F and AOD_C) and Angstrom exponent (AE) measured by POLDER-3 from airborne observations. Green boxes indicate the input values from airborne measurements (size distribution, scattering and extinction coefficients) and the initial values of the complex refractive indexes estimated from published literature. The iterative steps of the procedure are indicated in the blue boxes. The results of optical calculations (corrected size distribution, scattering and extinction coefficients) are in the orange boxes.

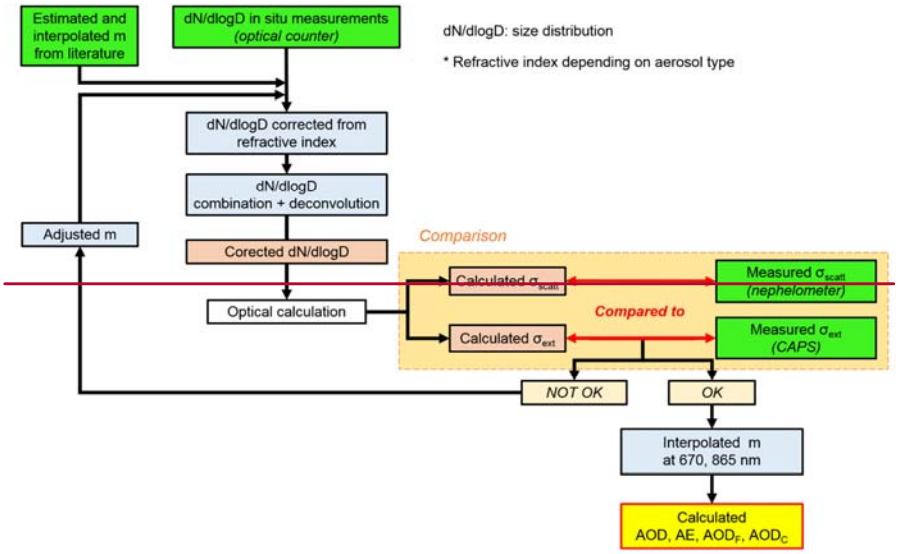

Mis en forme : Espace Avant : 0 pt, Interligne : simple

Figure ~~3~~2. Flight tracks of the ATR~~-~~42 aircraft (coloured lines) during the TRAQA and ADRIMED campaigns. Only flights relevant to this study are presented. The location of the profiles coincidental, at their lowermost altitude, with a POLDER-3 overpass is shown by a circle. During the TRAQA campaigns, 7 profiles were retained for comparison on 6 flights. During the ADRIMED campaign, 12 profiles occurring during 9 flights were retained. In this second case, symbols are not always visible ~~as~~ due to overlapping.

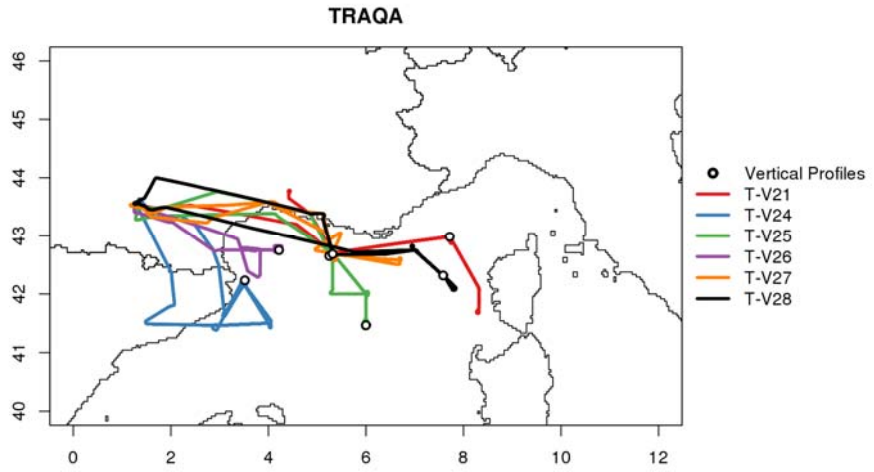

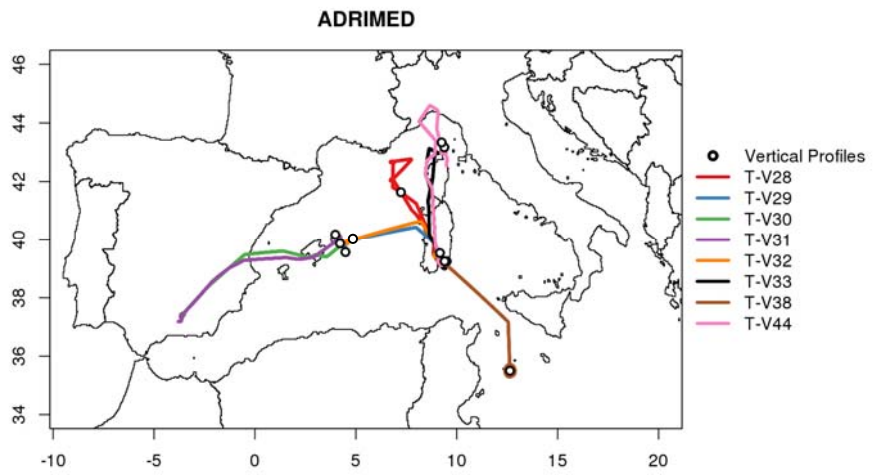

Figure 43. Scatterplots of daily *AOD* retrieved by POLDER-3 at 865 nm with respect to: (top panel) coincident and co-located values from the 17 ground-based AERONET sites at 870 nm; (middle panel) airborne PLASMA sun-photometer operated at 865 nm during ADRIMED; (bottom panel) results of the optical calculations at 865 nm according to Figure 1 from airborne measurements during TRAQA and ADRIMED. The solid line is the bisector. The dashed lines represent the limits indicated by the ~~G_{frac}~~ parameter. ~~The characteristics of the linear correlation (number of points *N*, correlation coefficient *R*, G_{frac}, *RMS* and bias) are also reported.~~

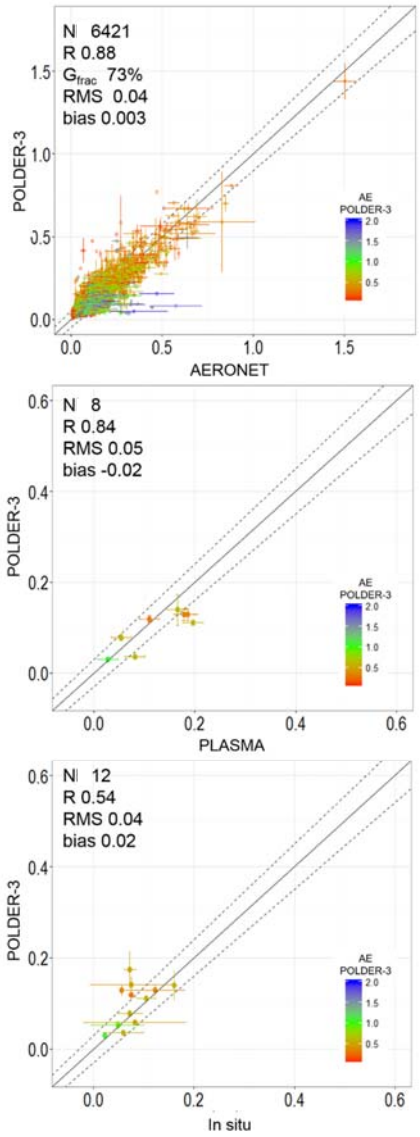

Mis en forme : Police :Italique

Mis en forme : Police :Italique

Mis en forme : Police :Italique

Mis en forme : Police :Italique

Mis en forme : Police :Italique

Mis en forme : Police :Italique

Figure ~~54~~. Scatter plots of daily AOD_F and AOD_C retrieved by POLDER-3 at 865 nm as a function of coincident AERONET values at 870 nm for the 17 sites of Western Mediterranean Sea. The solid line is the bisector. The dashed lines represent the limits indicated by the ~~G_{frac}~~ parameter. ~~The~~ characteristics of the linear correlation (number of points ~~N~~, correlation coefficient ~~R~~, ~~G_{frac}~~, ~~RMS~~ and bias) are also reported. ~~Note that, as discussed in sections 2.1 and 2.2, the definitions of AOD_F and AOD_C by POLDER-3 and AERONET are not the same.~~

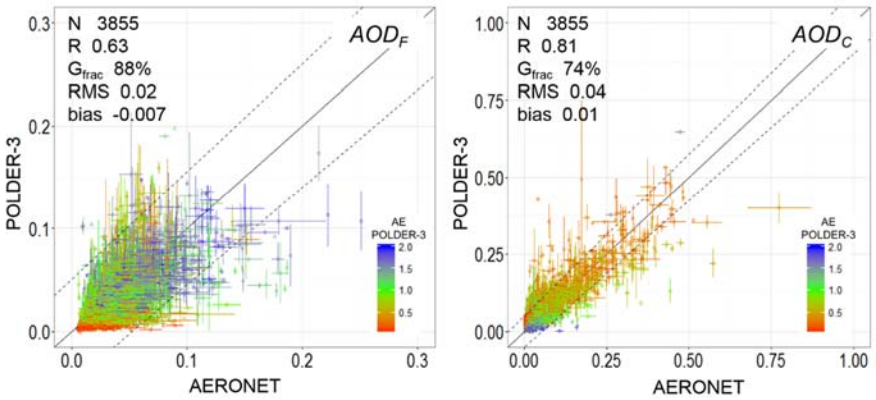

Mis en forme : Police :Italique
Mis en forme : Police :Italique
Mis en forme : Police :Italique
Mis en forme : Police :Italique
Mis en forme : Police :Italique
Mis en forme : Police :Italique
Mis en forme : Police :Italique
Mis en forme : Police :Italique
Mis en forme : Police :Italique, Indice
Mis en forme : Police :Italique
Mis en forme : Police :Italique, Indice

Figure 65. Scatter plots of daily AOD_F (top) and AOD_C (bottom) retrieved by POLDER-3 at 865 nm as function of coincident AERONET values at 870 nm at the 17 sites of Western Mediterranean Sea. The AERONET AOD_F and AOD_C are calculated from the fine and coarse modes of the retrieved volume size distribution defined as below and above a threshold diameter ($D_{cut-off}$) corresponding to the minimum of the size distribution. The $D_{cut-off}$ is not fixed but can vary between 0.44 and 0.99 µm. The figure presents for cases corresponding to AERONET retrievals yielding a separation of the fine and coarse modes of the volume distribution at $D_{cut-off}$ < 1.0 µm (left) and days with AERONET $D_{cut-off}$ ≥ 1.0 µm (right). The solid line is the bisector. The dashed lines represent the limits indicated by the G_{frac} parameter. The characteristics of the linear correlation (number of points N, correlation coefficient R, G_{frac}, RMS and bias) are also reported.

(a) AOD_F

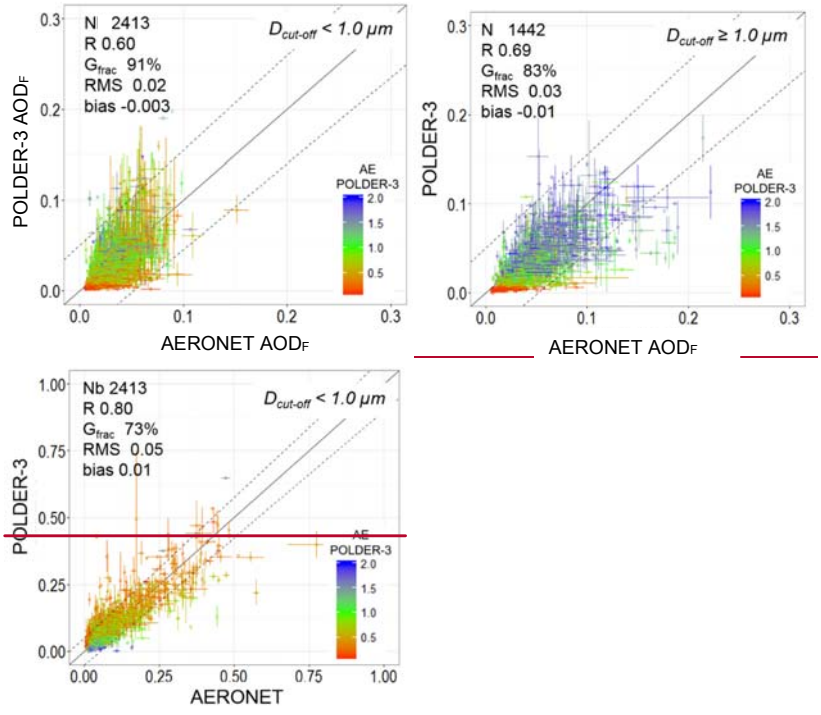

(b) AOD_C

Mis en forme : Police :Italique
Mis en forme : Police :Italique
Mis en forme : Police :Italique
Mis en forme : Police :Italique, Indice
Mis en forme : Police :Italique
Mis en forme : Police :Italique, Indice
Mis en forme : Police :11 pt, Italique, Anglais (États-Unis)
Mis en forme : Police :11 pt, Italique, Anglais (États-Unis), Indice
Mis en forme : Police :Italique
Mis en forme : Police :Italique
Mis en forme : Police :Italique
Mis en forme : Police :Italique
Mis en forme : Police :Italique
Mis en forme : Police :Italique
Mis en forme : Police :Italique

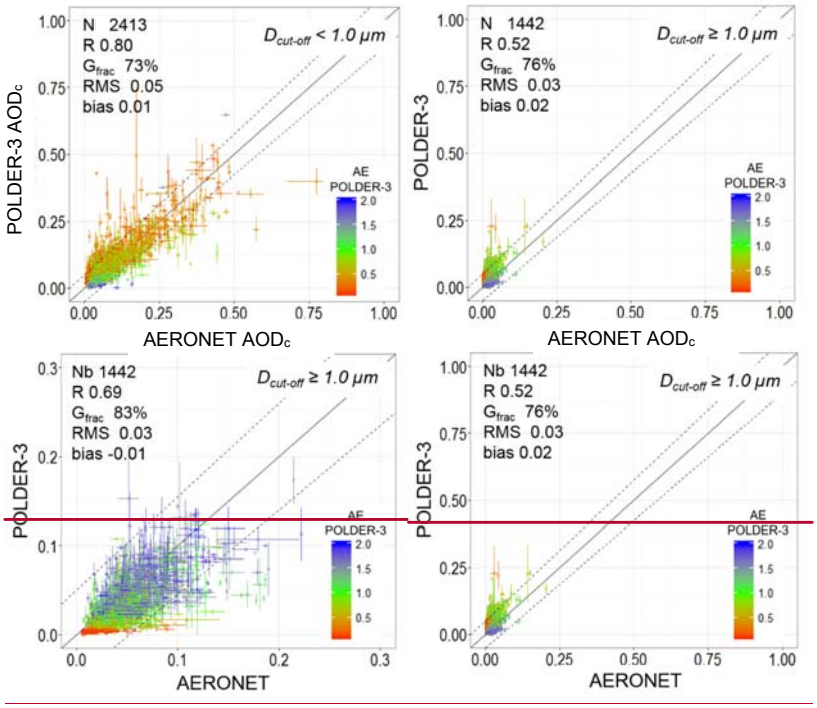
N 2413
R 0.80
G_{frac} 73%
RMS 0.05
bias 0.01
$D_{cut-off}$ < 1.0 µm
AE POLDER-3
POLDER-3 AOD_c
AERONET AOD_c
N 1442
R 0.52
G_{frac} 76%
RMS 0.03
bias 0.02
$D_{cut-off}$ ≥ 1.0 µm
POLDER-3
Nb 1442
R 0.69
G_{frac} 83%
RMS 0.03
bias -0.01
AERONET
Nb 1442
R 0.52
G_{frac} 76%
RMS 0.03
bias 0.02

Figure ~~7~~6. Scatter plots of AOD_F (left) and AOD_C (right) retrieved by POLDER-3 at 865 nm and compared to values obtained by optical calculations from airborne measurements of the number size distribution. Panels, from top to bottom, represent the results of the calculations when varying the cut-off diameter between 0.4 and 1.0 µm. Characteristics of the linear correlation are also reported (number of points ~~*N*~~, correlation coefficient ~~*R*~~, ~~*RMS*~~ and bias). ~~Error bars of in situ measurements~~ were calculated from the optical calculation and the instrumental uncertainties. The solid line is the bisector.

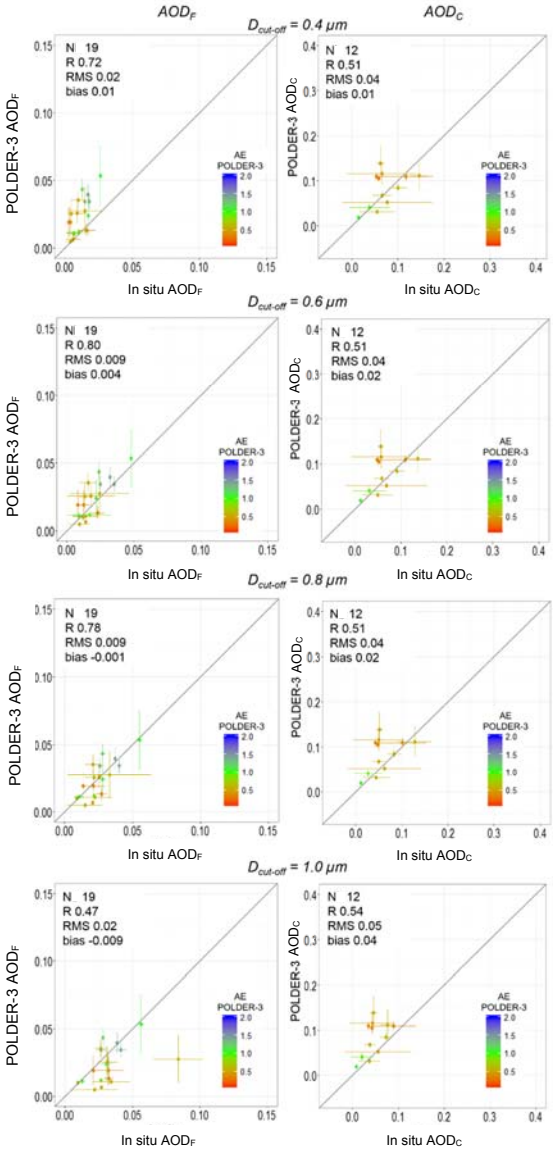

Mis en forme : Police :Italique
Mis en forme : Police :Italique
Mis en forme : Police :Italique
Mis en forme : Police :Italique
Mis en forme : Police :Italique

Figure ~~8~~7. Scatter plots of the Angström Exponent (*AE*) retrieved by POLDER-3 between 865 and 670 nm with respect to coincident and collocated values from (top) the 17 ground-based AERONET sites between 870 and 675 nm; (middle) airborne PLASMA sun-photometer operated at 870 and 675 nm during ADRIMED; (bottom) optical calculations at 865 and 670 nm from number size distributions measured in situ during TRAQA and ADRIMED. Only AERONET values corresponding to POLDER-3 *AOD* larger than 0.1 are considered. To facilitate the reading, the standard deviations of the AERONET values are not represented. Characteristics of the linear correlations are also reported (number of points *N*, correlation coefficient *R*, *RMS* and bias).

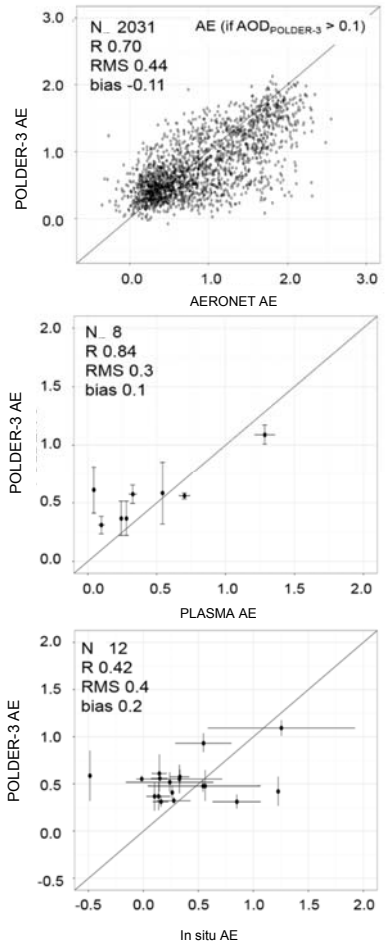

Mis en forme : Police :Italique

Mis en forme : Police :Italique

Mis en forme : Police :Italique

Mis en forme : Police :Italique

Figure 9108. Scatter plot of *AE* versus *AOD* retrieved by POLDER-3 (left) and AERONET (right) on coincidental days (*N* =6421) for the 17 stations of Western Mediterranean Sea. Mean and standard deviations (in brackets) of *AOD* obtained by classifying the air masses into pollution (blue, *AE* ≥ 1.5), mixed (green, 0.5 < *AE* < 1.5) and desert dust (orange, *AE* ≤ 0.5) according to Pace et al. (2006) are shown.

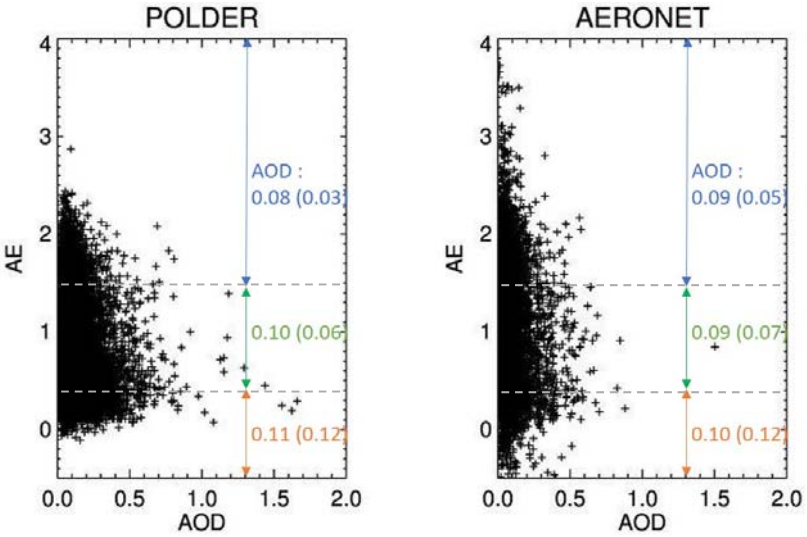

Mis en forme : Police :Italique
Mis en forme : Police :Italique
Mis en forme : Police :Italique
Mis en forme : Police :Italique
Mis en forme : Police :Italique
Mis en forme : Police :Italique
Mis en forme : Police :Italique
Mis en forme : Anglais (États-Unis)

Figure ~~10~~119. a) Scatterplot of the fraction of coarse mode optical depth due to non-spherical particles (f_{nsCRs}~~f_{CNS}~~) retrieved by POLDER-3 and that of total optical depth (f_{nsNS}~~f_{NS}~~) estimated by AERONET. Values are expressed in percent. As the AERONET f_{NS} depends on the total aerosol optical depth, o~~O~~nly ~~AERONET~~ data points for which the measured *AOD* exceeded 0.10 and the AOD_C represented more than 30% of the total *AOD* are represented. The solid line is the bisector. Dashed lines represent the interval of ± 25% of agreement between POLDER-3 f_{CNS} and AERONET f_{NS}. B) Mean and standard deviations of coarse mode optical depth due to non-spherical particles measured by POLDER-3 (f_{CNS}, blue) and that of total optical depth estimated by AERONET (f_{NS}, red) classified into four classes: spherical (f_{CNS} ≤25%); predominant spherical (25%< f_{CNS} ≤50%), predominant non-spherical (50%< f_{CNS} ≤75%); non-spherical (75%< f_{CNS} ≤100%). Values are expressed in percent. Only AERONET data points for which the *AOD* >0.10 and AOD_C/AOD >0.30 are represented. The black triangles represent the number of points in each class (the dashed curve is represented for increased readability)..

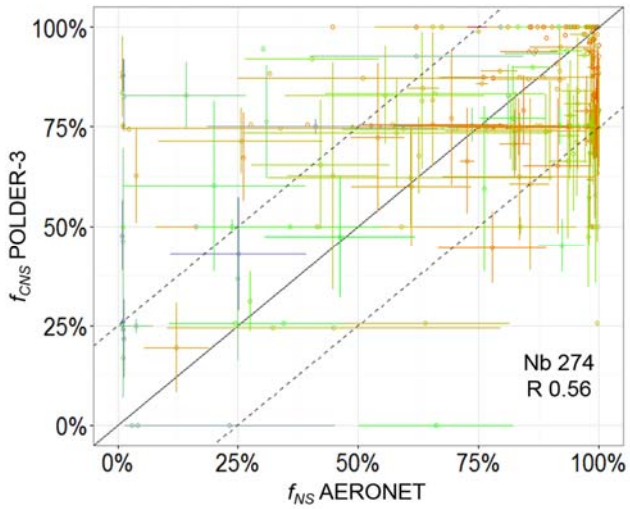

Mis en forme : Indice
Mis en forme : Police :Italique
Mis en forme : Police :Italique
Mis en forme : Police :Italique
Mis en forme : Police :Italique
Mis en forme : Police :Italique
Mis en forme : Anglais (États-Unis)
Mis en forme : Pas de saut de page avant

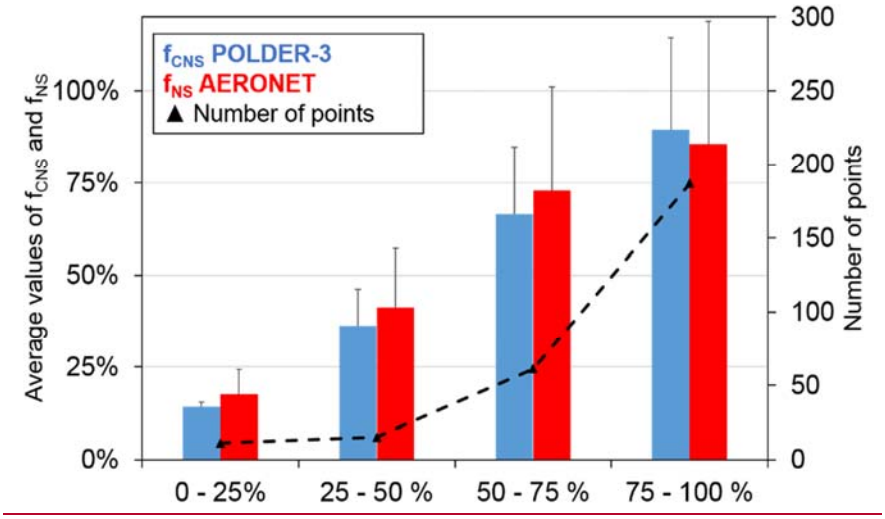
f_{CNS} POLDER-3
f_{NS} AERONET
▲ Number of points
Average values of f_{CNS} and f_{NS}
100%
75%
50%
25%
0%
300
250
200
150
100
50
0
Number of points
0 - 25%
25 - 50 %
50 - 75 %
75 - 100 %

Figure 1011. Scatterplot of the POLDER-3 coarse non-spherical AOD (AOD_{CNS}) as a function of AERONET non-spherical AOD (AOD_{NS}) at 865 nm for the same data set. The number of points and the regression coefficient R are shown. The solid think line represents the 1:1 line.

~~Mean and standard deviations of coarse mode optical depth due to non-spherical particles measured by POLDER-3 (f_{cns}, blue) and that of total optical depth estimated by AERONET (f_{ns}, red) classified into four classes: spherical (f_{cns} ≤25%); predominant spherical (25%< f_{cns} ≤50%), predominant non-spherical (50%< f_{cns} ≤75%); non-spherical (75%< f_{cns} ≤100%). Values are expressed in percent. Only AERONET data points for which the ΔAOD >0.10 and $\Delta AOD_C/AOD$ >0.30 are represented. The black triangles represent the number of points in each classes (the dashed curves is represented for increased readability).~~

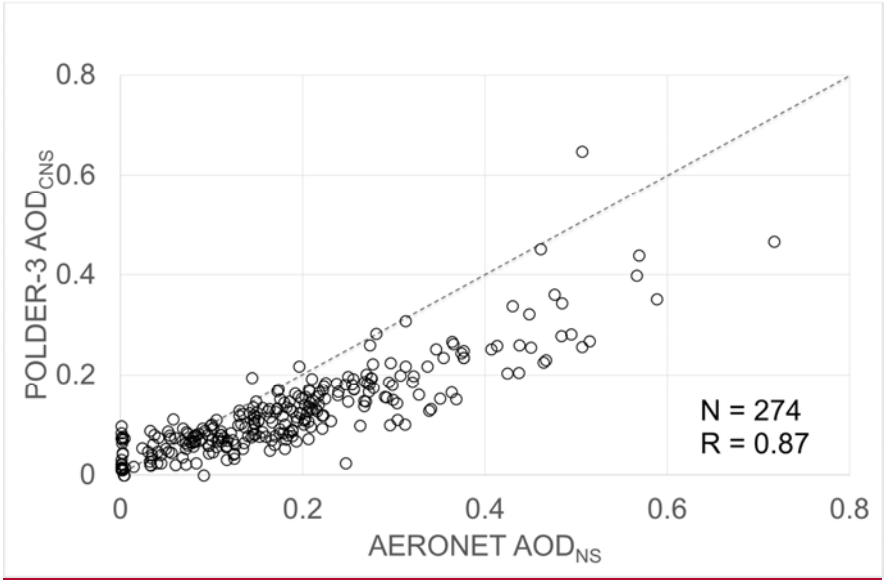

Mis en forme : Pas de saut de page avant

Mis en forme : Police :Italique

Mis en forme : Police :Italique

Mis en forme : Police :Italique

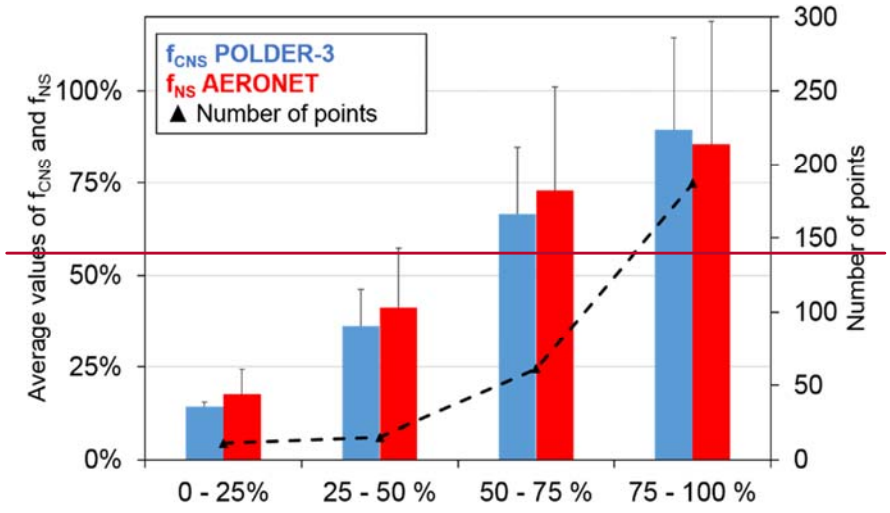

Mis en forme : Anglais (États-Unis)

Figure 1112. Regional maps for *AOD*, *AE*, AOD_F (top panel from left to right), AOD_C, AOD_{CNS} and AOD_{CS} (bottom panel from left to right) retrieved by POLDER-3 for the period March 2005-October 2013. Mean and standard deviations over the whole marine area of the window are also shown.

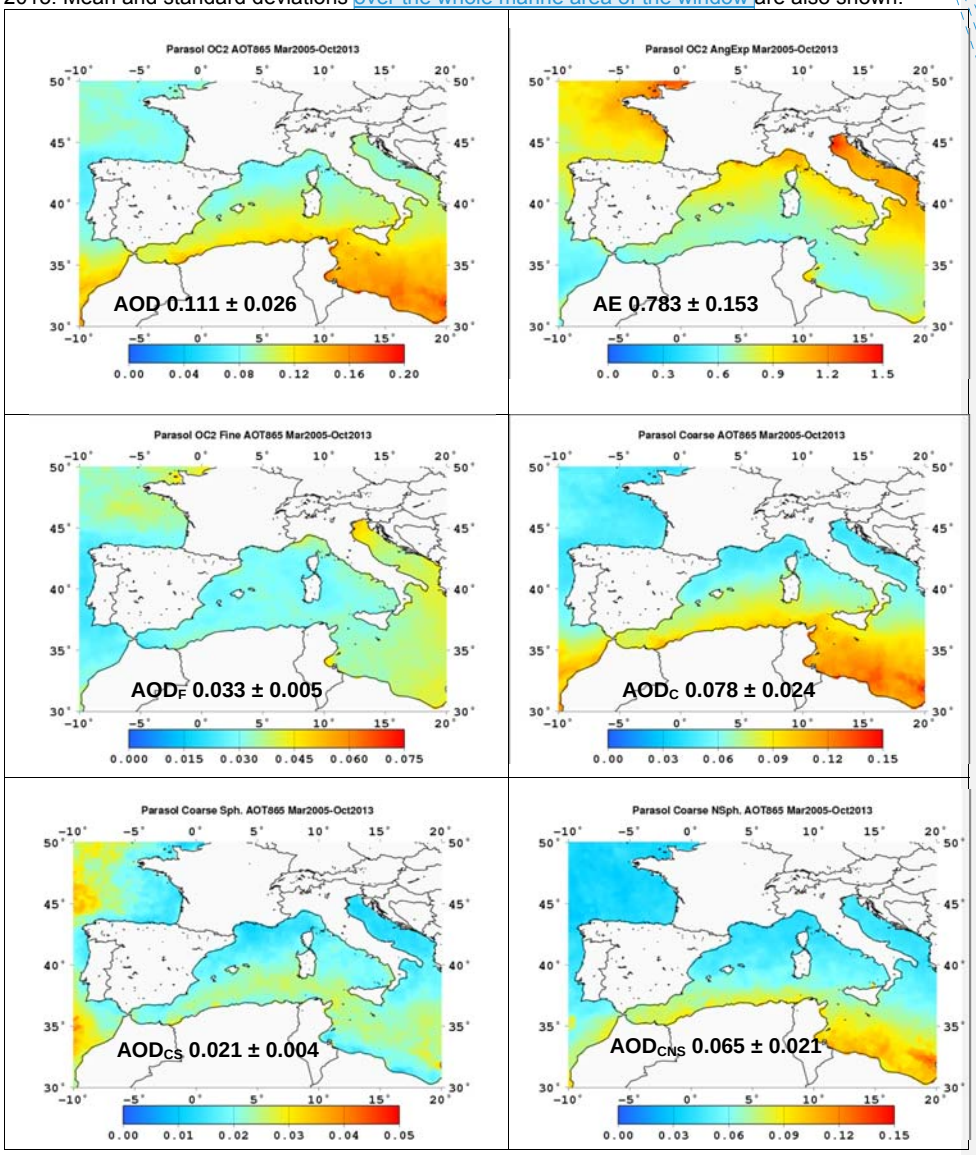

Mis en forme : Police :Italique

Mis en forme : Police :Italique

Mis en forme : Police :Italique

Mis en forme : Police :Italique

Mis en forme : Police :Italique

Mis en forme : Police :Italique

Commenté [d3]: Or over the Mediterranean marine area only?

Page 20 : [1] Mis en forme	Paola Formenti	07/11/2018 10:05:00

Police :Italique

Page 20 : [2] Mis en forme	dulac	09/11/2018 22:58:00

Police :Italique

Page 20 : [3] Mis en forme	dulac	09/11/2018 22:57:00

Police :Italique

Page 20 : [4] Mis en forme	dulac	09/11/2018 22:58:00

Police :Italique

Page 20 : [5] Mis en forme	dulac	09/11/2018 22:58:00

Police :Italique

Page 20 : [6] Mis en forme	dulac	09/11/2018 22:57:00

Police :Italique

Page 20 : [7] Mis en forme	dulac	09/11/2018 22:57:00

Police :Italique

Page 20 : [8] Mis en forme	dulac	09/11/2018 22:57:00

Police :Italique

Page 20 : [9] Mis en forme	Paola Formenti	07/11/2018 10:05:00

Police :Italique

Page 20 : [10] Mis en forme	dulac	09/11/2018 22:57:00

Police :Italique

Page 20 : [11] Mis en forme	dulac	09/11/2018 22:57:00

Police :Italique

Page 20 : [12] Mis en forme	Paola Formenti	07/11/2018 10:05:00

Police :Italique

Page 20 : [13] Mis en forme	dulac	09/11/2018 22:57:00

Police :Italique

Page 20 : [14] Mis en forme	dulac	09/11/2018 22:57:00

Police :Italique

Page 20 : [15] Mis en forme	dulac	09/11/2018 22:57:00

Police :Italique

Page 20 : [16] Mis en forme	Paola Formenti	07/11/2018 10:05:00

Police :Italique

Page 20 : [17] Mis en forme	Paola Formenti	07/11/2018 10:05:00

Police :Italique

Page 20 : [18] Mis en forme	Paola Formenti	07/11/2018 10:05:00

Police :Italique

Page 20 : [19] Mis en forme	Paola Formenti	07/11/2018 10:05:00

Police :Italique

Page 20 : [20] Mis en forme	dulac	09/11/2018 22:57:00

Police :Italique

Page 20 : [21] Mis en forme	Paola Formenti	07/11/2018 10:05:00

Police :Italique

Page 20 : [22] Mis en forme	dulac	09/11/2018 22:56:00

Police :Italique

Page 20 : [23] Mis en forme	dulac	09/11/2018 22:56:00

Police :Italique

Page 20 : [24] Mis en forme	Paola Formenti	07/11/2018 10:05:00

Police :Italique

Page 20 : [25] Mis en forme	dulac	09/11/2018 22:56:00

Police :Italique

Page 20 : [26] Mis en forme	dulac	09/11/2018 22:56:00

Police :Italique

Page 20 : [27] Mis en forme	dulac	09/11/2018 22:56:00

Police :Italique

Page 20 : [28] Mis en forme	dulac	09/11/2018 22:56:00

Police :Italique

Page 20 : [29] Mis en forme	dulac	09/11/2018 22:56:00

Police :Italique

Page 20 : [30] Mis en forme	dulac	09/11/2018 22:55:00

Police :Italique

Page 20 : [31] Mis en forme	Paola Formenti	07/11/2018 10:06:00

Police :Italique

Page 20 : [32] Mis en forme	dulac	09/11/2018 22:55:00

Police :Italique

Page 20 : [33] Mis en forme	Paola Formenti	07/11/2018 10:06:00

Police :Italique

Page 20 : [34] Mis en forme	dulac	09/11/2018 22:55:00

Police :Italique

Page 20 : [35] Mis en forme	dulac	09/11/2018 22:55:00

Police :Italique

Page 20 : [36] Mis en forme	Paola Formenti	07/11/2018 10:06:00

Police :Italique

Page 20 : [37] Mis en forme	dulac	09/11/2018 22:55:00

Police :Italique

Page 20 : [38] Mis en forme	dulac	09/11/2018 22:55:00

Police :Italique

Page 20 : [39] Mis en forme	Paola Formenti	07/11/2018 10:06:00

Police :Italique

Page 20 : [40] Mis en forme	Paola Formenti	07/11/2018 10:06:00

Police :Italique

Page 20 : [41] Mis en forme	dulac	09/11/2018 22:54:00

Police :Italique

Page 20 : [42] Mis en forme	dulac	09/11/2018 22:54:00

Police :Italique

Page 20 : [43] Mis en forme	dulac	09/11/2018 22:54:00

Police :Italique

Page 20 : [44] Mis en forme	dulac	09/11/2018 22:54:00

Police :Italique

Page 20 : [45] Mis en forme	Paola Formenti	07/11/2018 10:06:00

Police :Italique

Page 20 : [46] Mis en forme	dulac	09/11/2018 22:54:00

Police :Italique

Page 20 : [47] Mis en forme	dulac	09/11/2018 22:54:00

Police :Italique

Supplementary material of Formenti et al., Aerosol optical properties derived from POLDER-3/PARASOL (2005-2013) over the western Mediterranean sea: I. Quality assessment with AERONET and in situ airborne observations

Table S1. Modal diameter (D_0), geometric standard deviation (σ_0) and effective diameter (D_{eff}) of the log-normal distribution as well as real part of the refractive index (m_r) of the aerosol models over ocean of the POLDER-3 Look-Up Table (LUT). The imaginary part of the refractive index (m_i) is assumed as zero.

Parameters	Fine mode	Spherical coarse mode	Non spherical coarse mode
D_0 (µm)	0.08, 0.16, 0.20, 0.26	1.56	0.90, 1.50
σ_0	0.46	0.69	0.69
D_{eff} (µm)	0.136, 0.272, 0.34, 0.442	5.10	2.96, 4.92
m_r	1.35, 1.45, 1.60	1.33, 1.35, 1.37	1.53

Mis en forme : Police :Italique
Mis en forme : Police :Italique
Mis en forme : Police :Italique
Mis en forme : Police :Italique
Mis en forme : Police :Italique
Mis en forme : Police :Italique, Indice

Figure S1. Iterative data inversion procedure to retrieve from airborne observations the aerosol optical depth (AOD, AOD_F and AOD_C) and Angstrom exponent (AE) as measured by POLDER-3. Green boxes indicate the input values from airborne measurements (size distribution, scattering and extinction coefficients) and the initial values of the complex refractive indices estimated from published literature. The iterative steps of the procedure are indicated in the blue boxes. The results of optical calculations (corrected size distribution, scattering and extinction coefficients) are in the orange boxes.

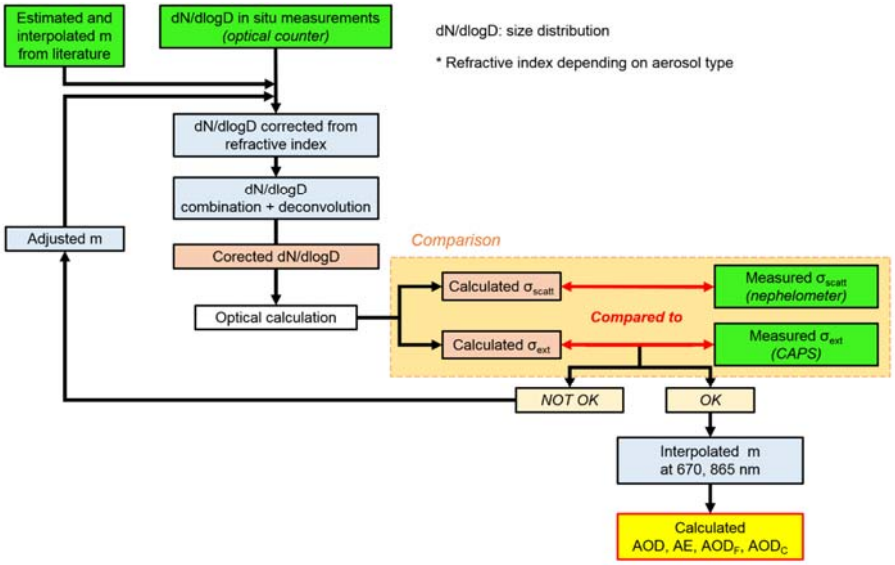

Figure ~~S1~~S2. Ratio of the coarse to the total AOD (AOD_C/AOD) by AERONET as a function of the cut-off diameter ($D_{cut\text{-}off}$) between the fine and coarse aerosol particle modes.

Mis en forme : Police :Italique

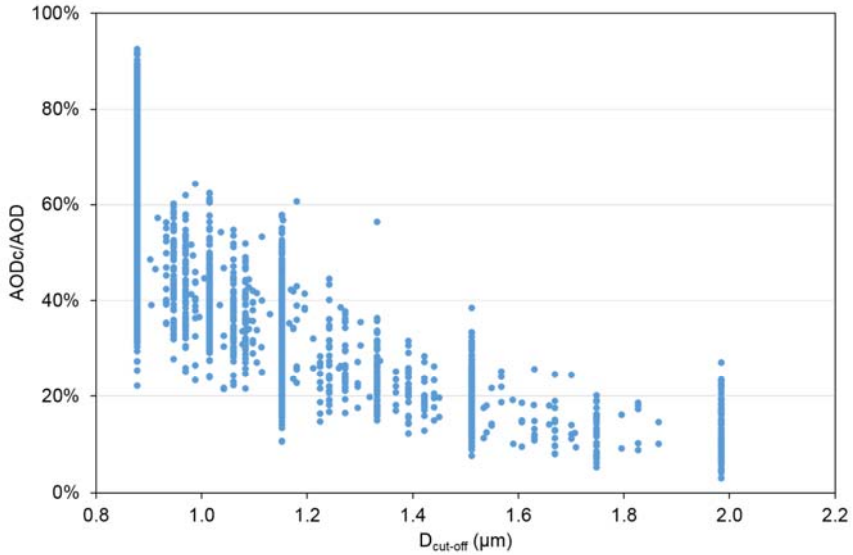

Supplementary A. Assessment of the size distribution

Here we provide details of the procedure to estimate the aerosol particle size distribution from the measurements of the PCASP, UHSAS and Grimm optical counters operated on board the ATR42 during TRAQA and ADRIMED. This also requires to assess the particles complex refractive index.

S.1. Correction for complex refractive index

The operating principle of the particle optical counters is based on the angular dependence of the light scattering intensity to the particle size through optical Mie theory (Mie, 1908; Wendisch and Brenguier, 2013). The optical particle counters provide the number size distribution at an optical equivalent diameter (D_{EO}) corresponding to the measured intensity of the scattered radiation at the value of the complex refractive index m used for calibration. This is generally done with latex spheres (or equivalent standard material) for which m is equal to 1.59 – i0 at 638 nm. Henceforth, to represent the actual aerosol, the value of D_{EO} needs to be converted into a particle equivalent geometrical diameter (D_{EG}), corresponding to the real value of the complex refractive index. This correction depends on aerosol composition and the geometrical and spectral characteristics of the particle counter (Reid et al., 2003; Denjean et al, 2016).

The equivalence between D_{EO} and D_{EG} was established by calculation using the Mie theory for homogeneous spherical particles (Bohren and Huffman, 1998). Examples of this equivalence for a range of m values is shown in Figure ~~S2~~ S3 for the particle optical counters used in this study (UHSAS, PCASP and Grimm).

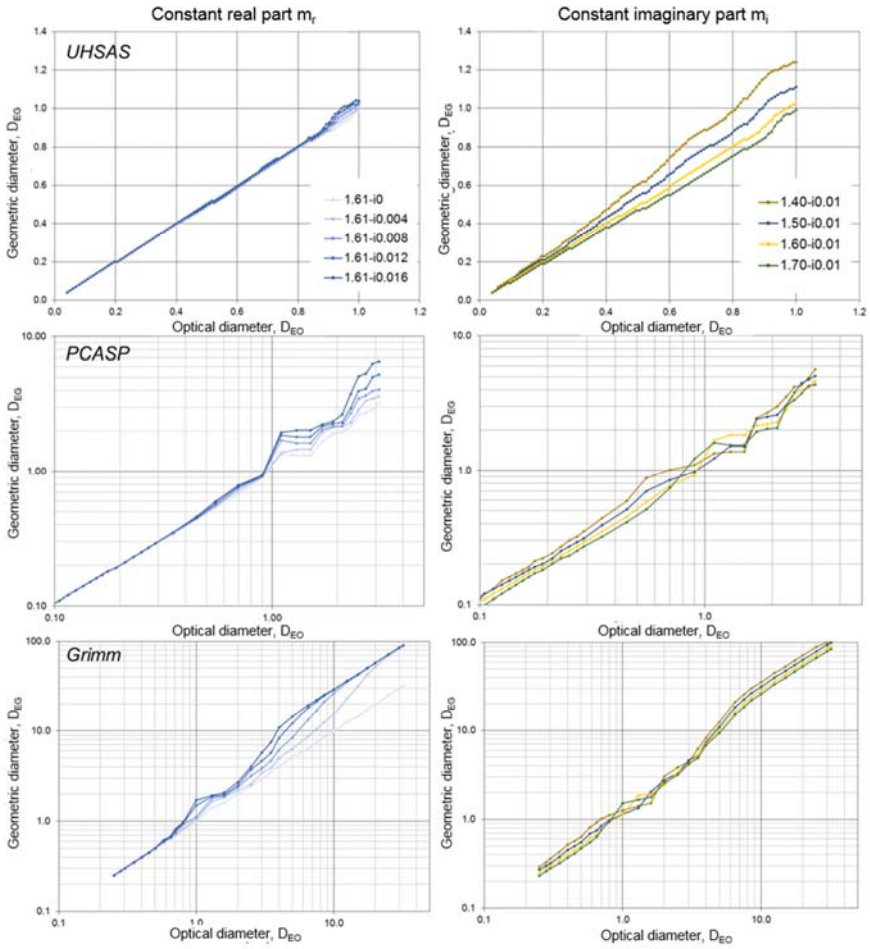

Figure S3~~2~~. Scatterplot of the geometric-equivalent diameter (D_{EG}) with respect to the optical-equivalent diameter (D_{EO}) for various refractive indices with real part fixed at 1.61 (left) and imaginary part fixed at 0.01 (right), for UHSAS (top), PCASP (middle), and Grimm (bottom).

The relation between D_{EO} and D_{EG} is not linear with size. The real and imaginary parts of the refractive index modify significantly the particle diameter, notably above 0.6 µm. The imaginary part of the refractive index has a greater influence at diameters larger than 1 µm, whereas the real part affects more the submicron aerosols. Figure ~~A1~~ S3 also shows the equivalence between D_{EO} and D_{EG} is not unique, especially for D_{EO} around 1 µm.

Mis en forme : Police :Non Italique
Mis en forme : Police :Non Italique
Mis en forme : Police :Non Italique
Mis en forme : Police :Italique
Mis en forme : Police :Italique

S.2. Combination of optical counter measurements

The combination of the size spectra measured by the PCASP, UHSAS, and Grimm was performed by examining their overlap over their common measurement size ranges. The combination was performed as follows. First, the measured size distributions were visually inspected to establish whether, at the calibration refractive index (m_{latex} = 1.59 -0i), the observations by the counters coincided on their common size range. This analysis was repeated after applying the geometric equivalence correction according to the refractive index (that is, on the size distributions expressed as a function of D_{EG}). When the difference between the particle number concentration measured by the two counters (at pairs) was lower than the sum of the absolute counting errors ($\sqrt{dN}$ according to the Poisson statistics), the agreement was considered as satisfactory. A boundary diameter (D_{cover}) was then defined in the overlap zone to generate a new combined size distribution from the PCASP or UHSAS in the particle diameter range $D'_{EG} \leq D_{COVER}$ and the Grimm counter in the range $D''_{EG} \geq D_{COVER}$ (with D''_{EG} up to the AVIRAD inlet cut-off diameter), so that

$$\frac{dN_{tot}(D_{EG})}{dlogD_{EG}} = \frac{dN_{PCASP}(D'_{EG})}{dlogD'_{EG}} + \frac{dN_{Grimm}(D''_{EG})}{dlogD''_{EG}} \quad \textbf{(S1.a)}$$

$$\frac{dN_{tot}(D_{EG})}{dlogD_{EG}} = \frac{dN_{UHSAS}(D'_{EG})}{dlogD'_{EG}} + \frac{dN_{Grimm}(D''_{EG})}{dlogD''_{Eg}} \quad \textbf{(S1.b)}$$

Figure ~~S3~~ **S4** shows a schematic representation of the combination between both size distributions.

Mis en forme : Police :Italique

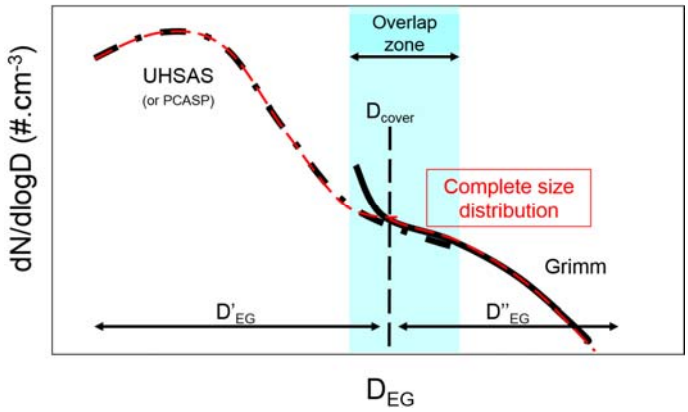

Figure ~~S3~~S4. Schematics of the combination of the number size distributions between UHSAS (or PCASP) and Grimm around D_{cover}. The overlap zone is indicated in blue. The black curves represent the distributions measured by the two counters in pairs, corrected by the refractive index (e.g., expressed as D_{EG}). The red curves represent the combined size distributions of the two optical counters over the combination of the domain of D_{EG}' (for UHSAS or PCASP) and D_{EG}'' for the Grimm. In each diameter range below and over D_{COVER}, dlogD_{EG} values and counting errors remain those of the respective counter.

The overlapping zone changes whether we work with PCASP (TRAQA campaign) or UHSAS (ADRIMED campaign). D_{cover} ranged between 0.23 and 0.7 µm for the TRAQA campaign when the PCASP and the Grimm were operated, and between 0.23 and 0.9 µm during ADRIMED when the UHSAS and the Grimm were operated.

Mis en forme : Police :Italique

To make sure that the total number of particles was conserved after the recombination and the modification of the size classes by the refractive index, we applied the conservation equation of the total number of particles

$$N_{EG} = N_{EO} \quad \textbf{(S2.a)}$$

$$N_{EO} = \int_{D_{EO,min}}^{D_{EO,max}} \frac{dN_{EO}(D_{EO})}{dlogD_{EO}} dlogD_{EO} \quad \textbf{(S2.b)}$$

$$N_{EG} = \int_{D_{EG,min}}^{D_{EG,max}} \frac{dN_{EG}(D_{EG})}{dlogD_{EG}} dlogD_{EG} \quad \textbf{(S2.c)}$$

where N_{EO} is the total number of particles corresponding to the measurement (for the refractive index m_{latex}) and N_{EG} is the total number of particles after correction of the refractive index.

Finally, the extended size distributions $\frac{dN_{EG}(D_{EG})}{dlogD_{EG}}$ obtained by the recombination of the optical particle counters were fitted by a multi modal normalized log-normal distributions as

$$\frac{1}{N_{EG}} \frac{dN_{EG}(D_{EG})}{dlogD_{EG}} = \sum_i \frac{n_i}{\sigma_i \sqrt{2\pi}} \exp\left(-\frac{(logD - logD_{0,i})^2}{2\sigma_i^2}\right) \quad \textbf{(S3)}$$

where n_i is the total number of particles, σ_i the geometric standard deviation and $D_{0,i}$ the modal (geometric mean) diameter of the mode i.

The log-normal fit of the reconstructed size distribution was done with the MPFIT routine available under IDL (Markwardt, 2009; http://purl.com/net/mpfit). The calculation routine considers the result as correct if the difference ε_{FIT} between the sum of the squares of the input size distribution and its deconvolution is less than 10^{-10} after 100 iterations. To limit error due to an over- or underestimation of the total number of particle N_{EG}, not constrained in this routine, the calculation was repeated several times, on normalized size distributions, by modifying the initial parameters until the calculated size distribution is within the limits of the counting uncertainties of the experimental size distributions. Examples of deconvolutions are shown in **Figure ~~S4~~S5**.

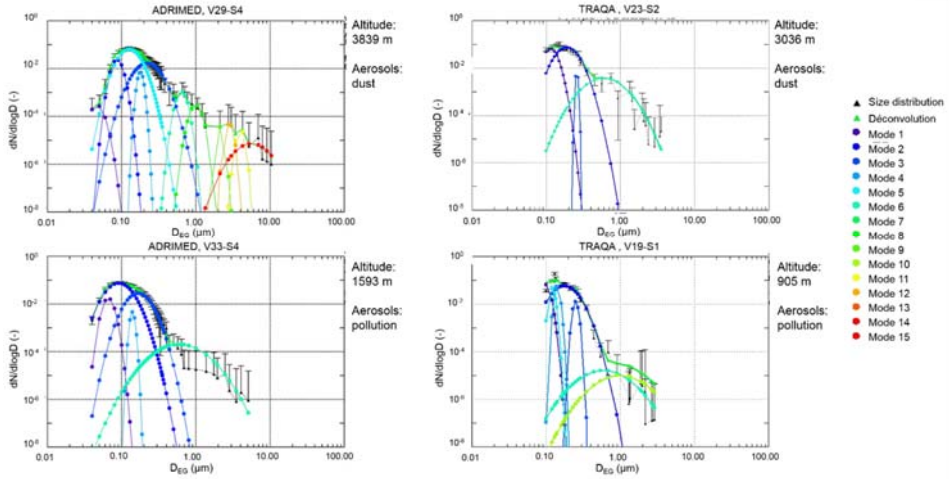

Figure ~~S4~~S5. Examples of reconstructed normalized number size distributions and their decomposition in log-normal modes for case studies of desert dust (upper panels) and pollution aerosols (lower panels) during ADRIMED and TRAQA. The deconvolution was performed with the IDL MPFIT routine for up to 15 different log-normal distribution modes. The uncertainties correspond to the Poisson statistical error.

Mis en forme : Police :Non Italique

Up to 11 modes were needed to fit the size distributions, of which up to 6 modes for D_{EG} < 1 µm. These do not necessarily have a physical meaning but are regarded as a way of reproducing the volume distribution at the highest possible size resolution.

S.3. Assessment of the complex refractive index

The complex refractive index necessary to estimate D_{EG}, and therefore correct the measured size distributions according to the optical equivalent diameter D_{EO}, are based on published values in the literature, some of them especially for our region of study (Ackermann, 1998; Petzold et al., 2009; Ryder et al., 2013; Di Biagio et al., 2015; Denjean et al., 2016; Sicard et al., 2016). The different values are presented in **Table S2**.

Aerosol	Campaign	Wavelength (nm)	Refractive index	References
Pollution (fine mode)	TRAQA, SAFMED	632.8	(1.50 – 1.72) – *i* 0.01	*Di Biagio et al., 2015*
Pollution (soot)	---	355	1.75 – *i* 4.64 10^{-1}	*Ackermann, 1998*
		532	1.75 – *i* 4.46 10^{-1}	
		1064	1.76 – *i* 1.43 10^{-1}	
Marine	---	355	1.51 – *i* 3.22 10^{-8}	*Ackermann, 1998*
		532	1.50 – *i* 1.12 10^{-8}	
		1064	1.47 – *i* 1.92 10^{-4}	
Desert dust	---	355	1.53 – *i* 1.66 10^{-2}	*Ackermann, 1998*
		532	1.53 – *i* 6.33 10^{-3}	
		1064	1.53 – *i* 4.30 10^{-3}	
	ADRIMED	530	(1.51 – 1.57) – *i* (1.0 – 4.6) 10^{-3}	*Denjean et al., 2016*
	SAMUM	450	(1.55 – 1.57) – *i* (3.1 – 5.2) 10^{-3}	*Petzold et al., 2009*
		550	(1.55 – 1.56) – *i* (1.6 – 4.2) 10^{-3}	
		700	(1.55 – 1.56) – *i* (0.3 – 2.5) 10^{-3}	
	FENNEC	550	1.53 – *i* (1.0 – 3.0) 10^{-3}	*Ryder et al., 2013*
Mixed aerosols	AERONET	440	(1.42 – 1.48) – *i* (2.8 – 4.7) 10^{-3}	*Sicard et al., 2016*

Table S2. Compilation of published values of refractive index and their wavelengths, for different aerosol type with some of them especially for our region of study (Mediterranean Sea).

Mis en forme : Police :Non Italique

In the absence of complementary information on the variability of the chemical composition with size, the refractive index was considered as independent on particle size. The refractive index for mixed aerosols (AE_{scatt} between 0.5 and 1.0) was calculated as volume-weighted averages of pollution aerosols and desert dust as

$$m = \sum_i f_i \times m_i \quad \textbf{(S4)}$$

where f_i et m_i are the volume fractions and the complex refractive index of two types of aerosols i, respectively. We assumed arbitrarily that f_i = 0.8 for desert dust and f_i = 0.2 for pollution aerosols for $AE_{scatt} \leq 0.75$, and f_i = 0.2 for desert dust and f_i = 0.8 for pollution aerosols for AE_{scat} >0.75. The extrapolation to our working wavelengths (450, 532, 550, 700 and 865 nm) was done by assuming the spectral dependences obtained by Ackermann (1998) between 355 and 532 nm and between 532 and and 1064 nm. The spectral dependence was applied to the refractive index for desert dust and mixed aerosols obtained by Di Biagio et al. (2016) and Denjean et al. (2016) for case studies during TRAQA and ADRIMED.

S.4. Comparison between in situ measurements and calculations of the extinction and scattering coefficient

The validation of the number size distributions reconstructed from airborne measurements, henceforth their ability in yielding the column-integrated but size-segregated extinction, was assessed by calculating, on 30-second averages, the extinction coefficient σ_{ext} at 532 nm and the scattering coefficient σ_{scatt} at 450, 550 and 700 nm, and by comparing them to σ_{ext} measured by the CAPS-PMex (only operated during ADRIMED) and to σ_{scatt} measured by the nephelometer, respectively. The comparisons were evaluated by examining the correlation coefficient R, the root-mean square error (RMS) and the bias (B) of their linear regression. The complex refractive index at each wavelength was varied until the best agreement between calculated and measured σ_{scatt} and σ_{ext} was achieved within the estimated error bars. The retrieved refractive index matching measurements and calculations are summarized in **Table S3.**

Mis en forme : Police :Italique
Mis en forme : Police :Italique
Mis en forme : Police :Italique
Mis en forme : Police :Italique
Mis en forme : Police :Italique
Mis en forme : Police :Italique

Aerosol type	Complex refractive index *m* ~~at various wavelengths~~								
	450 nm	**532 nm**	**550 nm**	**632.5 nm**	**655 nm**	**670 nm**	**700 nm**	**865 nm**	**1054 nm**
Clear layer / maritime	(1.40-1.50) -i(0 - 0.002)								
Desert dust	(1.50-1.57) – i(0.004-0.007)	(1.50-1.57) -i(0.002-0.004)						(1.50-1.57) – i(0.0020.003)	(1.50-1.57) – i(0.001-0.003)
Pollution	(1.41-1.77) – i(0.002-0.022)	(1.41-1.77) – i(0.002-0.018)	(1.41-1.77) – i(0.002-0.017)	(1.41-1.77) – i(0.002-0.015)	(1.41-1.77) -- i(0.002-0.014)	(1.41-1.77) – i(0.002-0.014)	(1.41-1.77) – i(0.002-0.013)	(1.42-1.78) – i(0.001-0.010)	(1.42-1.79) – i(0.001-0.008)
Mixed aerosol (AE ≤0.75)	(1.48-1.61) – i(0.004-0.010)	(1.48-1.61) – i(0.002-0.007)	(1.48-1.61) – i(0.002 - 0.007)	(1.48-1.61) – i(0.002-0.006)	(1.48-1.61) – i(0.002-0.006)	(1.48-1.61) – i(0.002-0.006)	(1.48-1.61) – i(0.002-0.005)	(1.48-1.61) – i(0.002-0.005)	(1.48-1.61) – i(0.002-0.004)
Mixed aerosol (*AE* >0.75)	(1.43-1.73) – i(0.002-0.019)	(1.43-1.73) – i(0.002-0.015)	(1.43-1.73) – i(0.002-0.014)	(1.43-1.73) – i(0.002-0.013)	(1.43-1.73) – i(0.002-0.012)	(1.43-1.73) – i(0.002-0.012)	(1.43-1.73) – i(0.002-0.011)	(1.43-1.73) – i(0.001-0.009)	(1.43-1.74) – i(0.001-0.007)

Table S3. Best-guess of the spectral refractive index obtained for the corrections of the optical particle counter, and comparison of measurements and calculations for clear layer/maritime aerosol, desert dust, pollution and mixed aerosol. The values extrapolated to 670 and 870 nm (working wavelengths of POLDER-3) are also shown.

Tableau mis en forme

Tableau mis en forme

The results of the comparison at 550 (σ_{scatt}) and 532 nm (σ_{ext}) are illustrated in **Figure ~~S5~~S6**. The uncertainties associated with the evaluation of the size distribution, the measured scattering and extinction, and finally the aerosol optical depth retrieved are estimated as the quadratic sum of the instrumental uncertainties as well as with the variability due to the reduction of the native time-resolution to a common time step of 30 seconds, a standard deviation generically indicated here as Δ_{30sec}. The instrumental uncertainties for the nephelometer and the CAPS-PMex are evaluated as ±10% for submicron aerosols (Anderson et al., 1996), and ±3.2% (Massoli et al., 2010), respectively. The error on the number of particles n_i (i = generic bin) follows the Poisson's law as $\Delta_{Poisson} = \sqrt{n_i}$. The comparison between measured and calculated σ_{scatt} at 450 and 700 nm are not shown as they are analogous to those at 550 nm.

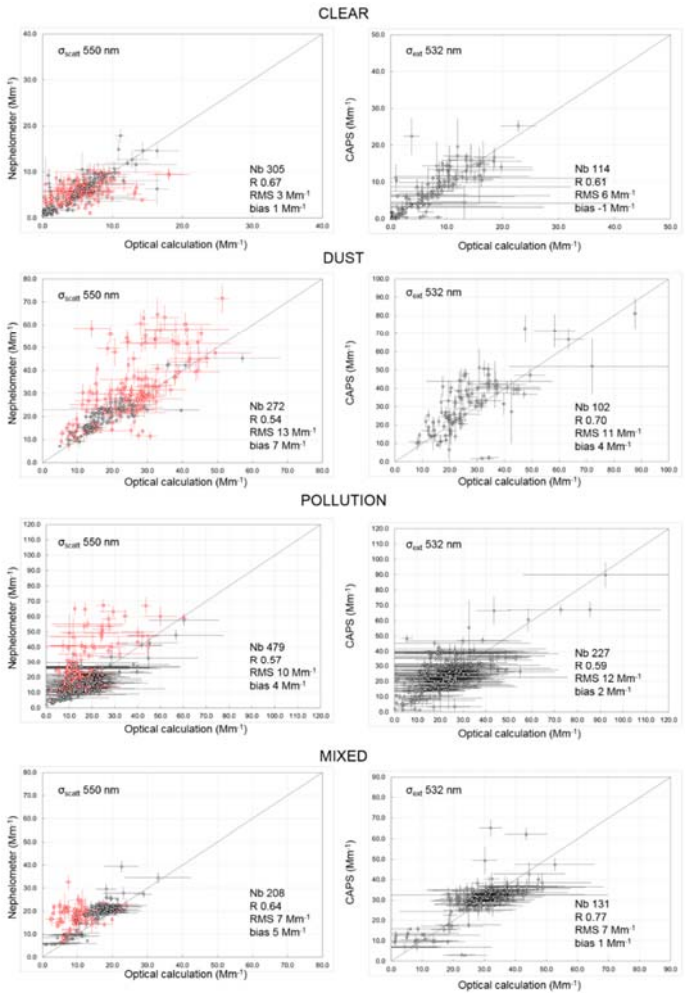

Figure ~~S5~~S6. Comparison of optical calculation and measurements of σ_{scatt} at 550 nm and σ_{ext} at 532 nm for all aerosol layers of all vertical profiles during TRAQA (red) and ADRIMED (black) campaigns. The comparison for σ_{ext} is shown only for ADRIMED since there were no CAPS-PMex measurements during TRAQA. See the text for error bars calculation.

The comparison is satisfactory for all aerosol types, and in particular concerning σ_{ext}. The systematic underestimation of the larger values of σ_{scatt} during TRAQA is due to the faulty operation of the Grimm OPC above 350 m from sea level. These data points were removed from the dataset for POLDER-3 AOD and AOD_C evaluation while kept for the evaluation of

196 AOD_F which is not affected by errors in sizing the largest particles. The uncertainties for the
197 optical computation of σ_{scatt} are higher for pollution layers than for other types of aerosols. This
198 is due to the wide range of possible values of the refractive index.